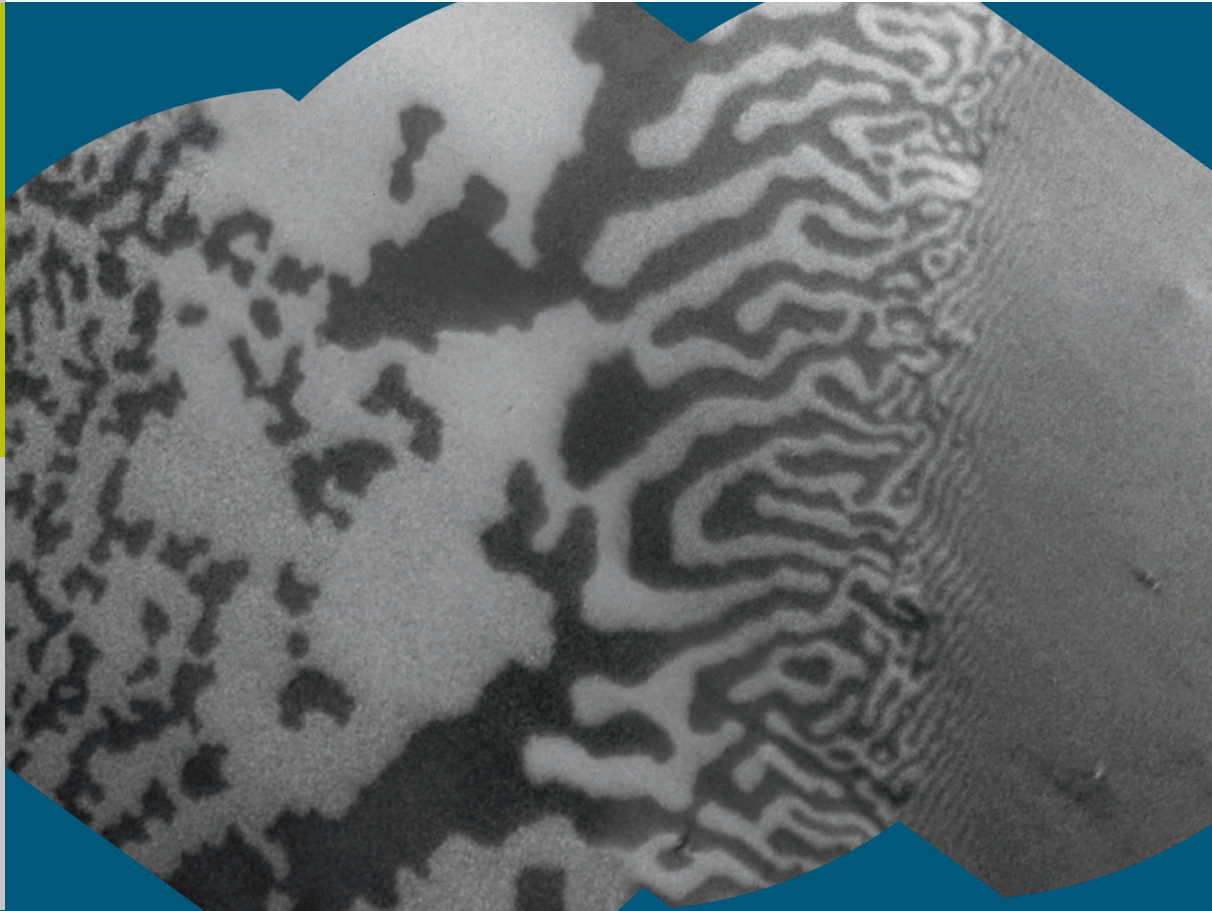


Spin-reorientation transition in epitaxial $\text{Ni}_x\text{Pd}_{1-x}$ films on Cu(001): a microscopic analysis

Daniel Marius Gottlob



Schlüsseltechnologien /
Key Technologies
Band/ Volume 104
ISBN 978-3-95806-049-4

Forschungszentrum Jülich GmbH
Peter Grünberg Institute (PGI)
Electronic Properties (PGI-6)

Spin-reorientation transition in epitaxial $\text{Ni}_x\text{Pd}_{1-x}$ films on Cu(001): a microscopic analysis

Daniel Marius Gottlob

Schriften des Forschungszentrums Jülich
Reihe Schlüsseltechnologien / Key Technologies

Band / Volume 104

ISSN 1866-1807

ISBN 978-3-95806-049-4

Bibliographic information published by the Deutsche Nationalbibliothek.
The Deutsche Nationalbibliothek lists this publication in the Deutsche
Nationalbibliografie; detailed bibliographic data are available in the
Internet at <http://dnb.d-nb.de>.

Publisher and Distributor:	Forschungszentrum Jülich GmbH Zentralbibliothek 52425 Jülich Tel: +49 2461 61-5368 Fax: +49 2461 61-6103 Email: zb-publikation@fz-juelich.de www.fz-juelich.de/zb
Cover Design:	Grafische Medien, Forschungszentrum Jülich GmbH
Printer:	Grafische Medien, Forschungszentrum Jülich GmbH
Copyright:	Forschungszentrum Jülich 2015

Schriften des Forschungszentrums Jülich
Reihe Schlüsseltechnologien / Key Technologies, Band / Volume 104

D 464 (Diss., Duisburg, Univ., 2014)

ISSN 1866-1807

ISBN 978-3-95806-049-4

The complete volume is freely available on the Internet on the Jülicher Open Access Server (JuSER)
at www.fz-juelich.de/zb/openaccess.

Neither this book nor any part of it may be reproduced or transmitted in any form or by any
means, electronic or mechanical, including photocopying, microfilming, and recording, or by any
information storage and retrieval system, without permission in writing from the publisher.

Erklärung

Hiermit erkläre ich, dass ich die vorliegende Arbeit selbstständig und ohne fremde Hilfe verfasst habe. Ferner habe ich außer den angegebenen Quellen keine anderen Quellen und Hilfsmittel benutzt. Die dem Sinn oder Wortlaut nach entnommenen Textpassagen oder Abbildungen habe ich in jedem Einzelfall kenntlich gemacht. Dieser Dissertation geht weder ein erfolgloser Promotionsversuch voraus, noch wurde sie in einem weiteren Promotionsverfahren eingereicht. Abgesehen von den angegebenen Publikationen sind die Ergebnisse dieser Dissertation unveröffentlicht. Diese Dissertation, die den Doktorgrad "Dr. rer. nat." anstrebt, wurde von Prof. Dr. C. M. Schneider betreut.

Berlin, den 13.10.2014

Daniel Gottlob

Zusammenfassung

Diese Arbeit befasst sich mit dem Spin-Reorientierungsübergang (SRT) in Ni/Cu(001) und NiPd/Cu(001) Schichtsystemen und der Verknüpfung von Domänenformation und magnetischer Anisotropie. Die intrinsischen Eigenschaften der magnetischen Anisotropie in dünnen Filmen im nativen Zustand, charakterisiert durch die Ausbildung verschiedenartiger Domänen, sind von großer Wichtigkeit für die Spintronik.

Um einem Modellverhalten nahezukommen wurden epitaktische Dünnschichtsysteme hergestellt. Dazu wurden Cu(001) Einkristalle mit hoher Oberflächenqualität präpariert und Ni beziehungsweise NiPd Filme in-situ durch Molekularstrahlepitaxie aufgewachsen. Domänenstrukturen wurden an demagnetisierten Proben mit Hilfe vom Röntgen-Zirkulardichroismus an einem synchrotronbasierten, energiegefilterten und aberrationskorrigierten Photoemissions-Elektronenmikroskop untersucht. Die Synchrotronstrahlung wurde als vielseitiges Analysewerkzeug zur elementselektiven Messung mit hoher Intensität genutzt, das die Bestimmung der Magnetisierungsrichtung durch die Dipolauswahlregeln ermöglicht.

Eine keilförmige Filmgeometrie gestattet eine räumliche Änderung der effektiven Anisotropie, was zu einzigartigen kontinuierlichen Messungen beginnend im Bereich der senkrechten magnetischen Anisotropie (PMA) bis zum SRT (0-100 ML) geführt hat. Es wurde eine neue Domänenformation mit rechtwinklig zueinander angeordneten Domänenwänden entlang der $\langle 110 \rangle$ -Achsen in der Nähe des SRT gefunden, die wir der Zunahme planarer Anisotropieeffekte zuschreiben. Dies befindet sich in guter Übereinstimmung mit theoretischen Modellen und Simulationen. Die Domänenformation während des Spinreorientierungsüberganges ist zum ersten mal beobachtet worden und konnte als sog. canted-state (verkippter Zustand) identifiziert werden. Es wurden NiPd Filme aufgewachsen um die Stärke der Gitterverzerrung, hauptverantwortlicher Parameter der PMA und SRTs, zu variieren. Die charakteristischen Domänen sind bis Pd-Konzentrationen von 12% beobachtet worden.

Das Verhalten von NiPd Filmen im Mischungsverhältnis kompressiver Verzerrung wurde untersucht, und bestätigte die theoretischen Überlegungen, dass keine PMA oder SRTs im Dickenbereich von 0-60 ML auftreten. Durch den Versatz von Ni- und Pd-Keilen war es möglich, den mischungsabhängigen SRT zu beobachten. Während der verschobene Parameterbereich zu stark veränderten Domänenformationen führt, konnten wie zuvor magnetische Anisotropieeffekte in der Ebene und ein canted-state identifiziert werden. Im Zusammenhang mit den untersuchten Domänenformationen schliesst die Arbeit mit einer Diskussion des T_c -Abfalls im SRT. Obwohl in vorigen Studien häufig berichtet, konnten wir keine Hinweise auf dessen Existenz in den beobachteten SRTs finden.

Abstract

This thesis deals with the spin-reorientation transition (SRT) usually observed at moderate thicknesses of 35-70 ML in Ni and NiPd thin films on Cu(001) and the connection between domain formation and anisotropy. The intrinsic properties of the magnetic anisotropy in thin films and native states, characterized by their domain formations, are of high interest in the framework of spintronics.

Thin film epitaxial systems are used to approach a model system behavior, therefore Cu(001) single crystals are prepared in a high surface quality and epitaxial Ni and NiPd films were grown in-situ by molecular beam epitaxy.

The domain formations are studied on demagnetized films by utilizing the x-ray magnetic circular dichroism on a synchrotron based, energy filtered, and aberration corrected x-ray photoemission electron microscope. Synchrotron light is used as a multi-purpose tool with element selectivity and high flux, enabling one to determine the magnetization direction by dipole selection rule geometries.

A lateral change of the effective anisotropy was achieved by employing a wedged film geometry, resulting in unique continuous measurements on the perpendicular magnetic anisotropy (PMA) area including the SRT area (0-100 ML) in Ni/Cu(001). A new domain formation of rectangularly ordered domains with domain walls aligning along the $\langle 110 \rangle$ -axes was found in the vicinity of the SRT and is attributed to the increasing influence of planar anisotropies, found to be in a very good agreement with theoretical models and simulations. The domain formation throughout the SRT is observed for the first time and identified as a canted state transition. Ni-like NiPd films were grown in order to vary the film-strain, the major driving parameter for the PMA and SRTs, yielding domain formations of similar characteristics up to Pd-concentrations of 12%.

The behavior of NiPd films exhibiting compressive strain was investigated, verifying theoretical predictions that no SRT or PMA can be found throughout the whole thickness range of 0-60 ML. Offsetting the elemental wedges made it possible to observe a composition-driven SRT. While the varied parameter range results in a strongly varied domain formation, in-plane anisotropy influence and a canted state could be found again. In the framework of the observed domain formations in the microscopic setup, a discussion of the T_c drop at the SRT concludes this thesis. While being frequently reported, we could not find any hints for its existence in various examined SRTs.

Contents

1	Introduction	1
2	Fundamental aspects	7
2.1	Magnetism	7
2.1.1	Stoner Model	7
2.1.2	Magnetism in transition metal alloys	10
2.1.3	Magnetic Anisotropy	12
2.1.4	Spin reorientation in uniaxial anisotropy model	16
2.2	Anisotropy and spin-reorientation transition in Ni/Cu(001)	18
2.3	Magnetic domains & domain walls	19
2.4	Photoemission process & XMCD	23
2.5	Electron inelastic mean free path	26
3	Experimental methods & setup	29
3.1	Preparation	30
3.1.1	Molecular beam epitaxy	30
3.1.2	AUGER electron spectroscopy (AES)	33
3.1.3	Low energy electron diffraction (LEED)	35
3.1.4	Medium energy electron diffraction (MEED)	36
3.2	Photoemission & low energy electron microscopy	37
3.2.1	Optics for immersion lens microscopy	38
3.2.2	Imaging modes	42
3.2.3	Generation of polarized x-rays	46
3.2.4	FE-LEEM-P90 at UE56/1-SGM	49
3.2.5	Determination of image rotations.	53
4	Sample preparation & characterization	55
4.1	Cu(001) substrate preparation	55
4.2	Ni/Cu(001) thin films	57

Contents

4.3	$\text{Ni}_x\text{Pd}_{1-x}/\text{Cu}(001)$ thin films	58
4.3.1	Preparation and characterization	58
4.3.2	Effects on lattice strain	59
5	Magnetic properties of $\text{Ni}/\text{Cu}(001)$ and $\text{Ni}_x\text{Pd}_{1-x}/\text{Cu}(001)$	63
5.1	$\text{Ni}/\text{Cu}(001)$ and Ni-like $\text{Ni}_x\text{Pd}_{1-x}/\text{Cu}(001)$	64
5.1.1	$\text{Ni}/\text{Cu}(001)$	64
5.1.2	Ni-like $\text{Ni}_x\text{Pd}_{1-x}$ films on $\text{Cu}(001)$	78
5.1.3	Summary Ni and Ni-like $\text{Ni}_x\text{Pd}_{1-x}$ films on $\text{Cu}(001)$	83
5.2	$\text{Ni}_x\text{Pd}_{1-x}/\text{Cu}(001)$ in higher Pd concentration	85
5.2.1	Thickness wedged $\text{Ni}_x\text{Pd}_{1-x}$	85
5.2.2	Composition wedged $\text{Ni}_x\text{Pd}_{1-x}$	87
5.2.3	Summary $\text{Ni}_x\text{Pd}_{1-x}$ films with higher Pd concentration	97
5.3	Domain patterns close to vanishing lattice mismatch	98
5.3.1	Continuous films in the vicinity of vanishing lattice mismatch . . .	99
5.4	T_c drop at the spin-reorientation transition	100
6	Summary and outlook	103
	Bibliography	107
	Acknowledgements	125
	Curriculum Vitae	129
	List of own Publications	131

1 Introduction

Present everyday life is dominated by electronic technology, miniaturized to a degree that was unimaginable some decades ago. The age of information technology, starting with the success of the personal computer and the availability of the internet twenty years ago, brought us to a lifestyle with every possible information at our fingertips. As the most notable representative, the 'smartphone' is more of a pocketable computer with a processing power comparable to a supercomputer of the early 90s [1, 2] than a machine solely enhancing telephone experience. Intriguingly, the most important scientific advances promoting this development can be found in the field of magnetism, eventually leading to the technological and scientific field of spintronics [3]. The combination of electrical charge and the quantum mechanical property of spin, mediating magnetism, led to the dramatic progress in the field of information technology.

Magnetism, as a fascinating property of naturally occurring materials, has been subject to scientific engagement since its first notation about 2000 years ago [4]. Scientific links, e.g. between the magnetic and electronic properties could be made already in 1856 by the observation of magnetoresistance (the resistivity of a ferromagnet on behalf of its magnetization direction) by THOMSON [5]. The MAXWELL equations, deduced in the late 19th century, offer a physical basis to evaluate magnetic phenomena in the framework of classical electrodynamics [6]. A theoretical connection between magnetism and its interaction with (magnetic) solids, electrical fields, and mechanical forces was made, but this description was not able to explain the microscopic mechanisms. The theoretical solution emerged from the extensive work on quantum mechanics in the early 20th century introducing the electronic spin [7]. The origin of magnetism is hence understood as a collective phenomenon, a many-body interaction of electrons with a half-integer spin. Magnetic interactions connected to the spin-property of electrons are identified as spin-orbit coupling and exchange interaction, not only determining macroscopic behavior, but also giving rise to a variety of magnetic effects. The magnetic moment of a macroscopic specimen organizes by a competition of these two mechanisms. This conclusion led to a phenomenological prediction of ferromagnetism on the basis of the spin-split band structure at the FERMI-edge by the STONER-criterion [8]. Only

1 Introduction

three elements from the main group of the periodic table of elements fulfill this criterion at room temperature, Iron (Fe), Cobalt (Co), and Nickel (Ni), making these materials crucial components in magnetic research.

From this point, discoveries on magnetic effects could be made or understood, starting with the anisotropic magnetoresistance (AMR) [9], an effect originating from spin-orbit scattering of a spin-polarized current depending on the magnetization \mathbf{M} of a specimen with respect to the current direction \mathbf{j} ($\mathbf{M} \parallel \mathbf{j}$ results in lower, $\mathbf{M} \perp \mathbf{j}$ in higher resistivity). However, the effect results in a resistivity change of only a few percent. Fueled by the improvements in vacuum technology, taking pressures to a level of 10^{-10} mbar, preparation by molecular beam epitaxy allowed one to produce pure metallic films on the atomic level. The interlayer exchange coupling (ILC) might be the first outstanding discovery based on these advances [10]: Two ferromagnetic (FM) layers of nm thickness, separated by a metallic, but nonferromagnetic (NFM) interlayer, establish a coupling mechanism via spin-polarized quantum-well states in the interlayer. Strikingly, both a parallel and antiparallel coupling can be found by tuning the interlayer thickness. This property can be used to pin the magnetization of a ferromagnetic layer at a defined state, a design used in the subsequent discovery of the GMR effect. Discovered by the two groups of FERT [11] and GRÜNBURG [12] separately at the end of the 80s, they were awarded the NOBEL price in 2007 because of the extensive influence of GMR on the research field of magnetism. In the sample geometry of FM/NFM/FM thin film layers, the resistivity was measured with parallel and antiparallel magnetization alignment. In the parallel case, a current passing through the stack finds a low resistivity, while an antiparallel magnetization increases the resistivity by a significant amount. Resistivity changes of up to 60% at room temperature enabled many new applications, most prominently read/write head geometries for a new generation of hard disk drives (HDDs). Physically, the effect is governed by spin-dependent scattering of electrons caused by exchange interaction. Additionally, the discovery of GMR can be named as the starting point of spintronics as a separate field of research, also with great impact on the technological advance.

Beginning in the 1950s, digital data storage on magnetic tapes introduced magnetism into what is now known as information technology. Tapes were replaced in favor of hard disk drives (HDDs), which are comprised of spinning disks coated with a magnetic material. The data is written in form of small magnetic domains by a write/read head hovering above the disks. While the first HDD by IBM featured a capacity of 3.5 megabytes in a form factor of approximately two cubic meters with covers attached, commercial HDDs of around 2010 can hold 4 terabytes in a 3.5" housing [13]. The

downscaling of magnetic domains into the sub 100 nm regime is driven by the success of spintronics: Incorporating thin-film layer structures exploiting the GMR effect can be named as one of the milestones in HDD developments. State-of-the-art technology in magnetic data storage features tunnel-magnetoresistance [14] as detection mechanism in the read-heads, while grained films as storage media are already scratching at the density limit given by superparamagnetism [15], an effect when the magnetic energy stored in grained media is comparable to the energy fluctuations induced by room temperature, leading to spontaneous reorientation of the magnetization. Current perpendicular to plane GMR [16] and heat/microwave-assisted magnetic recording (HAMR, MAMR [17]) are trying to resolve the problem by creating more sensitive read heads or shifting the superparamagnetic limit by making harder magnetic materials writable. However, also completely different spintronic approaches, magnetic random access memory (MRAM) [18] and magnetic domain wall racetrack memory [19], may pave ways to faster and smaller mass data storage, while the spin-valve transistor [20] and magnetic logic-elements [21] find spintronic solutions for data processing.

As evident from the development in technological and scientific advances, the properties of magnetism in thin films are of utmost importance. The downscaling of technological components is an ongoing process which creates more efficient devices at lower energy consumption, as can be seen from the initial example of the 'smartphone', also featuring small magnetic sensors. In order to put the effects arising in the reduced dimensions to optimum use instead of struggling to overcome them, the energetically favorable organization of magnetic films needs to be investigated in studies on systems free from external influences and remanences. Magnetic anisotropy, the energetic preference of the magnetic moment to align along preferred direction, is strongly influenced by the thin and ultrathin epitaxial film geometry via contributions arising from thin film surfaces and tension [22]. While the magnetization is typically found to be aligned within the plane of the film due to a reduction of the magnetic stray field energy, ultrathin epitaxial films (e.g. Co/Au(111) [23], Fe/Cu(001) [24]) are found to exhibit a magnetization perpendicular to the film plane, referred to as perpendicular magnetic anisotropy (PMA). By controlling the parameters influencing the anisotropy of a thin film, i.e. thickness, temperature, and film stress, the favored magnetization direction can be tuned. In a critical parameter range, a reorientation of the preferred magnetic axis can be found, known as spin reorientation transition (SRT) [25]. At this point the PMA, often driven by the surface anisotropy, decreases in relative influence leaving the magnetostatic anisotropy as the dominating contribution, pulling the magnetization in-plane - at least in a very simple picture. In more complicated cases, the energy balance, leading to a magnetic

1 Introduction

state, has to take into account additional terms, such as stress-related magnetostriction. The transition itself underlies complicated mechanisms, which determine the nature of the magnetization rotation. Energy minimizations, which take higher order anisotropy terms into account, reveal the possibility of second-order transitions to proceed (i) by a continuous shift of the magnetization angle (canted state) or (ii) by shifting the weight between both conforming states of in-plane and out-of-plane magnetization (coexistence state). First-order transitions have a long history in theory, while experiments almost exclusively find second order transitions [26]. In addition, the thin film systems can be treated in the anisotropy-flow model [27], allowing one to address the evolution of the anisotropy constants in thin film geometry [28] and also under applied field [29,30]. A special case was found in Ni/Cu(001) [31], which exhibits a thickness-driven inverse spin reorientation (iSRT) at about 7 monolayers (ML) [32] - a magnetization preference switching from in-plane to perpendicular with increasing thickness. The resulting PMA is upheld for a fairly large thickness regime, resulting in an SRT at moderate thickness of 35-60 ML [31,32]. Uniaxial anisotropy models explain this surprising behavior by additional anisotropy contributions arising from film strain and its reduction with thickness increase.

However, the investigation of the microscopic states in the PMA phase and the spin-reorientation of thin films is an underrepresented aspect in research. Magnetic simulations of magnetic systems with varying anisotropy show the existence of different magnetic phases, that cannot be addressed in experiments employing applied fields [33]. The study presented in this thesis hence focuses on the microscopic formation of domains in the demagnetized state, using Ni/Cu(001) as a model system for the thickness driven SRT, and NiPd/Cu(001) alloys to investigate a composition driven SRT in comparison, aiming for a deeper insight to the undisturbed system.

The microscopic imaging of magnetic contrast is a big challenge, since the means of imaging need to interact with the magnetic structure of the specimen. First experiments used BITTER pattern technique [34], imaging magnetic domains by bringing ferromagnetic particles in contact with the sample. Since the contrast is created as a reaction to the stray field of the magnetization, only perpendicularly magnetized samples are susceptible to this technique, and the exhibited stray field strength plays a crucial role to the technique's quality. While the technique's resolution is limited by the particle's size (down to 10 nm) and resolution of the optical microscope (limited by the wavelength of the illuminating light source), technical circumstances as the fluidic application and optical data acquisition with a microscope make this technique unsuitable for magnetic thin film samples.

Experiments based on the magneto optic KERR-effect [35,36], the rotation of the polarization plane of photons, are limited by the wavelength of the light (usually > 150 nm). Also, the typical execution of the experiment in ambient pressure makes its application for in-situ grown magnetic films an ambiguous choice.

In scanning electron microscopy with polarization analysis (SEMPA) a polarization analyzer, such as the spin low energy electron diffraction (SPLEED) detector, is used to map the magnetization of the first few atomic layers in a scanning approach. The resolution of this technique (about 20 nm) is only limited by the spot size of the electron beam. However, the relatively low efficiency of the polarization analyzer leads to minimum scanning times of about 10 s, preventing a useful live view utilization.

Electron optical magnetic imaging with a photoemission electron microscope (PEEM), offering full field observation, a non-destructive means for measuring epitaxial films without sample thickness restriction, is best suited for experiments on the NiPd/Cu(001). The availability of synchrotron light as a light source of high flux and brilliance combined with element-selectivity makes x-ray PEEM (XPEEM) the method of choice for this study. Magnetic information has been shown to be accessible in spectroscopic experiments by exploitation of x-ray magnetic circular dichroism (XMCD) [37] and x-ray magnetic linear dichroism (XMLD) [38], yielding magnetic signals with respect to the spin orientation. The technique has been employed as a means to create magnetic contrast in PEEM [39] yielding first scientific results in the beginning of the 90s [40–43]. All experiments on magnetic contrast shown in this study have been carried out at the aberration corrected, energy filtered PEEM/LEEM located at the Forschungszentrum Jülich soft x-ray beamline UE56/1-SGM at the synchrotron facility BESSY II, Germany, Berlin. The instrument is the first commercially available aberration corrected PEEM/LEEM. Together with the SMART microscope, the pioneering project in aberration corrected PEEM/LEEM [44], it is the only aberration corrected PEEM with permanent synchrotron access to date.

This thesis is organized as follows:

- Chapter 2 provides an introduction to the fundamentals of magnetism in 3d transition metals. The magnetic anisotropy of Ni/Cu(001) and its contributions arising from the thin film geometry will be discussed in particular, setting up a framework for the evaluation of experimental data. The chapter finishes with an introduction to the photoemission process.
- In chapter 3, the experimental setup and methods are presented. The description ranges from the mechanisms operating during thin film growth and the connected

1 Introduction

analyzation tools to the layout of the photoemission electron microscope.

- A characterization of the in-situ grown samples and substrate preparation procedure is presented in chapter 4. The substrate and grown thin films are analyzed with respect to their purity and surface quality.
- Chapter 5 is concerned with the results obtained from Ni/Cu(001) and $\text{Ni}_x\text{Pd}_{1-x}/\text{Cu}(001)$ films. Pure Ni wedges are subject to evaluation first, creating a connection between domain observation and the anisotropy studies from literature. The nature of the SRT at moderate thicknesses, and, together with Ni-like NiPd/Cu films, the domain structure close to the SRT thickness is analyzed. The studies are expanded to NiPd films with higher Pd content, evaluating the findings on a composition driven SRT. The chapter concludes with a brief review of the observed SRTs concerning a T_c drop widely reported in literature.
- Chapter 6 summarizes the results found in the previous chapters and concludes the thesis with an outlook on further experiments and challenges.

In this structure, the thesis at hand tries to provide insight into the formation of the SRT in a microscopic study. Demagnetized Ni/Cu(001) and NiPd/Cu(001) were chosen to serve as epitaxial model systems to observe domain formation in the yet microscopically unexamined vicinity of the SRT. While previous studies focused on averaging methods under applied field, this thesis tries to capture the unique properties of the undisturbed domain state under the variation of the film strain via compositional changes.

2 Fundamental aspects

An overview on the physical fundamentals which are relevant for this thesis will be given in this chapter. Since the main focus is put to the anisotropic behavior of thin film samples, especially Ni/Cu(001) and the domain formation as the main part of the chapter, an understanding of ferromagnetism will be given first in Sect. 2.1.1. A short description of magnetism in alloys can be found in Section 2.1.2. The origin and phenomenology of magnetic anisotropy is described in Sect. 2.1.3, which is followed by an introduction to spin reorientation transitions (Sect. 2.1.4). More details are given on the anisotropy development in Ni/Cu(001) thin films in Sect. 2.2. The energy minimization principle of domains for demagnetized films will be shortly addressed in Sect. 2.3.

The fundamentals of photoexcitation will be explained in Sect. 2.4, since it forms the basis of the experimental method of XPEEM used for this thesis. This includes a description of the mechanism used to extract magnetic information, the XMCD effect. Eventually, an important property of electrons propagating through matter is described in the final Section 2.5, the electron inelastic mean free path.

2.1 Magnetism

2.1.1 Stoner Model

Ferromagnetic materials are characterized by a spontaneous long range order of magnetic moments without an applied external magnetic field, resulting in a remanent magnetization M . The occurrence of ferromagnetism is reasoned by the minimization of the free energy, which will be the topic of this section. Ferromagnets can be divided into two groups depending on the origin of collective ordering of magnetic spins: itinerant and localized ferromagnets. The latter are represented by rare earth elements, which are characterized by a magnetic moment tied to localized, i.e. deeply bound, f-electrons. These electrons are only weakly participating in chemical processes of the atoms, hence the localized ferromagnets are theoretically treated in a spin-lattice model [45], fixing the magnetic moments at lattice points. Contrary, an itinerant ferromagnet's magnetic moment arises from the valence band electrons, which are only weakly bound to the

2 Fundamental aspects

atom. These delocalized electrons are a feature of all transition metals, however, at room temperature only Ni, Co, and Fe exhibit ferromagnetism. In these materials, the whole electron system has to be taken into account, as the energy minimization is subject to different influences. (i) The quantum mechanical effect of exchange interaction originates from the symmetry of particle wave functions. In (anti-)ferromagnetic materials, the (anti-)parallel alignment of magnetic moments is energetically favorable due to the exchange interaction. (ii) Considering the PAULI exclusion principle, the parallel alignment of spins requires difference in one of the other quantum numbers n , l or m_l of the electrons, effectively increasing kinetic energy of the electron system while decreasing the COULOMB repulsion of the electrons.

The energy difference between an excited electron state in a parallel spin alignment and the antiparallel alignment in the otherwise same quantum-mechanical state is called exchange energy. If the energetic gain due to exchange interaction is larger than the expense of increased kinetic energy, the system is able to minimize its energy by aligning the spins, i.e. magnetic moments, parallel [46]. The electrons carrying the magnetic moment in itinerant ferromagnets are organized in the valence band, which is important when formulating the so called STONER criterion to predict ferromagnetism [8]. The STONER model is developed in the framework of density functional theory including spin polarization [47], for an extensive description see Ref. [48]. The following description is based on BLUNDELL [45]:

In a situation of potential ferromagnetism, a certain amount of electrons at the FERMI-level align their spin. Changing their spin from $+1/2$ in the balanced state to $-1/2$ for the ferromagnetic state is connected to an energy change of δE from $E_f - \delta E$ to $E_f + \delta E$ given by the free density of states $g(E)$ (see Fig. 2.1). The increase in kinetic energy E_{kin} is given by the amount of aligned electrons $(g(E_F)/2) \cdot \delta E$

$$\Delta E_{\text{kin}} = \frac{1}{2}g(E_F)(\delta E)^2 \quad (2.1)$$

The reduction of the COULOMB repulsion for electrons with the same spin serves as an energy reduction of potential energy E_{pot} in the ferromagnetic case on the other hand:

$$\Delta E_{\text{pot}} = -\frac{1}{2}I(g(E_F)\delta E)^2 \quad (2.2)$$

Here, the STONER parameter I is introduced as a measure of the difference in COULOMB energy. It can be expressed as the exchange integral, averaging over the COULOMB interactions in the many-particle system of valence electrons [49]. The energy balance,

as the sum of both contributions

$$\Delta E = \Delta E_{kin} + \Delta E_{pot} \quad (2.3)$$

$$= \frac{1}{2} g(E_F) (\delta E)^2 (1 - I \cdot g(E_F)) \quad (2.4)$$

shows occurrence of ferromagnetism if $\Delta E < 0$. Hence, the formal expression of the STONER criterion is given as:

$$I \cdot g(E_F) \geq 1 \quad (2.5)$$

Since the exchange interaction is similar for all 3d transition metals (resulting in $I \sim 1 \text{ eV}$) [49, 50], the density of states at the Fermi level is the most important parameter in the determination of the STONER criterion [51].

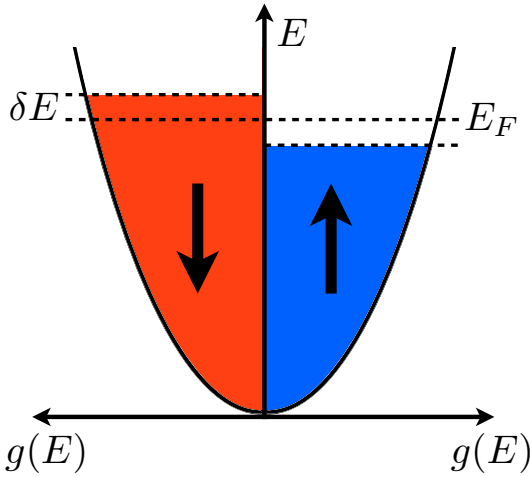


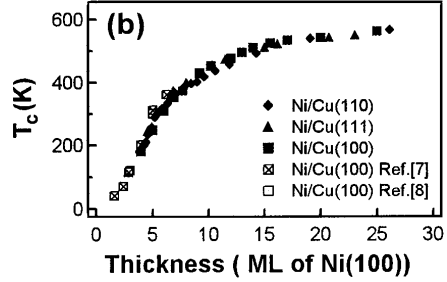
Figure 2.1 – Schematic description of the STONER-criterion and the related energies in the density of states $g(E)$.

and an applied magnetic field H :

$$\mathbf{M} = \chi_m \mathbf{H} \quad (2.6)$$

For every material satisfying the STONER criterion, there is a temperature T_c , the Curie temperature, at which the spontaneous order is lost and the ferromagnetism changes to paramagnetism in a second-order phase transition [52]. In paramagnetism, the magnetic moments of a material are in a disordered state, and can be temporarily ordered by applying a magnetic field [53, 54], effectively reinforcing it [55]. Paramagnetic materials (especially) are characterized by the magnetic susceptibility χ_m , a proportionality factor connecting the magnetization M

Figure 2.2 – Decrease of T_c with film thickness. References in image can be found here as [56, 57]. Thicknesses of the different Ni films and their respective symmetries resulting in differing lattice constants are given in monolayers (ML) of Ni(100). From [58]



Curie temperature in thin films Calculations in the HEISENBERG model¹, applying a random phase approximation [59], show a dependence of the CURIE temperature on the number of nearest neighbor atoms. Hence, T_c is expected to decrease if the thickness of a magnetic film is reduced [52]. As e.g. found in experiments on Ni/Cu(001) films [60], the CURIE temperature decrease can be described by a finite-size scaling relation

$$\frac{T_c(\infty) - T_c(h)}{T_c(h)} = \left(\frac{h}{h_0} \right)^{-1/\nu} \quad (2.7)$$

with deviations for ultrathin films described best by

$$\frac{T_c(\infty) - T_c(h)}{T_c(h)} = \left(\frac{h - h'}{h_0} \right)^{-1/\nu}. \quad (2.8)$$

$T_c(h') = 0$ denotes an offset parameter, h_0 a scaling factor characteristic for each system, and ν the bulk correlation length exponent. The T_c development for Ni films can be seen in Fig. 2.2, compiled and measured by ZHANG et al. [58]. The strongest effect of decreasing film thickness can be found for films below 15 ML ≈ 2 nm, HUANG et al. [61] found the CURIE temperature of bulk Ni to be valid for films of ≥ 35 Å thickness [62].

2.1.2 Magnetism in transition metal alloys

The magnetic properties of ferromagnetic materials can be widely varied by alloying. For binary alloys, the SLATER-PAULING curve represents the development of magnetic moment based on the electrons per atom (see Fig. 2.3). A maximum of $2.4 \mu_B$ occurs at the crossing point of two decreasing branches with Ni and Co alloys on the right

¹A model defined by the Hamiltonian $\mathcal{H} = 1/2 \sum_{i,j} J_{i,j} S_i \cdot S_j$; i and j referring to lattice sites, J is the coupling constant between the to spins S_i and S_j . In a first, mostly very reasonable approximation, the interaction is limited to spins on neighboring lattice sites)

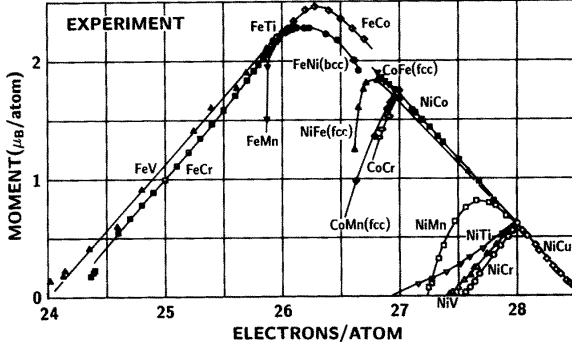


Figure 2.3 – SLATER-PAULING curve for 3d transition metal alloys, describing the magnetic moment per atom depending on the averaged number of electrons per atom. From [63]

and Fe alloys on the left branch. The different slopes of left and right branch are a result of different screening behavior given by minority and majority spin electrons, respectively [64].

Magnetism in NiPd alloys With respect to the study presented in this thesis, the magnetic behavior of binary 3d/4d transition metal alloys of Ni as one material is of interest. With the concentration x as the driving parameter, the behavior of magnetic moment ρ and CURIE-temperature T_c is linear for typical NiX alloys:

$$\rho(x) = \rho(0)(1 - \nu x) \quad (2.9)$$

$$T_c(x) = T_c(0)(1 - \nu x) \quad (2.10)$$

with ν denoting what could be called a magnetic valence ($\nu = 1, 2, 3, 4, 6$ for $X = \text{Cu, Zn, Al, Ti, Cr}$) [49]. This simple approach is driven by the idea that each Ni atom is replaced by a solvent atom (with respect to the concentration), linearly reducing the amount of Ni-driven magnetism. The magnetic valence ν is introduced due to the shared amount of valence atoms to take the intermixing of spin-up and -down into account. This approach has proven suitable for many Ni-rich alloys, as can exemplary be seen in the NiRu data in Fig. 2.4.

Alloys of Ni with materials featuring a high magnetic susceptibility however, find a deviation from this simple law. Pd, as the material of interest, is highly paramagnetic, characterized by a high susceptibility, and almost ferromagnetic by itself considering the STONER criterion [49, 65]. Pd atoms can easily be magnetized due to the exchange interaction with nearby ferromagnetic atoms in a crystallographic arrangement, hence

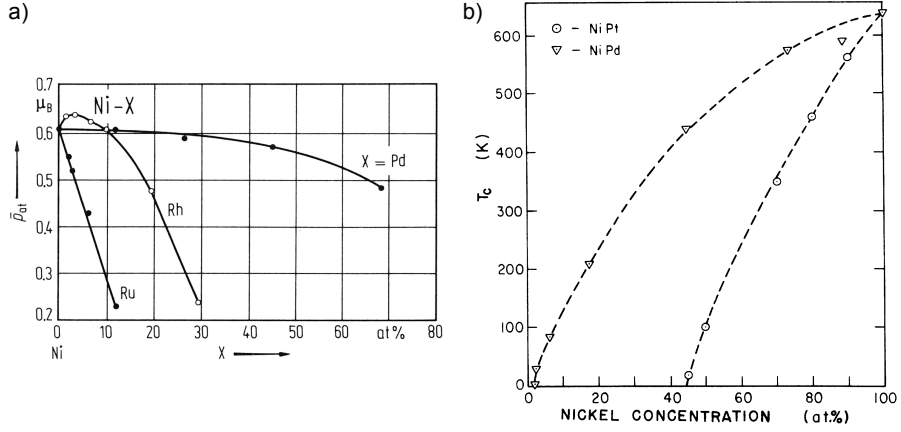


Figure 2.4 – Magnetic moment per atom in NiX alloys depending on concentration x of material X. NiPd shows a strong deviation from the linear behavior of Eqn. 2.9, due to its large susceptibility (a). From [67]. Development of T_c in NiPd alloys depending on Ni concentration (b). From [68].

exhibiting a ferromagnetic alignment of their own magnetic moments. Thus, the averaged magnetic moment per atom of NiPd alloys decreases much slower, as can be seen from experimental data displayed in Fig. 2.4 a). In the context of this study it is worth mentioning that bulk NiPd alloys exhibit ferromagnetic order for concentrations up to 93% Pd [66], room temperature ferromagnetism can be found up to $\sim 25\%$ Ni concentration [67, 68] (see Fig. 2.4 b))

2.1.3 Magnetic Anisotropy

Observation in experiments showed that the magnetic moments in a crystal behave anisotropically. Alignment along certain directions, so called easy axes, is preferred by the ferromagnetic crystal, whereas a magnetization along other (hard) axes is only possible by investing energy in form of an applied field (see Fig. 2.5). The HEISENBERG model, taking into account the exchange interaction, but not the magnetic anisotropy, cannot explain ferromagnetism in two-dimensional films above $T = 0\text{ K}$ [69]. Due to the short range of the exchange interaction, the magnetization is able to be rotated throughout the lengthscale of the so-called magnetic coherence length at a negligible energy expense [70], resulting in a paramagnetic state. The amount and strength of hard and easy axes is determined by a number of contributions, which will be described

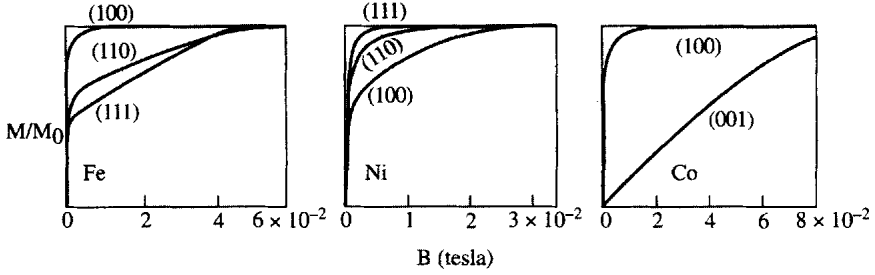


Figure 2.5 – Magnetization curves of Fe, Ni, and Co along different crystallographic axes. Easy and hard axes can easily be identified by the field strength needed to saturate the material. From [45]

in a phenomenological model in the following.

The magnetic anisotropy energy is defined by the energy that an external field has to provide to magnetize the material along a certain direction given by the angle γ . Following STÖHR & SIEGMANN [70], the energy density e_{ani} connected to uniaxial magnetic anisotropy has to be constant upon inversion along an easy axis, hence it can be expressed as an even function of γ . In a serial expansion

$$e_{\text{ani}} = K_2 \sin^2 \gamma + K_4 \sin^4 \gamma + K_6 \sin^6 \gamma + \dots, \quad (2.11)$$

with anisotropy constants K_i ($i = 2, 4, 6, \dots$) = $K_i(t, h)$ [energy/volume], where t denotes temperature and h film thickness. For the introduced geometry of the anisotropy, a positive contribution results in alignment along the axis (out-of-plane in the notation used in this thesis), a negative contribution results in a magnetization preference perpendicular to the axis (in-plane in the notation used in this thesis). The size of the anisotropy constants is typically described and determined in the frame of three microscopically different contributions - shape, magnetocrystalline, and magnetoelastic anisotropy, which will be discussed in the following.

- **Shape anisotropy:** The shape anisotropy arises from the demagnetizing field \mathbf{H}_d generated by the magnetization itself. On a microscopic level, the demagnetizing field is an effect of the dipolar coupling of atomic moments. While not being the only component arising from the dipolar coupling, it is the dominant term for thin films [70]. With a magnetic field \mathbf{H} generated by the gradient of the magnetization

2 Fundamental aspects

\mathbf{M} expressed as

$$\mu_0 \nabla \cdot \mathbf{H} = -\nabla \cdot \mathbf{M}, \quad (2.12)$$

the energy contained in the magnetic field created by a magnetic body is given as

$$e_d = \frac{\mu_0}{2} \iiint_{\text{all space}} \mathbf{H}_d^2 dV = -\frac{1}{2} \iiint_{\text{sample}} \mathbf{H}_d \mathbf{M} dV. \quad (2.13)$$

Hence, with a demagnetizing field $H_d = -M/(2\mu_0)$ given by the magnetization in a thin film, the energy/volume contained in the demagnetizing field with respect to the uniaxial anisotropy formalism can be written as

$$e_d = K_d = -\frac{1}{2\mu_0} M^2 \quad (2.14)$$

Considering the uniaxial nature of the anisotropy energy and a magnetic system that is indefinitely extended in two dimensions like a thin film, it becomes clear that the shape anisotropy is minimized if the magnetization lies in the plane of the film.

Energy contributions of the shape anisotropy for 3d transition metals are in the range of 10^{-4} eV/atom, as given by table 11.3 in [70].

- **Magnetocrystalline anisotropy:** The magnetocrystalline anisotropy arises from spin-orbit coupling in conjunction with the crystallographic structure. Dating back to its first proposition by VAN VLECK [71], the MCA can be qualitatively understood by a coupling of the isotropic spin moment to an anisotropic crystallographic lattice. The energetically favorable state of the system is gained by minimizing the overlap of the electronic wavefunctions. Hence, the orbitals are aligned with respect to their symmetry and the crystallographic lattice. The macroscopic magnetization is tied to this alignment by spin-orbit-coupling and the energy embedded can be expressed by the spin-orbit Hamiltonian

$$\mathcal{H} = \zeta(r) \mathbf{L} \cdot \mathbf{S}. \quad (2.15)$$

$\zeta(r)$ denotes the spin-orbit coupling constant. Mathematically, the magnetocrystalline anisotropy is defined as the difference between magnetic alignment along

hard and easy axis:

$$e_{\text{MC}} = K_{\text{MC}} = \sum_{\text{hard}} \zeta(r) \mathbf{L} \cdot \mathbf{S} - \sum_{\text{easy}} \zeta(r) \mathbf{L} \cdot \mathbf{S} \quad (2.16)$$

As can be seen from this discussion, no general statements can be made about the preferred direction of magnetization, as the crystallographic structure of the material and the connected easy axis' direction may vary with sample geometry. Ni, as the magnetic material of interest in this study, has its easy axis oriented along $\langle 111 \rangle$ direction. Calculations show that the small magnetic moment of 3d transition metals results in a comparably small contribution of magnetocrystalline anisotropy of about 10^{-5} eV/atom [72].

It is noteworthy, that symmetry breaks, e.g. at the surface, and forces acting on the crystallographic lattice structure create relevant energetic variations from the phenomenological description above, which are also of magnetocrystalline origin. However, they are typically described by additional anisotropy terms, which are covered in the following items.

- Magnetoelastic anisotropy: Strain applied to a ferromagnetic crystal introduces anisotropy via magnetostriction. The deformation of the unit cell changes the orbital overlap producing deviations from the relaxed system. Following CHAPPERT & BRUNO [73], the magnetoelastic anisotropy energy density can be expressed as

$$e_{\text{ME}} = K_{\text{ME}} = B\epsilon \quad (2.17)$$

where B is the material specific magneto-elastic coupling constant and ϵ denotes the strain within the film. Introduction of the strain tensor ϵ to the model was first proposed by NÉEL [74]. Typically, and certainly in the frame of this study, the strain is a result of lattice mismatch in an epitaxially grown film due to the adoption of the substrate's lattice constant. As will be discussed later (see Sect. 3.1.1), strain will be reduced in a thin film upon growth, hence the influence of the magnetoelastic anisotropy will decrease with film thickness. A description of the film strain resulting from epitaxial growth in a mismatched system, and its relaxation, can be found in Sect. 3.1.1.

- Surface anisotropy: In addition to the three contributions presented above, surface effects can be of important influence. Surface effects applying to the system studied in this thesis include a variation in strain due to surface relaxation, and the

2 Fundamental aspects

influence of a broken symmetry at the sample surface. Since the relative amount of surface decreases with film thickness h , surface anisotropy contributions are generally of the form

$$e_X^{\text{surf}} = K_X^{\text{surf}} = K_{X,0}^{\text{surf}}/h \quad (2.18)$$

The breaking of symmetry is modeled as a uniaxial contribution following

$$e_{\text{surf}} = K_{\text{surf}} = K_{\text{surf},0}/h. \quad (2.19)$$

The surface-dependent magnetoelastic contribution is expressed as

$$e_{\text{ME}}^{\text{S}} = K_{\text{ME}}^{\text{S}} = B_{\text{S},0}\epsilon/h. \quad (2.20)$$

The strain-dependent Néel pair-interaction model predicts opposing sign of these two contributions [75].

The anisotropy energy in a uniaxial system can be expressed as a sum of the introduced anisotropy contributions to the first anisotropy constant, henceforth denoted K_2^{eff} :

$$\begin{aligned} e_{\text{ani}} = K_2^{\text{eff}} &= K_{\text{d}} + K_{\text{MC}} + K_{\text{ME}} + K_{\text{surf}} + K_{\text{ME}}^{\text{S}} \\ &= -\frac{1}{2\mu_0}M^2 + K_{\text{MC}} + B\epsilon + K_{\text{surf},0}/h + B_{\text{S},0}\epsilon/h \end{aligned} \quad (2.21) \quad (2.22)$$

A graphical representation of this equation and its contributions can be seen in Fig. 2.7 for the relevant terms of the Ni/Cu(001) system as discussed.

2.1.4 Spin reorientation in uniaxial anisotropy model

From the description of the anisotropy contributions in the previous section it can already be seen that the anisotropy of a material is subject to variation upon material parameters as thickness h in films of reduced dimensions, film stress ϵ and temperature t in general. In the discussed uniaxial anisotropy geometry, it is possible that the variation of these parameters changes the sign of K_2^{eff} , resulting in a reorientation of the easy axis. This so called spin reorientation transition has been subject to research in the frame of epitaxial thin films since the pioneering work of GRADMANN [77, 78]. Theoretical predictions supporting these findings were given by GAY & RICHTER [79] and FREEMAN & WU [80]. With respect to the demagnetizing field of thin films as discussed in the previous section, the out-of-plane magnetized state connected to the perpendicular magnetic anisotropy

(PMA) is an unexpected state. Nevertheless, it could be found in a variety of thin film systems. Most prominent studies on the PMA involve Co/Au(111) [23, 25, 81], Fe/Ag(001) [82–85], Fe/Cu(100) [24, 86–89], Fe/Ag(001) [89], Ni/Cu(001) [31, 32, 61, 90–92], Ni/Cu(111) [90] and also superlattices of Co/Pd(111) [93, 94] and Co/Au(111) [95, 96]. Due to the dominance of the demagnetizing field, the PMA usually can only be found in a very restricted part of the parameter space, resulting in a spin-reorientation transition at its boundaries.

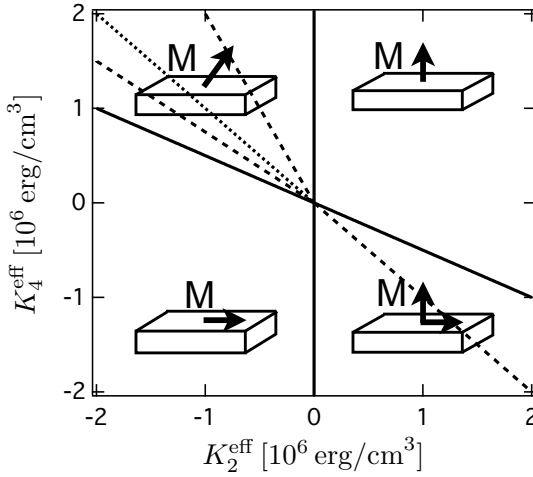


Figure 2.6 – Single-domain spin phase diagram in fourth-order depiction. Based on data from [76]

in the anisotropy flow concept [27, 28], evaluating magnetic orientation depending on K_2^{eff} and K_4^{eff} . Since both constants follow a $\sin^{2n}(\gamma)$ behavior, they prefer perpendicular magnetization for positive, and planar magnetization for negative values. Thus, the areas of opposite signs for the two constants are of particular interest. Energy minimization of the free energy from Eqn. 2.11 leads to different behavior for the two cases:

- Positive K_2^{eff} , negative K_4^{eff} : Two local energy minima for in-plane and out-of-plane magnetization angles are found for a certain range in the parameter space visualized in Fig 2.6. The depth of the energy minima for each magnetization direction changes continuously from out-of-plane to in-plane with decreasing K_2^{eff} , giving rise to a transition via a coexistence state.

The treatment of uniaxial anisotropy based on limiting the anisotropy constants to K_2^{eff} yielded results agreeing with experiments to understand the driving mechanisms to the PMA and SRT. However, based on K_2^{eff} only, the SRT is assumed to be a sharp transition. Experiments have shown continuous transitions depending on film thickness and temperature [97]. Inclusion of K_4^{eff} extends the parameter space allowing for continuous transitions to appear. The development of the uniaxial anisotropy throughout this parameter space has been addressed

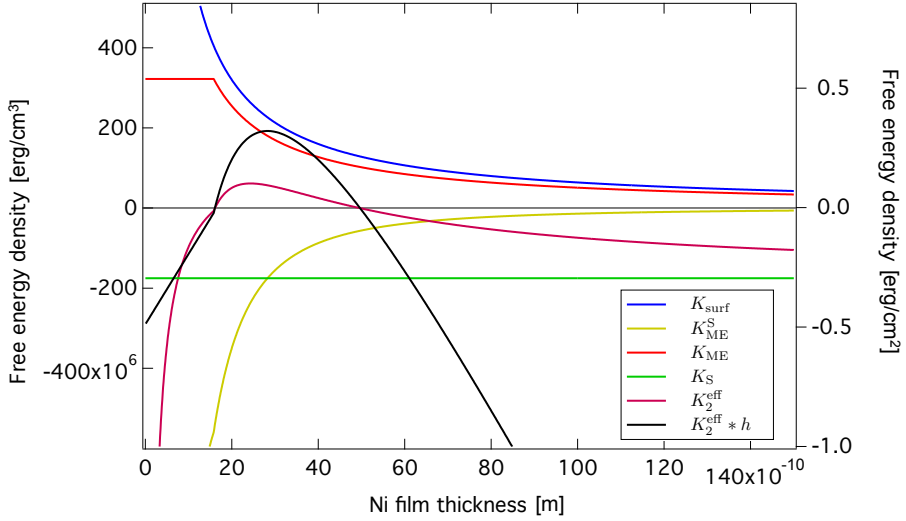


Figure 2.7 – Graphical representation of the anisotropy terms contributing to K_2^{eff} . Mathematical expressions are given in Eqn. 2.22. The black curve represents the anisotropy multiplied by the film thickness.

- Negative K_2^{eff} , positive K_4^{eff} leads to a single energy minimum of the free energy at a canted γ . The angle is continuously shifting from out-of-plane to in-plane geometry upon decreasing K_2^{eff} and K_4^{eff} .

The anisotropy space is depicted in Fig. 2.6 with marked regions of continuous SRTs and the respective magnetization direction. Studies on the nature of SRTs prove the validity of this model, as single-domain measurements showed the ability of magnetic materials to exhibit second order reorientation transitions for Ni/Cu(001) [97, 98], and Fe/Ag(100) [85].

2.2 Anisotropy and spin-reorientation transition in Ni/Cu(001)

Systems of Fe and Co films as discussed above exhibit a spin reorientation transition depending on thickness. For ultrathin films, the surface anisotropy is dominant and pulls the magnetization out of plane. At a critical thickness, typically between 1-5 ML, a spin reorientation transition takes place, originating from the decreasing influence of the surface anisotropy and the growing contribution of the shape anisotropy.

The system of Ni/Cu(001), however, has been shown to exhibit an inverse spin reorientation [32], and also a regular SRT for thicker films [31]. Up to 7 ML film thickness, the magnetization is in-plane, followed by a perpendicularly magnetized regime up to thicknesses of 35-70 ML. The magnetization is realigned in-plane in a second SRT. With reference to the anisotropy theory discussed in Sect. 2.1.3 and measurements determining the anisotropy constants for Ni/Cu/Si(001) [91, 97], the anisotropy contributions have been displayed in Fig. 2.7.

The in-plane magnetic anisotropy for thicknesses $h < 15 \text{ \AA}$ is driven by the negative average surface anisotropy, i.e. the sum of strain-dependent and strain-independent surface contributions for both vacuum/Ni and Ni/Cu interfaces $K_{\text{ME}}^{\text{S}} + K_{\text{surf}}$. A positive bulk magnetoelastic anisotropy dominates the effective anisotropy upon decreasing influence of the surface terms with increasing thicknesses up to 60 \AA . The negative magnetostatic anisotropy (demagnetizing field) becomes the leading term for thicknesses above 60 \AA resulting in the SRT from out-of-plane to in-plane magnetization. BOCHI et al. confirmed the same magnetic phases and sources for the Cu capped system Cu/Ni/Cu/Si(001) [91]. It is worth noting that the driving mechanism is completely of magnetic origin, as the morphology of the film is not considered in this model [99].

2.3 Magnetic domains & domain walls

The minimization of the free energy of a magnetic sample, given in Eqn. 2.22, yielded the existence of easy and hard axes. Also, the symmetry of these axes found an inversion of magnetization without change in overall energy. Areas of magnetization with different directions complying to one of the easy axis directions are called magnetic domains. The introduction of domains can decrease the stray field of a magnetic specimen, e.g. by compilation of a flux closure. However, the exchange energy prevents a spontaneous reorientation of magnetization complying to the easy axes, which results in an energetic cost caused by the magnetization rotation diverging from the easy axes at the border between the domains. These areas of continuous magnetization rotation between two domains aligned along the easy axes are called domain walls. Thus, domains will be formed if the additional energy from creating a domain wall will be overcompensated by the decrease in stray-field energy. In addition, external magnetic fields and the remaining terms from the anisotropy treatment in Sect. 2.1.3 form the basis of the micromagnetic approach to the domain state given by a minimization of the free energy. This approach will be subject of this section.

In order to define a magnetic domain state by the participating energies, a more so-

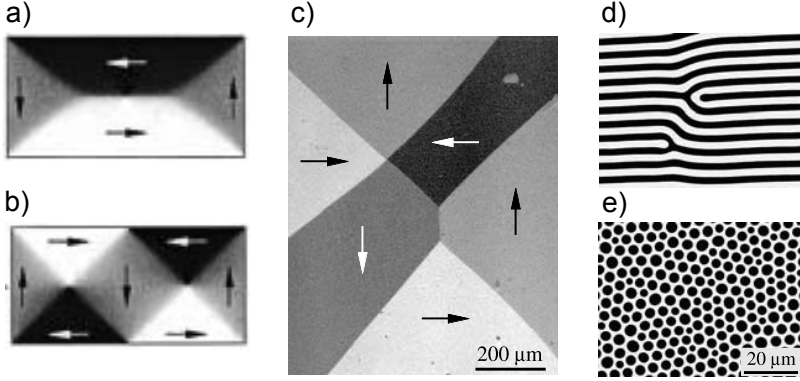


Figure 2.8 – Illustrations of the discussed domain patterns. (a) & (b) Numerically calculated equilibrium structures of a $(2 \times 1 \times 0.02) \mu\text{m}$ Permalloy thin film structure - LANDAU pattern and diamond state, respectively. Vortices can be seen at the center(s) of the structures. Taken from [100]. (c) Fe(100) oriented 40 nm films. A preference for 90° walls can be seen. Samples originally from GRUENBERG et al., taken from [34]. (d) & (e) domain patterns from a bubble garnet film at varied magnetic field. The film has a growth induced perpendicular anisotropy. Depending on the application of a magnetic field, saturating the film at different angles (20° or 1° respectively), the remanent domain structure formed in an energetic local minimum is different. Taken from [34]

phisticated description of the exchange energy is needed: The energy connected to the deviation of magnetic moments from the parallel alignment of magnetic moments is given by the "stiffness" expression [34]:

$$E_{\text{ex}} = A \int (\nabla \mathbf{m})^2 dV \quad (2.23)$$

with the material parameter A , called exchange stiffness constant, which is scalar for cubic or isotropic materials, and the reduced magnetization $\mathbf{m} = \mathbf{M}/\mathbf{M}_s$ (saturation magnetization \mathbf{M}_s).

The influence of an external magnetic field \mathbf{H}_{ex} , also called ZEEMAN energy, can, complementary to the demagnetizing field, be expressed as

$$E_{\text{H}} = -M_s \int \mathbf{H}_{\text{ex}} \cdot \mathbf{m} dV \quad (2.24)$$

Now, the free energy of a domain state can be expressed in a general form as sum of the

following contributions (which have partially been introduced in Sect. 2.1.3):

$$\begin{aligned}
E_{\text{tot}} &= \int [E_{\text{exchange}} + E_{\text{demag.}} + E_{\text{MC+S}} + E_{\text{ext.strain}} + E_{\text{ext.field}}] \, dV \quad (2.25) \\
&= \int \left[A(\nabla \mathbf{m})^2 - \frac{1}{2} \mathbf{H}_d \cdot \mathbf{M} + E_{\text{MC+S}} + \mathbf{B} \cdot \boldsymbol{\epsilon} - \mathbf{H}_{\text{ex}} \cdot \mathbf{M} \right] \, dV \quad (2.26)
\end{aligned}$$

where $E_{\text{MC+S}}$ denotes the energy related to magnetocrystalline and surface related anisotropies. The dot products can be replaced by their simplified expressions discussed in Sect. 2.1.3 for thin film uniaxial geometries under transformation of the integral over the film thickness.

The domain state's manifestation strongly depends on the local interplay between the terms in Eqn. 2.26, resulting in complex domain formations of various appearances. In the first instance, the domain implementation depends on the balance of the short ranged exchange energy and the energy connected to the demagnetizing field and anisotropy terms on a longer range. As a result of the exchange energy, the magnetization rotation in a domain wall has to be continuous, while the demagnetizing field and anisotropy would prefer a spontaneous realignment complying to the easy axes of the system.

In order to gain an understanding of the interplay between the terms, three examples will be discussed in the following:

- **Thin film elements** of soft magnetic materials [magnetic materials which only need small external fields to remove a remanent magnetization (low coercivity)], tend to spontaneously minimize the free energy by employing flux closure domain patterns called diamond patterns. An in-plane magnetized thin film element would create stray fields outside of its element's boundaries in a single-domain state, which can be avoided if the magnetization is organized parallel to the closest border of a given point in the element. If the film element is small enough, this structure involves a point of perpendicular magnetization in its center, a so called vortex. At larger sizes, a 180° wall is formed in the center. An example for a LANDAU pattern (i.e. a single diamond) can be seen in Fig. 3.8 a). If the film element's size is increased, the LANDAU pattern is replaced by diamond patterns (Fig. 3.8 b), since the 180° wall in the center is energetically unfavorable, whereas the diamond structure mostly involves 90° walls and only shorter 180° wall parts [100].
- **Iron**, the model system for **bulk cubic crystals with two easy axes in the surface**, exhibits a clear pattern of in-plane magnetized domains (Fig. 2.8 c)). The flux closure patterns known from thin film elements are predominant in the arrange-

2 Fundamental aspects

ment of domains, minimizing the energy in a general flux closure. This dominating occurrence is easily disturbed if the domains get larger. Hence, domain walls are introduced to create domains, creating a local stability. Since the wall energy for 90° walls is lower than 180° walls, mostly the former can be found. The invested domain wall energy and the local flux closure, reducing the magnetostatic interaction, result in an equilibrium domain formation and size.

One has to note that the local variations also result in preferences of a specific easy axis, as reported from studies on Fe samples where an additional demagnetizing cycle has been performed between two measurements. While the domains are reordered, most areas are magnetized along the same axis as before the demagnetizing [34].

- A typical domain configuration of **positive anisotropy films** involves formation of parallel stripe domains (see Fig. 2.8 d)). Obviously, domains are introduced to minimize the stray field that extends out of the sample. The magnetic field is closed between the magnetic poles at the surface or interface of the sample. The stripe pattern is characterized by a long range order of the stripes and their width, which is given by an equilibrium between the increase of overall domain wall energy and the reduction of the stray field when increasing the stripe density.

In the same geometry, bubble lattices can form under an applied field, since they are a metastable configuration of such films (see Fig. 2.8 e)). The underlying bubble lattice ideally is formed in a hexagonal, close-packed structure, but will deform in the presence of in-plane anisotropies [34].

As can be seen from the examples above, the energy of domain walls is a crucial parameter for the observation and the detailed manifestation of a domain state. The two most prominent types of 180° domain walls will be discussed in the following. The BLOCH and NÉEL walls both describe a magnetization transition between two domains with an antiparallel magnetization. While the rotation direction of the magnetic moments lies in the plane of the wall for BLOCH-walls, the rotation for NÉEL-walls is perpendicular to the wall. Both domain wall magnetization rotations are depicted in Fig. 2.9.

The energy of a 180° domain wall is given by

$$E_W = 2\pi\sqrt{AK} \quad (2.27)$$

with the exchange stiffness A , a material specific parameter depending on the crystallographic structure and the exchange integral J , hence defining the interaction strength of

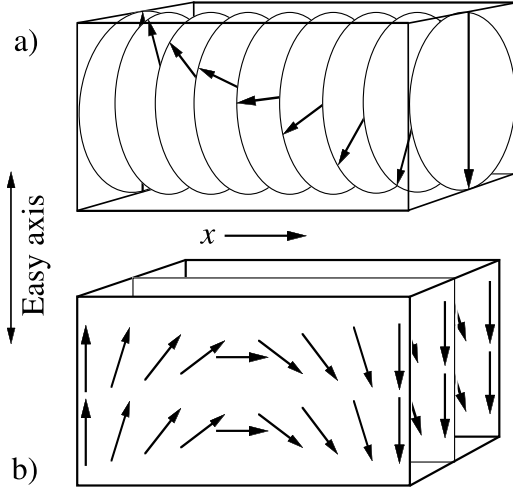


Figure 2.9 – Schematic of BLOCH-wall (a) and NÉEL-wall (b). Magnetic domains are to the left and right of either schematic, magnetized up and down, respectively. The opposite rotations of either depicted wall is equally possible. From [34]

neighboring spins [70]. The width of a 180° wall is depending on a more complicated set of properties. As domain walls are continuous rotations of the local magnetization, the definition of the wall length cannot be unique. Based on the slope of the magnetization angle $\gamma(x)$, the classical definition by LILLEY [101] leads to

$$W_L = \pi \sqrt{A/K} \quad (2.28)$$

for a 180° BLOCH wall. An elaborate discussion can be found in the textbook by HUBERT & SCHÄFER [34].

2.4 Photoemission process & XMCD

Photoemission is the effect of energy transfer from photons to matter, resulting in photoelectrons that are able to leave the illuminated material. The effect was discovered back in 1905 with the explanation of the photoelectric effect by EINSTEIN [102]. The first spectroscopic experiments making use of the photoelectric effect were carried out by SIEGBAHN in 1950, who used x-rays to analyze bonding states connected to chemical shifts, hence naming the the technique 'Electron Spectroscopy for Chemical Analysis (ESCA)' [103].

Nowadays, diverse experiments satisfying wide interests revolve around the same physical

2 Fundamental aspects

principle, which will be discussed with respect to its application in this thesis. Here, with emphasis on the x-ray magnetic circular dichroism (XMCD) effect, the dependence on the angle between magnetization and incident light can be used as a contrast mechanism, as will be discussed further in Sect. 3.2.2 in the context of the microscopes imaging modes.

Einstein's energy relation of the photoeffect links the energy of a photon $E_{ph} = h\nu$ to the binding energy of the electron E_{bin} , the potential barrier of a solid called work function Φ and the electron's final kinetic energy E_{kin} :

$$h\nu = \Phi + E_{\text{kin}} + E_{\text{bin}} \quad (2.29)$$

The quantum mechanical description of the photoexcitation, FERMI's Golden Rule, specifies the transition probability to excite an electron from an initial state $|i\rangle$ with the energy E_i to a final state $|f\rangle$ with the energy E_f [104, 105]:

$$P_{i \rightarrow f} = \frac{2\pi}{\hbar} |\langle f | \mathbf{O} | i \rangle|^2 \delta(E_f^N - E_i^N - h\nu), \quad (2.30)$$

Energy conservation is granted by the δ -function, in accordance to Eqn. 2.29. The transition probability is given by the transition matrix element $M_{fi} = \langle f | \mathbf{O} | i \rangle$, which depends on the interplay of wave function symmetry and the photonic operator. As a result of the Golden Rule and application of suitable approximations, the so called dipole selection rules are obtained [47], which allow for a simple evaluation of the transition possibility based on quantum numbers $|n, l, m_l, s, m_s\rangle$ defining an electron state as presented in the following.

The transition matrix element can be split into a radial-, angular- and spin-dependent part [70] in consideration of illumination by polarized photons:

$$M_{fi} = \underbrace{\langle n'l | r | nc \rangle}_{\text{radial}} \underbrace{\langle lm_l | \mathbf{e} | cm_c \rangle}_{\text{angular}} \underbrace{\delta(m'_s, m_s)}_{\text{spin}} \quad (2.31)$$

if atomic wave functions are used for symmetry determination. In this approach spin-orbit coupling, and hence spin-orbit splitting of the levels, is neglected for the explanatory purpose. Primes denote initial states, c denotes the initial orbital quantum number from the core state and $|s = 1/2, m_s\rangle$ denotes the spin state of the electron. The δ -function handling the spin-part discloses that a non-vanishing transition probability only exists for $m'_s = m_s$, i.e. the spin has to be conserved. The radial dipole matrix element is

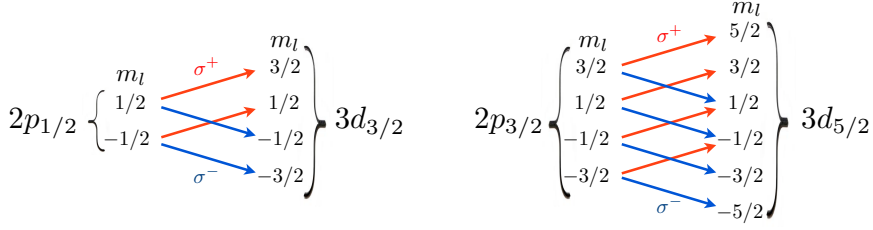


Figure 2.10 – Allowed transitions from the 2p to the 3d levels according to the dipole selection rules and $\Delta l = +1$. The allowed transitions depend on the given polarization of the exciting photon. From [108]

given by

$$\mathcal{R} = \langle n'l|r|nc \rangle = \int_0^\infty R_{n',l}^*(r) R_{n,c}(r) r^3 dr, \quad (2.32)$$

where the radial part of the electron wavefunction $R_{nl}(r)$ has to obey the normalization condition

$$\int_0^\infty |R_{nl}(r)|^2 r^2 dr = 1. \quad (2.33)$$

In general, the angular part involves a summation over the Racah operator $C_q^{(1)}$ [70], while it yields the atomic dipole selection rules by evaluation of the non-vanishing matrix elements in the dipolar approximation:

$$\Delta l = l' - l = \pm 1, \quad (2.34)$$

$$\Delta m_l = m'_l - m_l = q = 0, \pm 1, \quad (2.35)$$

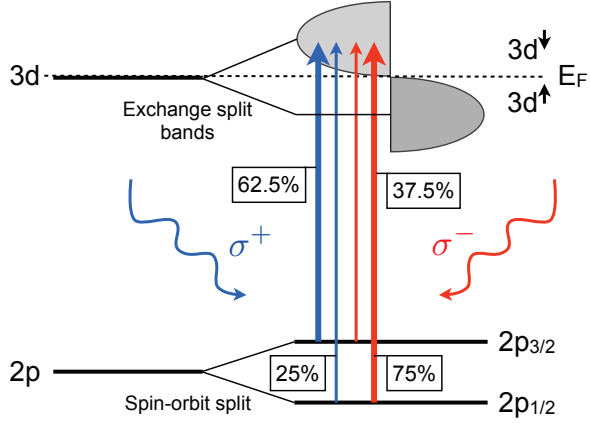
$$\Delta s = s' - s = 0, \quad (2.36)$$

$$\Delta m_s = m'_s - m_s = 0 \quad (2.37)$$

with the angular momentum $q\hbar$ of the incident x-ray. The selection rules and their application in photoemission spectroscopy (the so called sum rules to determine the orbital and spin magnetic moment) have been deduced in full generality for the angular momenta by THOLE et al. [106] and for the spin by CARRA et al. [107].

Allowed transitions from 2p→3d levels are depicted in Fig. 2.10 according to Eqn. 2.35.

Figure 2.11 – Schematic XMCD effect in a single electron picture with large exchange-splitting in the d-bands (filled majority band, empty minority band). Transitions are shown for $2p \rightarrow 3d$ levels in exchange split 3d transition metals upon excitation by circularly polarized light. The angular momentum of the photons gives rise to the application of dipole selection rules resulting in the denoted transition probabilities. Transitions into the majority band do not find possible final states and are hence not occurring.



Circularly right polarized photons (σ^+) conform to $\Delta m_j = +1$ while circularly left polarized photons (σ^-) conform to $\Delta m_j = -1$, where $m_j = m_l + m_s$ with $|m_l + m_s| \leq j = |l \pm s|$.

The transition probabilities can be calculated by use of the CLEBSCH-GORDON-coefficients to evaluate the products of spherical harmonics emerging from the electron wavefunctions. For the transitions of interest for this thesis, the transition probabilities from $2p \rightarrow 3d$ levels are denoted in the XMCD transition scheme in Fig. 2.11, for the case the propagation vector \mathbf{k} of the photon is parallel to magnetization direction. Hence, circularly right (left) polarized light excites 75% spin \downarrow (37.5% spin \uparrow) electrons from the $2p_{1/2}$ level and 25% spin \downarrow (62.5% spin \uparrow) electrons from the $2p_{3/2}$ level to the $3d$ \downarrow level. In addition, the absolute amount of excited electrons is depending on the population of electrons from the spin-orbit split initial level. The difference of the intensities of excited electron sums constitutes the x-ray magnetic circular dichroism:

$$\Delta I = I(\sigma^+) - I(\sigma^-) \quad (2.38)$$

2.5 Electron inelastic mean free path

The electron inelastic mean free path (eIMFP) is an important physical quantity in connection to photoemission and the experiments conducted in this thesis. Electrons

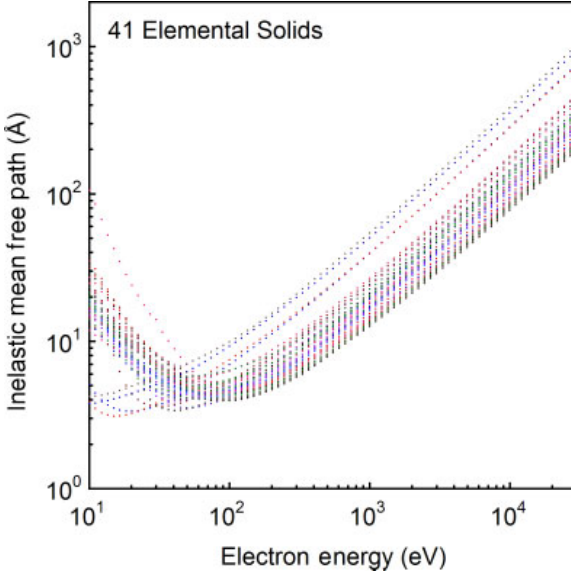


Figure 2.12 – Inelastic mean free paths for electrons in the energy range of 10 eV to 20000 eV calculated for 41 elemental solids, corresponding to different colors. From [109]

that travel through solid material with a kinetic energy E_{kin} , e.g. photoelectrons, will experience elastic and inelastic scattering events, leading to changes in the electron momentum and energy. The inelastic mean free path, the mean travel length without scattering events, determines the probing depth of electron measurement techniques. The probability of scattering events is determined by the solid's composition and the kinetic energy of the electron. A general trend in the so called universal curve finds a minimum eIMFP of $<10 \text{ \AA}$ between 50 eV and 100 eV. For higher and lower kinetic energies, increasing eIMFPs are found. The traveling electrons lose their energy by plasmonic scattering, electron-hole formation, and vibrational excitation [110]. The decay in electron intensity can be expressed as

$$I(l) = I_0 \exp\left(-\frac{l}{\lambda_{IMFP}}\right), \quad (2.39)$$

where l denotes the electron intensity and λ_{IMFP} the mean free electron path [111]. Approximately, the eIMFP can be calculated by

$$\lambda_{IMFP}[\text{\AA}] \approx \frac{14.3}{\sqrt{E}} + 0.54\sqrt{E}; \quad E \text{ in eV} \quad (2.40)$$

2 Fundamental aspects

Modern simulations for the eIMFP, yielding good agreement with previous measurements from the same group [112], can be found in Fig. 2.12.

The eIMFP will be used in the further course of the thesis as a tool to determine the film thickness in a wedged sample geometry (Sect. 5.1.1) and also needs to be incorporated when determining the film composition by AUGER electron spectroscopy due to the varying kinetic energies of the electrons (Sect. 3.1.2). However, the influence of the eIMFP is of different nature in the two cases. The AUGER electrons are direct electrons which are measured at energies corresponding to only elastically scattering events, which means a direct application of the eIMFP. Electron energies in the typical range of 200 – 1000 eV result in eIMFPs of about 1 – 10 nm.

In the x-ray absorption experiment (see Sect. 3.2.2), the secondary electron cascade is measured as a signal proportional to the absorption. The energy transfer between scattering electrons results in much lower energies of about 0 – 5 eV and corresponding to eIMFPs of about 0.5 – 20 nm [113].

3 Experimental methods & setup

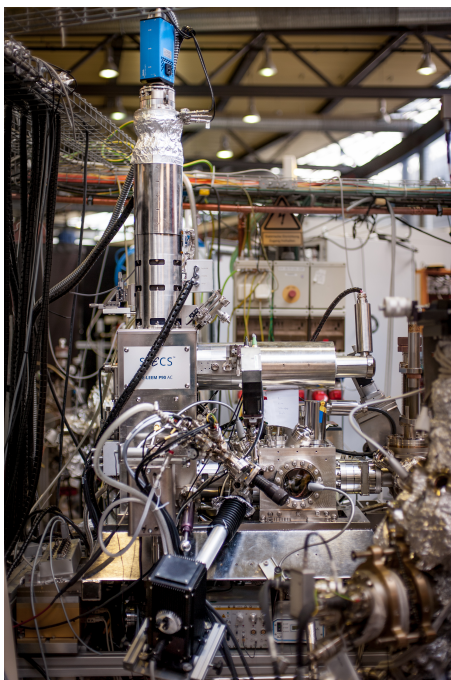


Figure 3.1 – The FE-LEEM P90 at the FZ Jülich beamline UE56/1-SGM, BESSY II, Berlin, Germany

In order to gain a deeper knowledge about the SRT and the domain structure depending on the anisotropy parameters in $\text{Ni}/\text{Cu}(001)$ and $\text{Ni}_x\text{Pd}_{1-x}/\text{Cu}(001)$, we conducted all experiments utilizing an FE-LEEM P90 [114–117] instrument with aberration corrector, commercialized by SPECS Surface Nano Analysis GmbH [118, 119]. The microscope is operated as a permanent end-station at the Forschungszentrum Jülich’s soft x-ray beamline UE56/1-SGM at the synchrotron facility BESSY II, Berlin, Germany. An attached preparation chamber allows for in-situ preparation of the wedged $\text{Ni}_x\text{Pd}_{1-x}$ films on $\text{Cu}(001)$. For this purpose, the preparation chamber is equipped with a 5-axis manipulator with electron beam-heating, a low-temperature pyrometer for temperature readout (250-1400°C), an Ar^+

ion beam source and two distinct evaporators (Sect. 3.1.1). For characterization purposes the preparation chamber accommodates dedicated systems for AUGER electron spectroscopy (Sect. 3.1.2), low energy electron diffraction (Sect. 3.1.3), and the possibility to determine film thickness and growth mode during evaporation by medium energy electron diffraction (Sect. 3.1.4).

In the second part of this chapter a descriptions of immersion microscopy in general, and

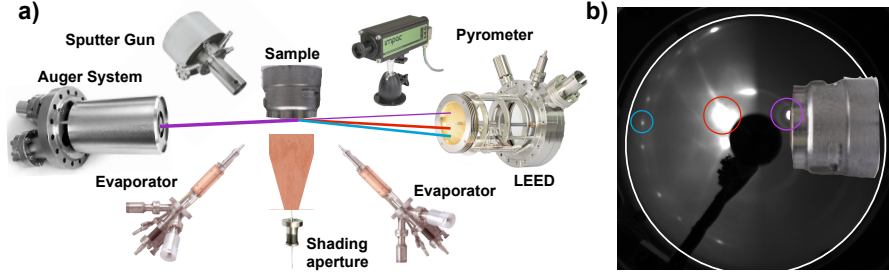


Figure 3.2 – Sketch of the preparation chamber’s layout (a). MEED pattern during evaporation (b). Color marks correspond to incident electron beam (purple), used for normalization purposes, direct reflection (red), used for recording the MEED oscillations and first order diffraction (cyan).

of the microscope used in the studies for this thesis in particular are given (Sect. 3.2). A particular focus is put to the aberration corrector in Sect. 3.2.1 as a novel commercially available feature. The imaging modes of the microscope are discussed in Sect. 3.2.2. Synchrotron radiation, as the main illumination source used for experiments, is discussed in Sect. 3.2.3, also characterizing the beamline UE56/1-SGM at BESSY II, Berlin. In the course of this study, in-situ demagnetization via electromagnets has been established and image rotations for typical magnifications have been determined, and are described in Sect. 3.2.4 and Sect. 3.2.5, respectively.

3.1 Preparation

3.1.1 Molecular beam epitaxy

Clean and monocrystalline samples are mandatory to study the role of lattice stress on the anisotropic behavior of magnetism. Molecular beam epitaxy excels in slow evaporation rates and clean deposition below 5×10^{-10} mbar, both endorsing epitaxial growth of clean ultrathin films. Technically, the evaporand, in the form of a 2 mm diameter rod, is brought to sublimation temperature by electron beam heating. An exit tube, incorporating a flux monitor and a shutter, directs the sublimated atoms towards the sample, where the growth mode is determined by a set of parameters: deposition rate, temperatures, residual gases, and individual atomic processes [120]. In a thermal equilibrium (high adsorbate mobility, low deposition rate), the growth process is mainly determined by the chemical interaction between substrate and adsorbate. BAUER [121] first reviewed thin film growth modes depending on the surface free energies of the adsorbate

γ_a , the substrate γ_s and the interface layer γ_i . Three growth modes are discussed in this framework:

- $\gamma_s \geq \gamma_a + \gamma_i$ & small lattice mismatch (FRANK-VAN DER MERWE growth). An adsorbate layer is completed before atoms adsorb in a second layer on top, constituting a layer-by-layer growth mode.
- $\gamma_s < \gamma_a + \gamma_i$ (VOLMER-WEBER-growth), an island growth mode. As reflected by the energy relation it is more energy efficient for the film to create three dimensional islands instead of completing layers.
- $\gamma_s \geq \gamma_a + \gamma_i$ & significant lattice mismatch (STRANSKI-KASTRANOV growth). After a first wetting (mono-)layer, the strain leads to a preferred island formation for subsequent growth.

As RUGGERONE et. al. described, usually the system will not be in a perfect thermal equilibrium, and the resulting film morphology is also determined by kinetic processes [122].

However, for the present work, the influence of lattice strain on the growth needs special attention. As the bulk lattice constant of a deposited material usually is not the same as found for the substrate, the grown film will be strained. The corresponding parameter, the lattice mismatch η , can be described with the lattice constant of the substrate $a_{\text{substrate}}$ and the bulk lattice constant of the deposited film a_{film} [123]:

$$\eta = \frac{a_{\text{film}} - a_{\text{substrate}}}{a_{\text{substrate}}} \quad (3.1)$$

The adoption of the substrate lattice constant for the first monolayers of the deposited film is called pseudomorphic growth, transcribing the term from the mineralogy 'replacer after original'. In this initial phase, the film is under an in-plane biaxial tensile strain given by the lattice mismatch $\epsilon_0 = \eta$, leading to POISSON-compression/expansion of the unit cell along its normal given by $\epsilon'_0 = -\eta$, assuming a POISSON's ratio $\nu = 1/3$ and an elastically isotropic film [75, 124]. The pseudomorphic growth prevails until it is energetically more favorable to reduce the strain by implementation of misfit dislocations. The energy connected to the strain is proportional to the volume V and can be described by HOOK's law:

$$E_H = \frac{1}{2} C \epsilon_0^2 V \quad (3.2)$$

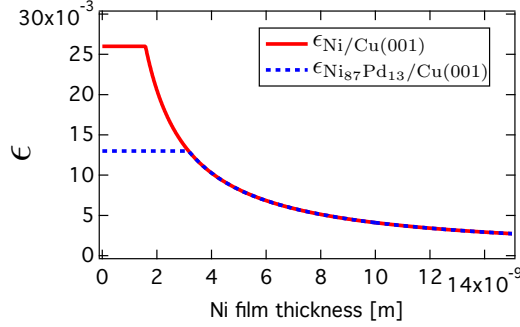


Figure 3.3 – Theoretical calculation of the strain in an epitaxially grown Ni/Cu(001) and Ni₈₇Pd₁₃/Cu(001), deduced from Eqns. 3.4 & 3.5

where C denotes the elastic constant. The sum of strain energy and energy cost of incorporating misfit dislocations to relax the strain E_{MD} ,

$$E_S = E_H + E_{MD}, \quad (3.3)$$

will be minimized by the system, leading to a constant strain in the film until a critical thickness h_c is reached [125]. This critical thickness h_c can be mathematically determined if information about the BURGERS vector [126] (representing the magnitude and direction of the lattice distortion) and the misfit dislocation properties is present [127]. The development of strain relaxation for films thicker than h_c , given by the minimization of Eqn. 3.3, can be approximated by a $1/h$ law as proposed by the model of CHAPPERT and BRUNO [73]:

$$\epsilon_0(h) = \eta \frac{h_c}{h}, \quad h > h_c \quad (3.4)$$

$$\epsilon_0(h) = \eta, \quad h \leq h_c \quad (3.5)$$

The model predicts a constant strain for epitaxial films up to thicknesses of h_c and a decreasing strain for higher thicknesses. The $\epsilon_0(h)$ function is depicted in Fig. 3.3 for the Ni/Cu(001) system studied in this thesis and determines the shape of the strain-dependent anisotropy contributions in Ni/Cu(001) depicted in Fig. 2.7. Under the assumption of a constant volume V of the atomic unit cell, the lattice constant in the

perpendicular direction has to increase according to

$$a^2 + a^2 + c^2 = V^2 = \text{const.} \quad (3.6)$$

with the in-plane lattice constant a and the perpendicular lattice constant c in a tetragonally strained cubic system.

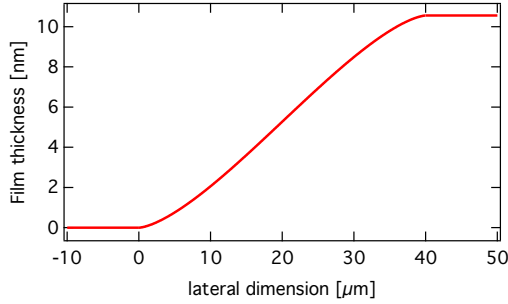


Figure 3.4 – Theoretical calculation of the wedge shape, deduced from Eqn. 3.7

Wedge deposition Part of the samples made for this thesis are grown in a wedge geometry. This is accomplished by an aperture shadowing technique, realized by a razor blade which is brought close to the sample where it resides throughout the evaporation process. For a finite size of the evaporand or the evaporators opening muzzle, whatever limits the vapor beam size, the theorem of intersecting lines results in a

wedged film. The final wedge shape $W(x)$ is given by the integration of the vapor beam shape:

$$\begin{aligned} W(x) &= 2 * \int \sqrt{1 - x^2} dx \\ &= \arcsin(x) + x\sqrt{1 - x^2} \end{aligned} \quad (3.7)$$

The width of the wedge is given by the theorem of intersecting lines, resulting in $\sim 33 \mu\text{m}$ (15 cm muzzle-aperture distance, 0.1 cm aperture-sample distance, 0.5 cm muzzle opening), while experimental determinations yielded 30-80 μm . This deviation is most likely given by the imperfect placement of the aperture in-situ. The wedge shape is shown in Fig. 3.4, scaled to fit actual measured wedge dimensions. The resulting wedge's inclination in this geometry and for a 100 ML film is less than a monolayer (Ni: 0.176 nm) per 400 nm.

3.1.2 Auger electron spectroscopy (AES)

3 Experimental methods & setup

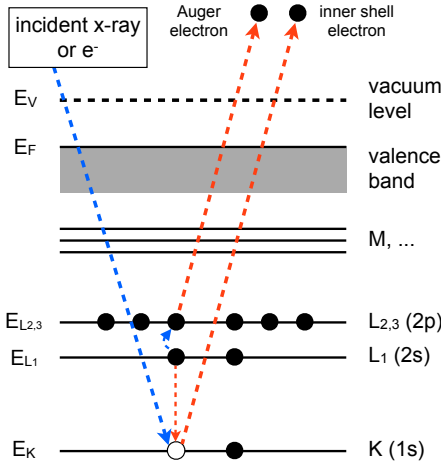


Figure 3.5 – Illustration of the AUGER process.

AUGER electron spectroscopy (AES) is a method used to determine the chemical composition of a sample with a shallow information depth given by the electron IMFP of the measured electrons (about 1 nm). AUGER spectra register a unique energy signature of emitted electrons from each element because of the energy transfer mechanism during the AUGER process. This process can be described in the following model [128, 129]:

- An electron from a core shell is removed by either an incident electron or photon, ionizing the atom.
- The core hole is filled by an electron from an outer shell.
- The difference in binding energy is transferred to another electron, which eventually is emitted from the sample.

Also see Fig. 3.5 for an illustration of the AUGER process. The transferred energy E_{i-f} is specific to the energy gap between the two shells participating in step 2. Hence, the emitted electron can then be measured at a kinetic energy of

$$E_{kin} = E_{i-f} - E_{bin} - \Phi, \quad (3.8)$$

taking also into account the binding energy of the emitted electron E_{bin} and the work function of the material Φ . In step 3., fluorescence is a competing mechanism to release the excess energy. The total amount of core hole decays is comprised as a sum of fluorescence and AUGER effect, with the amount of fluorescence increasing with increasing atomic weight [130].

In the dedicated AES system used for this thesis, the sample's electrons are excited by an incident electron beam of 3-5 keV energy. AUGER electrons are energy filtered in a single-pass cylindrical mirror analyzer and detected by a channeltron using a lock-in technique to improve the signal-to-noise ratio. Thus, spectra are displayed as a

derivative of energy dN/dE . As AES yields element specific information, it is used to detect contaminations and adsorbates of a sample and also to determine the thickness of deposited films. The damping of the substrate AUGER signal can be related to the grown film thickness. As used in the context of this thesis, AES is most suitable to determine the chemical composition of a mixed film, e.g. the alloys prepared for this study. Here, film thickness has to be determined separately, for example by MEED oscillations during film growth as described in Sect. 3.1.4. The electron yield of elements A and B is attenuated proportional to respective eIMFP $\lambda_{A,B}$. Also the thickness h of the film has to be taken into account. The composition regarding element A can be expressed as [66]:

$$x_A = \frac{\frac{I_A}{S_A} (1 - \exp(-d/\lambda_B \cos \Theta))}{\frac{I_A}{S_A} (1 - \exp(-d/\lambda_B \cos \Theta)) + \frac{I_B}{S_B} (1 - \exp(-d/\lambda_A \cos \Theta))} \quad (3.9)$$

where $I_{A,B}$ denotes the measured peak-to-peak heights from the derived AUGER spectrum and $S_{A,B}$ are the so called sensitivity factors. The sensitivity factors take the cross-section of the AUGER process into account, but also the sensitivity of the AUGER spectrometer itself, given by geometrical differences of each system. Therefore, the sensitivity factors have to be determined for each system uniquely by recording reference spectra. The $\cos \Theta$ is introduced to compensate the effect of the angle of incidence on the information depth (see eIMFP in Sect. 2.5). Eqn. 3.9 is idealized for pseudomorphic growth and incident electron energies much larger than AUGER electron energies.

3.1.3 Low energy electron diffraction (LEED)

Low energy electron diffraction (LEED) is a method used to determine the long range crystallographic structure of a material by diffraction of a collimated electron beam of low energy (5-400 eV) [131]. Due to the short eIMFP (Sect. 2.5) of the electrons, LEED is a very surface sensitive experiment. The electrons elastically scattered on the lattice give rise to diffraction spots which can be viewed on a fluorescent screen. Due to the wave nature of accelerated electrons, constructive interference occurs according to BRAGG's law

$$2d \sin \Theta = n\lambda \quad (3.10)$$

where n is an integer, λ the corresponding wavelength of the incident electrons, d the lattice constant perpendicular to the surface, and Θ the angle between incident and

3 Experimental methods & setup

diffracted electrons. As the emerging pattern is a reciprocal reconstruction of the diffracting crystallographic structure, it can be used to determine crystallographic structure's unit cell directions in real space.

While the determination by BRAGG's law is sufficient for a phenomenological description, generally, the strong multiple elastic scattering of electrons into all possible directions has to be taken into account. Dynamic calculations of LEED scattering processes are able to reproduce the intensity fluctuations of LEED spots depending on incident electron energy, called LEED I(V). These intensity curves are the basis of any quantitative LEED experiment and yield information about the exact structure of the crystallographic unit cell up to an error limit of $\pm 0.01 \text{ \AA}$ [132].

The spot size is determined by the the long-range order of contributing scattering centers. The spot-to-background brightness ratio may be related to lattice defects, dislocations, adsorbed atoms, and surface roughness. This can be used to distinguish between local disorder (e.g. temperature-related), poor long-range order, and superlattices. Additionally, the brightness distribution in the spot profile can be used for further analysis, including the aforementioned LEED I(V) experiments.

3.1.4 Medium energy electron diffraction (MEED)

Medium energy electron diffraction (MEED) is a method used to determine thin film thickness during evaporation for samples growing in a layer-by-layer fashion in UHV. An electron beam of medium energy (1-3 keV) is focused on the sample with an incident angle of $1-5^\circ$, with respect to the sample plane, for a high surface sensitivity. The scattered electrons create a diffraction pattern on a phosphor screen, which can be recorded by a CCD camera. The intensity of the elastic spot scales with the roughness of the sample due to decreasing reflection for rougher sample surfaces: For layer-by-layer growth the roughness is minimal once a layer is completed and at a maximum for half a completed layer, which corresponds to the opposite in reflected intensity. The resulting intensity oscillations of the elastic peak thus allow for growth monitoring during film growth. However, certain growth modes prevent MEED oscillations even though layer-by-layer growth is persistent. Step-flow growth, where high mobility of the adatoms results in diffusion to atomic steps, might be the most prominent example [133]. The development of MEED oscillations, i.e. damping and height of oscillations, gives hints on the prevalent growth mode. MEED is a most suitable technique for thin-film growth because of its high signal-noise ratio due to the intensity of the elastic peak, and its accuracy of monolayer determination. Lower electron energy than used for

RHEED (reflection high energy electron diffraction) results in a more surface sensitive measurement because of the reduced eIMFP [111].

All MEED measurements shown in this study have been normalized to the reflected intensity before evaporation shutters were opened and the background intensity. Also, we will refer to results from previous publications that have been correlated to MEED oscillations. In our system, we arranged the AES- and LEED system opposite to each other in a geometry suitable for MEED during film deposition (see Fig. 3.2).

3.2 Photoemission & low energy electron microscopy

Electronic immersion microscopy has its origin in a method published in the 30s by BRUECHE [134,135]. By using an electrostatic accelerating field as an analogon to the immersion fluid known from optical microscopy, he increased the imaging capabilities of his microscope. This principle can be found in all electron microscopes up to the latest generation and is typically realized by a cathode lens (see also Fig. 3.12). A positive potential of 5-20 kV between the front part of the objective lens (extractor) and the sample (cathode) creates the electrostatic 'immersion-' field. The emitted photoelectrons will be accelerated to a drift-energy $E_d = E_0 + eU$, which reduces the relative energy-spread. This reduction helps to increase the microscope's resolution by reducing angles with the optical axis and reducing the influence of electronoptical imperfections. In this kind of design the sample itself is part of the immersion lens [136]. Another common part in electron immersion microscope design is the projector, a set of lenses which magnifies the image created by the objective lens to a detector, for example a phosphor screen. Digital conversion of the image can be achieved by a CCD camera.

Electron microscopy has seen various inventions, improvements and specializations to suit multiple unique purposes, resulting in different techniques. The most prominent representatives are (scanning) transmission electron microscopy [(S)TEM] [137, 138], scanning electron microscopy (SEM) [139], photoemission electron microscopy (PEEM) [140], and low energy electron microscopy (LEEM) [141]. As the names suggest, main differences lie in creation of the image-forming electrons and their energy. Due to the IMFP of electrons in condensed matter this also determines the probing depth of the microscopic design. (S)TEM is operated at electron energies of 100 keV to 1 MeV, therefore resulting in a bulk sensitivity, also characterized by its transmission design. However, samples have to be made specifically thin (typically 5-150 nm [137]) for transmission techniques. LEEM and PEEM on the other hand operate at electron energies < 100 eV, which is connected to probing depths of typically < 10 nm (see Fig. 2.12). The micro-

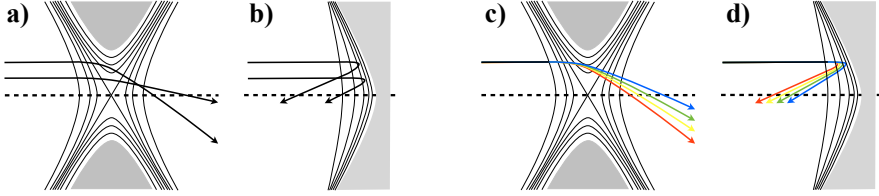


Figure 3.6 – Spherical and chromatic aberration of an electron lens (a) & (c), and an electron mirror (b) & (d). Notably, the aberrations of lenses and mirrors are of opposite sign. From [108]

scope used for this study is a combined LEEM/PEEM-machine operated as stationary end-station at the synchrotron facility BESSY II, Germany. In PEEM mode the sample is illuminated by photons under an angle of about 25° , the secondary electron cascade of the excited photoelectrons is used for image formation. In LEEM mode, a monochromated and collimated electron beam is focused onto the sample at normal incidence. The image is formed by electrons reflected or diffracted at the sample. Even though the contrast mechanisms in these two techniques are quite different, the electron optical imaging process is very similar since the imaged electrons are of similar kinetic energy when they leave the sample.

3.2.1 Optics for immersion lens microscopy

The most important optical parameters and modes of immersion lens microscopy in general and the present microscope specifically will be elucidated in this section. A discussion is needed since lenses cannot be designed without optical limitations, resulting in the disability to focus all electrons emerging from the same spatial point to the same point in the imaging plane, due to various reasons. A reproduction of the exact details would be beyond the scope of this thesis, hence interested readers are forwarded to find all information calculated in the framework of the contrast-transfer-function method by SCHRAMM et al. [117] for the design of the used microscope.

Cathode lens An exhaustive description of optical aberrations of cathode lenses has been given by Krivanek [142] in 2009. However, after carefully setting up a microscope, resulting in a defocus-, tilt-, and coma-free and a for astigmatism corrected imaging condition, the limiting aberrations are of spherical and chromatic nature, which will be the focus of the following paragraph.

Spherical aberration occurs when electrons pass an optical element outside its center.

The geometry of spherical lenses doesn't keep the refractive index constant for peripheral areas. The path of the electrons through a lens exhibiting spherical aberration is sketched in Fig. 3.6 a). The resulting offset in focal distance δ can be described by an expansion:

$$\delta_s = C_1\alpha + C_3\alpha^3 + C_5\alpha^5 + \dots \quad (3.11)$$

where α is the acceptance angle of the lens (usually restricted by a contrast aperture, see Fig. 3.12), C_1 the defocus of the lens and C_{2n+1} (for integer $n \geq 1$) are the aberration coefficients of $2n + 1$ st order. The coefficient of third order is called spherical aberration coefficient.

Chromatic aberration, as depicted in Fig. 3.6 c), is caused by a dependence of the refractive index of optical materials on kinetic energy of imaged waves and particles. The resulting offset δ_c can be expressed as an expansion

$$\delta_c = C_c\alpha\varepsilon + C_{cc}\alpha\varepsilon^2 + C_{3c}\alpha\varepsilon^3 + \dots \quad (3.12)$$

with the chromatic aberration coefficients C_{nc} of n -th order. One can see that the displacement is proportional to $\varepsilon = \Delta E/E$, the relative energy spread of imaged electrons.

Following NICKEL [108] leads to a definition of the radius for the circle of confusion caused by aberrations and diffraction $\delta_d = 0.61\lambda/\sin \alpha$:

$$r = \left[\left(\frac{0.61\lambda}{\alpha} \right)^2 + \left(\frac{C_3\alpha^3}{2} \right)^2 + (C_5\alpha^5)^2 + (C_c\alpha\varepsilon)^2 + (C_{cc}\alpha\varepsilon^2)^2 + (C_{3c}\alpha^3\varepsilon)^2 \right]^{\frac{1}{2}} \quad (3.13)$$

satisfying the relation $r = \sqrt{\delta_D^2 + \delta_s^2 + \delta_c^2}$, featuring leading terms of the expansions for an in-focus image ($C_1 = 0$) and small angles α .

For systems consisting of several lenses, aberrations can simply be added. However, aberrations from lenses following in the path of light have to be multiplied by $1/M^n$, M being the magnification of the preceding lens and $n = 4$ for spherical and $n = 2$ for chromatic aberrations. This shows the importance of the discussion of the cathode lens, being most influential on aberration-restricted resolution, while projection lenses are of negligible influence. A graphical representation of Eqn. 3.13 can be found in Fig. 3.7. The parameters used for the calculations correspond to the X-PEEM mode of the instrument, magnifying an image formed by the secondary electrons created in the x-ray absorption process (see Sect. 3.2.2), restricting the acceptance angle α by the typically used contrast

3 Experimental methods & setup

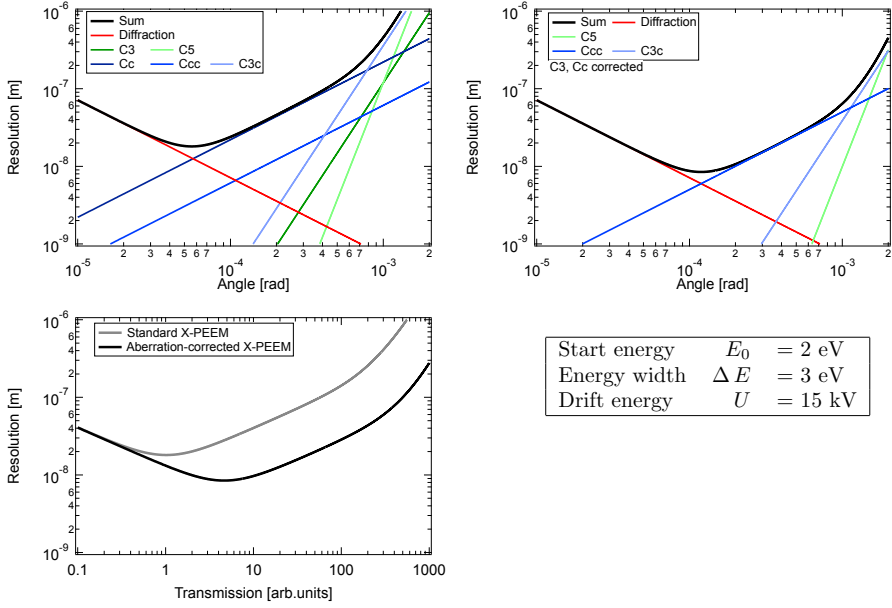


Figure 3.7 – Theoretical resolution limits as restricted by aberration given by Eqn.3.13. Computations have been made with values typical for the microscope used for this thesis in an X-PEEM setup: $E_0 = 2 \text{ eV}$, $\Delta E = 3 \text{ eV}$, and $U = 15 \text{ keV}$. Aberration coefficients for a microscope of the same build taken from [119]. The uncorrected microscope (a) shows a maximum resolution of about 18 nm. Aberration corrected microscope featuring $C_3, C_c = 0$ (b) resulting in a maximum resolution of 8.5 nm. (c) demonstrates the relation between microscope transmission and resolution. The corrected microscope transmits about 4.5 times more electrons than in an uncorrected state. Further explanations see text. Adapted from Ph.D. thesis NICKEL [108]

aperture of $20\text{ }\mu\text{m}$. Aberration coefficients have been taken from measurements on the same build of microscope by TROMP [119]. As can be seen, the dominating term in the resolution limit is the chromatic aberration, mainly limited by the energy width given by the distribution of secondary electrons (see Fig. 3.9). A 3 eV selection of this distribution is made by an energy filter ($20\text{ }\mu\text{m}$ slit width) located upstream of the contrast aperture. See Sect. 3.2.2 for further information. With a smaller energy width ($\sim 0.25\text{ eV}$) given by the electron beam in LEEM (Sect. 3.2.2), a much better resolution is achievable, making resolution limits mostly dominated by spherical aberration.

Aberration correction As shown in the previous paragraph, a correction of the leading aberration terms would be highly desirable to increase resolution limits or increase the transmission at the same resolution by using wider acceptance angles. Due to the limitation in electron-optical lens design, not allowing for achromatic lenses [143], approaches for aberration correction are limited [144]. Some experimentally proven approaches involve multipole-combination [145], Wien-filter [146], electrostatic meshes [147], moving-focus [148], time-modulated lenses [149], energy inversion [150], or electronic tetrode mirror [151]. The latter proves to be easier to realize to a technically sufficient elaboration and more practical in use than its competitors.

The electron mirror is formed by electrodes creating a rotationally symmetric electric potential $\Phi_{\text{mirror}} > eU_{\text{drift}}$ repelling approaching electrons. In contrast to electronic lenses, which show a shorter focal length for larger α (spherical undercorrection), the electronic mirror's spherical aberration coefficient is of opposite sign, creating longer focal length for larger α (spherical overcorrection). This effect can be understood, if one takes the magnitude and interaction length of the potential and electronic trajectory into account [108], and can immediately be seen in the sketch of Fig. 3.6 b).

In addition, an electron mirror also possesses a chromatic aberration coefficient of opposite sign compared to regular electronoptical lenses. Electrons of higher kinetic energy will reside longer in the electrostatic field of the mirror which results in a stronger focussing effect, hence a shorter focal length (overcorrected chromatic aberration). This effect is depicted in Fig. 3.6 d).

In order to compensate the aberrations of a cathode lens, the focal lengths, C_3^{TM} and C_c^{TM} of the electron mirror have to be controlled separately, motivating the design of a tetrode electron mirror in 1997 by PREIKSZAS and ROSE [152]. Featuring three degrees of freedom on the electric field, the tetrode mirror can be tuned to compensate C_3^{CL} and

3 Experimental methods & setup

C_c^{CL} of the cathode lens of a microscope by satisfying the following relations:

$$-C_3^{TM} = M^4 C_3^{CL} \quad (3.14)$$

$$-C_c^{TM} = M^2 C_c^{CL} \quad (3.15)$$

M is the magnification in the imaging plane of the mirror. For this corrected case, the effective aberration coefficients being zero, the curve expressing the radius of the circles of confusion for a focused image has been plotted in Fig. 3.7 b). Corrections of higher aberration terms, neglected in the previous discussion, have also been taken into account in calculation of this figure. The effect of aberration correction on PEEM can also be seen when comparing transmission and resolution, since an increased angle of emitted electrons can be used for imaging at a given resolution. Fig. 3.7 c) depicts this relationship and finds an increased transmission by a factor of 4.5 for the same transmission in aberration-corrected mode. As part of the experimental work during the setup of the LEEM/PEEM at UE56/1-SGM in this thesis (see Sect. 3.2.4) the aberration correction coefficients were determined, taking values from TROMP [119] as a starting point, contributing to [153].

3.2.2 Imaging modes

The imaging modes used with the FZ-Jülich LEEM/PEEM will be discussed shortly in this chapter. All three modes presented use a similar optical setup for imaging, however, the contrast mechanisms and information generated are of different origin.

Threshold PEEM Threshold PEEM describes the imaging of photoelectrons that carry just enough energy to leave the crystal. The photon energy for that purpose has to overcome the work function Φ of about 2-5 eV [156], depending on the sample. A typical source with a photon energy in this range is a mercury-discharge lamp, a broad band lamp featuring a prominent spectral line of $h\nu = 4.9$ eV photonic energy. Because of this low-energy excitation, the energy width of the photoelectrons released from the sample is of the order of 1 eV, as sketched in Fig. 3.9 a). The small energy width results in low chromatic aberration and a strong intensity dependence on the work function Φ . Local variation of the work function or structural changes on the sample, characteristic for chemical or structural changes, leads to image contrast. However, also topographical features, which influence the electron trajectories by locally distorting the electric field formed with the objective lens, create image contrast. Fig. 3.8 a) shows topographical

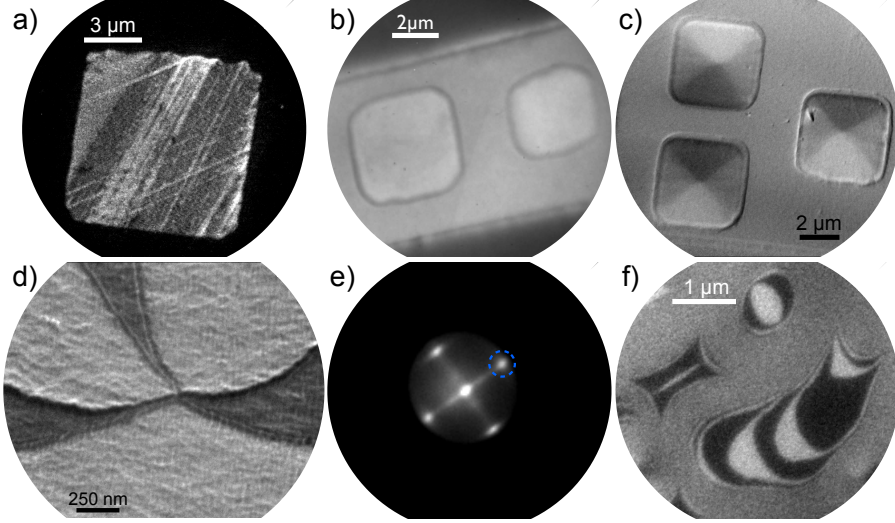


Figure 3.8 – Imaging modes of LEEM/PEEM: Threshold PEEM from Permalloy structures on a Au stripline (a), XPEEM (b) and XMCD-PEEM (c) from similar samples at the Fe L_3 edge. (a)-(c) have been recorded in connection to Refs. [116] and [108]. MEM-LEEM from an ErMnO_3 crystal recorded in connection with Refs. [154] and [155](c). LEED pattern recorded in diffraction mode from Si(001) (d) and the corresponding darkfield-LEEM image (e).

contrast on a lithographically structured $10\ \mu\text{m}$ Permalloy² square on the edges. Chemical contrast can be seen as the Permalloy square has a different work function than the substrate material (Si). Also a mixture of topographical and work function contrast is the reason for different brightness levels on the square, due to photoresist, which was not entirely removed. The respective sample has been created and measured in the context of Refs. [108] and [116].

XPEEM of secondary electrons with x-rays of tunable energy and polarization is the primary operation mode used for this thesis. Here, the sample is illuminated with x-rays, creating photoelectrons from core levels according to the selection rules (see Sect. 2.4). Excited electrons and AUGER electrons emitted in the process of the core-hole decay (see Sect. 3.1.2), create a secondary electron cascade by scattering in the sample. As the eIMFP increases towards lower electron energies, the secondary electron

²Permalloy is an alloy of about 80% Nickel and 20% Iron, which is known for its high magnetic permeability.

3 Experimental methods & setup

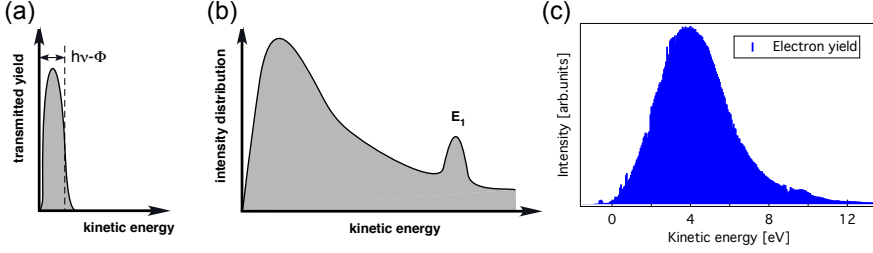


Figure 3.9 – Sketched photoelectron distributions in the low kinetic energy range, excited by a Hg-discharge lamp (a), and x-ray source (b). Both from [156]. Secondary electron spectrum from a BTO single crystal excited by synchrotron light, measured in the PEEM at UE56/1-SGM (c). The broad flank at the low energy side is given by the decreasing scattering probability of low energy electrons due to the bandgap of the BTO in combination with the energy resolution of the used imaging mode (approx. 1eV).

spectrum peaks at about 5-7 eV [157]. Fig. 3.9 b) shows an image of the distribution of secondary electrons by excitation with synchrotron light in a typical energy-resolved PEEM experiment. The secondary electron spectrum in Fig. 3.9 c) shows the secondary electron peak from a BTO single crystal illuminated with x-rays at the PEEM used in this thesis.

Evidently, the secondary electron intensity is proportional to the x-ray absorption. This enables us to use all effects found in absorption spectroscopy as contrast mechanisms, like element selectivity and XMCD.

Tuning the photon energy to an absorption peak of a selected element, e.g. of an alloy, enables one to laterally resolve the abundance of this element. By additionally using light of circular polarization parallel to the magnetization, the electronic transitions become dichroic, hence the magnetic information of the material is transported to the image. The magnetic information in an image, formed from electrons from such a dichroic transition, can be extracted by calculating the normalized difference of two images recorded at opposite circular polarization of the incident light. The so-called asymmetry image is given as

$$\mathbf{A} = \frac{\mathbf{I}_{\sigma^+} - \mathbf{I}_{\sigma^-}}{\mathbf{I}_{\sigma^+} + \mathbf{I}_{\sigma^-}} \quad (3.16)$$

with \mathbf{I}_{σ^\pm} being the 2D intensity distribution for light of circular polarization σ^\pm . As previously described, the magnetic signal is proportional to the projection of the mag-

netization vector \mathbf{M} onto the propagation vector \mathbf{k} of the incident light:

$$A \propto \mathbf{M} \cdot \mathbf{k} \quad (3.17)$$

For photons incident on the sample with about 25° , both in- and out-of-plane magnetization directions can project non-vanishing contributions to the \mathbf{k} -direction. While out-of-plane magnetization direction with respect to the photon \mathbf{k} is fixed since it is coupled to the optical axis by zero condition for the sample tilt in a photoemission microscope, in-plane magnetization can be subject to azimuthal rotation and therefore a varying projection. The method of sample rotation can be exploited to distinguish between in-plane magnetized- and out-of-plane magnetized areas.

We want to point out, that the synchrotron radiation of variable energy allows for microspectroscopy in absorption geometry.

Fig. 3.8 b) & c) show XPEEM images of a Permalloy-structure as imaged from secondary electrons at the Fe edge and as XMCD asymmetry image, respectively. Chemical selectivity and topographical influence is demonstrated in b). The magnetic information can be seen in c). The Permalloy structures create a flux closure LANDAU-pattern originating from shape anisotropy [158]. Neutral gray levels show no feasible projection of the magnetization vector onto the wave vector \mathbf{k} of incident photons. White and black regions are a result of parallel (antiparallel) alignment of magnetization vector and the \mathbf{k} of incident photons.

Low energy electron microscopy (LEEM) is a technique, where a collimated and monochromated electron beam is focused on the sample to probe the density of states above the Fermi energy. The electrons are accelerated to the sample potential of 15 kV and are decelerated upon approaching the sample. The elastically backscattered electrons are then re-accelerated towards the cathode lens, similar to low energy electrons leaving the sample in threshold PEEM. A magnetic beam deflector is needed to separate the two passes through the objective lens.

As the potential difference between the sample and the incident electrons can be tuned, different imaging modes are possible with LEEM:

(i) Mirror electron mode LEEM (MEM-LEEM), corresponding to a sample potential larger than the electron kinetic energy. Electrons approaching the sample will be decelerated and repelled before reaching the sample surface. At that point, the low energy electrons are very susceptible to variations of the electric field, distorted by topographic features on the sample surface and local changes in the sample potential by work func-

3 Experimental methods & setup

tion or ferroelectric differences. Fig. 3.8 d) shows an image of ferroelectric ErMnO_3 measured at the FZJ LEEM/PEEM in the frame of [154, 155]. Bright and dark areas are created by the ferroelectric potential differences in the corresponding domains. Charging/conductivity effects reveal ferroelectric domain walls.

(ii) Upon decrease of sample potential the electrons will be able to scatter and diffract at the sample surface. The diffraction patterns can be imaged by setting the lenses to a mode projecting the diffraction plane onto the image detector. Hence, local LEED patterns can be gathered comparable to the description in Sect. 3.1.3. The LEED pattern shown in Fig. 3.8 e) originates from a clean (2×1) reconstructed $\text{Si}(001)$ substrate at about 3 eV. The existence of four first order LEED spots is reasoned by the rotated equivalent reconstruction of (1×2) areas, which are equally distributed on the surface.

(iii) If the diffracted electrons are selected by isolating a single LEED spot, brightfield-LEEM [(0,0)-spot] or darkfield-LEEM (every other LEED spot) are possible. The selection is made by an aperture in the diffraction-plane of the microscope, while the incident electron beam is tilted to bring desired LEED-spots onto the optical axis and through the aperture. This method allows one to conveniently switch between imaging modes. Due to the diffraction process, only the parts of a sample that contribute diffracted electrons to the chosen LEED spot will be bright in the real-space image. This can be seen in Fig. 3.8 f), where the electrons from the selected LEED-spot in panel (e) are creating a black/white pattern with respect to the (2×1) surface reconstruction of a $\text{Si}(001)$ crystal. Each of the two orientation directions of the reconstruction only contributes to two of the four first order LEED spots, hence selecting one LEED spot only allows electrons of one of the two rotated domains to contribute to the image.

3.2.3 Generation of polarized x-rays

This section will give a brief overview on synchrotron light creation, especially circularly polarized x-rays, and the particular characteristics at the FZ Jülich beamline UE56/1-SGM at BESSY II, Berlin, Germany.

Synchrotron radiation was discovered as side effect in early synchrotrons (initially built for high energy particle acceleration), because it meant a loss in kinetic energy of the circulating particle [159]. The by-product synchrotron radiation was used in 1970's synchrotrons yielding highly successful experiments, which led to the construction of storage rings solely dedicated as light sources all over the world. However, the fundamental processes are still the same, and can be found in relativistic electrodynamics [160]. As is

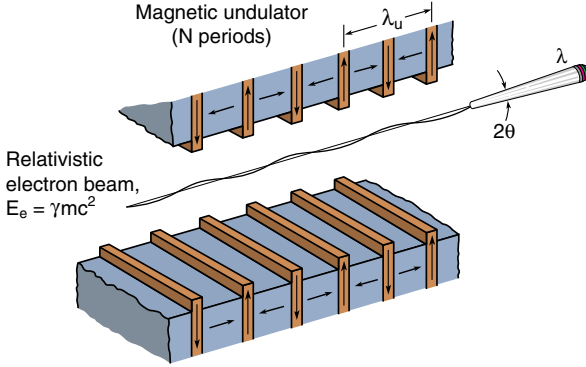


Figure 3.10 – Schematic layout of an undulator. From [161]

known from the MAXWELL equations, electromagnetic radiation is emitted from accelerated charged particles, e.g. electrons. The relativistic LORENTZ-transformation shows that the radiation is focused into a cone along the particle's trajectory for particles moving nearly at the speed of light, which is called 'searchlight effect'. The power P emitted by the electron is strongly dependent on its energy E , which can be expressed as follows for highly relativistic electrons ($\beta = v/c \approx 1$) on a circular trajectory:

$$P = \frac{2e^2c}{3R^2} \left(\frac{E}{m_0c^2} \right)^4 \quad (3.18)$$

e denotes the electron charge, c the speed of light, R the radius of the circular motion and m_0 the electron's rest mass. The direction of radiation emission transforms from a typical dipolar characteristic for $\beta \ll 1$ to a narrow cone around the motion direction for highly relativistic electrons ($\beta \approx 1$). The radiation is emitted in an opening angle of $\Theta = \frac{1}{2\gamma}$, $\gamma = \sqrt{1/(1-v^2/c^2)}$. These two effects result in a high brilliance of synchrotron radiation, emitted at angles as small as $\Theta = 0.1 \text{ mrad}$ ($< 0.01^\circ$).

A breakthrough for dedicated light sources was the development of insertion devices [162]. They consist of a periodical array of magnet pairs with alternating field direction, forcing electrons onto an oscillating trajectory (see Fig. 3.10). On this trajectory the electrons are constantly accelerated and de-accelerated in a periodic pattern. In the so called undulator, the constructive and destructive interference of the henceforth emitted radiation creates monochromatic radiation, characteristically peaked around a single wavelength and its higher harmonics (as these are also created in the interference pattern)

3 Experimental methods & setup

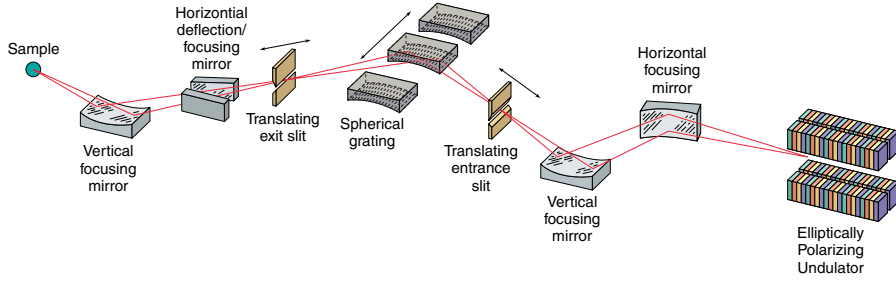


Figure 3.11 – Schematic layout of a beamline. From [161]

$$n\lambda = \frac{\lambda_u}{2\gamma^2} \cdot \left(1 + \frac{1}{2}K^2 + \gamma^2\Theta_u^2\right), n = 1, 2, 3, \dots \quad (3.19)$$

for relativistic electrons. Here, λ_u is the period length of the magnet pairs, and Θ_u the observation angle with respect to the undulator axis. Because

$$K = 0.934\lambda_u [\text{cm}] \cdot B [\text{T}] \quad (3.20)$$

the energy, hence wavelength, of the generated undulator radiation can be varied by modifying the magnetic field. This is typically realized by changing the gap between the two opposing arrays of magnets. The polarization of synchrotron radiation produced by this type of undulator is linear horizontal, meaning the vector describing the electrical field oscillation lies in the plane of the storage ring. By changing the geometry of the magnet-arrays, the polarization can be manipulated, opening up a whole new body of measurement techniques depending on the polarization of the photons, e.g. on magnetic materials by the XMCD effect described in Sect. 2.4. Splitting up both magnetic arrays in two separate lines and shifting them with respect to each other, as proposed by SASAKI et al. [163], creates a rotation in the magnetic field. The angular momentum, introduced to the electrons by forcing them onto a screw-like trajectory, has to be conserved, resulting in a rotation of the electric field vector of the synchrotron light. Hence, the photons are elliptically or circularly polarized, depending on the phase shift.

Beamlines In order to guide the synchrotron radiation onto a sample in an experiment, a setup of guiding mirrors is needed, as displayed in Fig. 3.11. Typically, modifications of the radiation's properties conforming to the needs of a particular experiment are

applied throughout the beamline by additional optical elements. This usually involves monochromatization and focussing of the light. The selection of a single photon energy in the soft x-ray regime is realized by diffracting the incoming (white) beam on an optical grating utilizing Bragg's law [164]:

$$n\lambda = d(\cos \alpha - \cos \beta), \quad (3.21)$$

where d is the line spacing of the grating and α and β are the entrance and exit angles, respectively. The selection is made by tilting the grating to a desired combination of these angles. Different setups use either a spherical grating to focus the entrance slit onto the exit slit or a plane grating with an additional focusing mirror. The exit slit cuts a certain energy interval ΔE from the angularly dispersed energy distribution [161]. The final part of a beamline usually features refocussing mirrors to create a desired spot-size on the sample and a gold-grid to measure a photocurrent proportional to the photon flux of the beamline. This typically is used as a normalizing means to correct measurement data for flux variations.

3.2.4 FE-LEEM-P90 at UE56/1-SGM

The microscope used in this thesis is a combined LEEM/PEEM microscope with a design developed by TROMP [114]. A detailed description of the electron optics and a setup procedure can be found in Refs. [115, 119]. A schematic overview of the microscope can be found in Fig. 3.12 and shall be topic of further discussion. In addition to the general features of immersion lens electron microscopy as described in Sect. 3.2.1, the microscope features two 90° magnetic beam separators realized by prism arrays. The first prism MP1 separates the incoming electron beam, used in LEEM mode, and the imaged electrons from the sample. The second prism MP2 separates the electrons entering the aberration corrector from the reflected electrons. Since each prism can be passed twice, the respective quadrants of the prism are further on named MP1.1 & MP1.2 and MP2.1 & MP2.2. The prisms possess the characteristics of a spherical lens and are, in the context of the discussed microscope, operating as 1:1 transfer lenses [165]. Most notably, they are free from astigmatism. Each 90° deflection of the prisms transfers a diffraction plane from entrance to exit-plane with real-space images in the diagonal of the respective prism. The objective lens O1, as part of the cathode lens, creates a diffraction image of the emitted electrons in the entrance plane of MP1.2. In this plane, electrons of a specific energy can be selected by an energy slit. The first real space image, at the mentioned image plane in the diagonal of MP1.2, possesses a magnification of $M=38$. The transfer lens

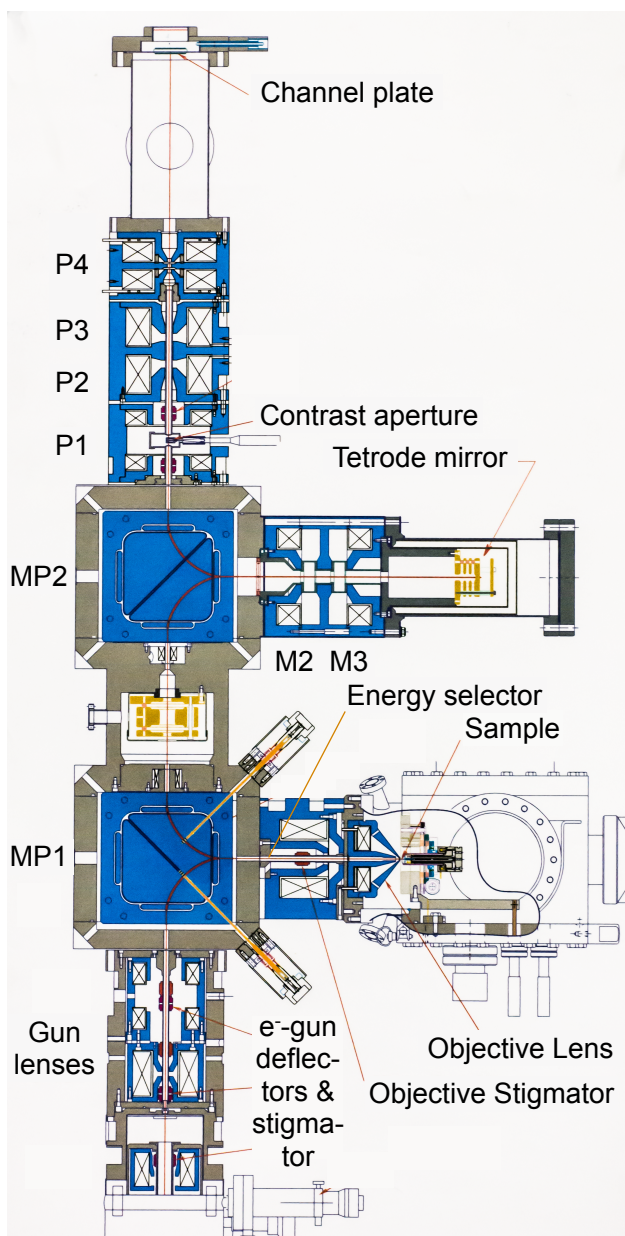


Figure 3.12 – Sketch of the aberration corrected PEEM/LEEM microscope. Annotations corresponding to text.

between the prisms solely serves the purpose of transferring this image to the diagonal of MP2.1, resulting in a 180° transfer by the two prisms combined. By M2, the image is demagnified by a factor of ~ 4 with a resulting magnification $M=8.5$, which is necessary to conform the diffraction plane to the acceptance angle of the aberration corrector TM. M3 executes the necessary transfer. After being mirrored at TM, the aberrations of the cathode lens have been corrected and the described effects of M3 and M2 are passed in reverse order, also magnifying the image back to $M=38$ to the image plane of MP2.2. The first lens of the projection column P1 is located in the exit plane of MP2.2, containing a diffraction image and also the optional contrast apertures. The projection column, consisting of lenses P1-4 displays the aberration corrected image with a variable final magnification to a commercial multi-channel plate with an attached phosphor screen. A slow-scan CCD camera is utilized for the digitalization of the image. In addition, the projector can be switched between real-space and diffraction-plane imaging with P2 being on or off. In the context of this thesis, considerable work has been put to the improvement of the working condition of the microscope, involving alignment of the image planes, aperture placement and aberration correction establishment.

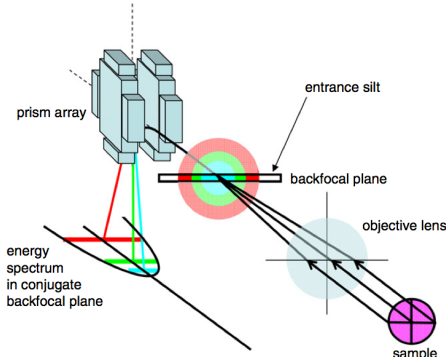


Figure 3.13 – A schematic view of the energy filter. In the entrance plane of P1.2, a dispersion plane is utilized to select an energy slice from the imaging electrons. The energy dispersion of the electrons leads to a parabolic distribution in the back-focal plane of P1.2. Further explanations see text. From [115]

Energy filter Imaging modes as XPEEM call for an energy filter to reduce the energy width and improve the spatial resolution. An extensive description of the energy filter used in this microscope can be found by TROMP et al. [115]. The construction is realized by the dispersion characteristics of the prism array and a k_y -selecting slit in the dispersive (k_x, k_y) entrance plane of P1.2. After passing the prism, the slice selected from the k_y axis disperses linearly proportional to its energy ($\Delta x/\Delta E = 6 \mu\text{m}/\text{eV}$ for a drift energy of 15 keV), reducing the $k_y + E$ axis into an energy axis. The dispersion relation for free electrons leads to a parabolic shape of the k_x, E distribution.

3 Experimental methods & setup

Additional details The microscope features three illumination sources, a mercury vapor lamp of 4.9 eV photon energy, a cold cathode electron gun with an energy width of about 0.25 eV, and the beamline UE56/1-SGM at BESSY II, Berlin, providing monochromatic x-ray light with variable energies of 100-1200 eV for linear and circular polarizations. The x-ray spot size focused onto the sample surface by the refocusing optics is about $70\text{ }\mu\text{m} \times 40\text{ }\mu\text{m}$. Energy resolution is between 200 and 700 meV for typically used slit-widths. To reduce vibrations coupling into the microscope, it is mounted onto a granite pedestal followed by a set of active vibration reduction devices from the 'Table Stable' range of JRS Scientific. The limiting factor hence is vibration introduction via UHV tubing to the beamline, the preparation chamber, through cables, and acoustic coupling from the environment.

During the time of the measurements at the microscope, it featured a manipulator with five degrees of freedom and incorporated electron-beam heating. By the time of this thesis' writing, an improved manipulator design is in operation, featuring an additional azimuthal rotation and the option of sample cooling down to $\sim 150\text{K}$. The rotation allows for convenient magnetic in-plane contrast optimization and makes accurate separation of contrast from in-plane and out-of-plane magnetization possible. All rotation studies in this thesis still involved extraction of the sample and rotation of the sample holder with respect to the manipulator.

An extensive setup for dynamic magnetization measurements has been developed in the framework of a Ph.D. thesis by F. NICKEL [108]. Pump-probe measurements can be carried out in a stroboscopic arrangement, exciting with a magnetic field up to 10 mT within 1 ns. A compact system, triggered and synchronized to the probing synchrotron pulses by a laser diode, has been incorporated in the sample holder. A custom electrostatic deflection electrode mounted in the image plane of MP2.2 enables dynamic measurements regardless of the synchrotron filling-pattern by specific selection.

In-situ demagnetizing In order to generate a demagnetized multidomain state in the sample, in-vacuum coils have been constructed for the experiments in this study for demagnetization purposes. Two core-less coils can be brought to the sample, creating a homogeneous magnetic field in the plane of the sample. The coils are powered by an alternating current of 50 Hz, which can be regulated in intensity. The magnetic field created in this setup reaches a maximum of about 100 mT, sufficient to overcome the coercive field of the investigated Ni/Cu(001) and $\text{Ni}_x\text{Pd}_{1-x}/\text{Cu}(001)$ films. In a typical demagnetizing procedure, the field is ramped up and down by hand twice. When ramped up, the amplitude of the current and hence the amplitude of the alternating magnetic

field is brought to zero in about 15 s, allowing for about 75 switches of field polarity per 10 mT.

3.2.5 Determination of image rotations.

Even though most magnetic lenses in this microscope are designed as rotation free doublets, the singlets result in a rotation of the image depending on the magnification settings and whether the operation mode is set to diffraction- or real-space imaging. A determination of the rotational character for the used magnifications and the diffraction plane has been conducted in the course of this study. These interrelations are needed to connect crystallographic directions detected by LEED to real-space images for the utilized fields of view (FOVs). The measurement was realized by corresponding motions of tilt (in diffraction plane) and x-y-translation (in real-space) due to a parallel alignment of the respective motors. The resulting values can be found in table 3.1.

FOV	diffraction	43 μm	20 μm	10 μm
Rotation (all CCW)	0°	(60 \pm 5)°	(78 \pm 8)°	(80 \pm 2.5)°

Table 3.1 – Rotation of selected fields of view with respect to the diffraction imaging condition. These values are necessary to identify crystallographic axes determined by LEED images in real-space images.

3 *Experimental methods & setup*

4 Sample preparation & characterization

Samples used in this study were prepared in-situ in the preparation chamber connected to the PEEM/LEEM endstation at UE56/1-SGM, BESSY II, Berlin, Germany. All methods used to characterize the samples are described in chapter 3, and a schematic display of the arrangement in the preparation chamber can be found in Fig.3.2. The base pressure was about $7 \cdot 10^{-11}$ mbar.

4.1 Cu(001) substrate preparation

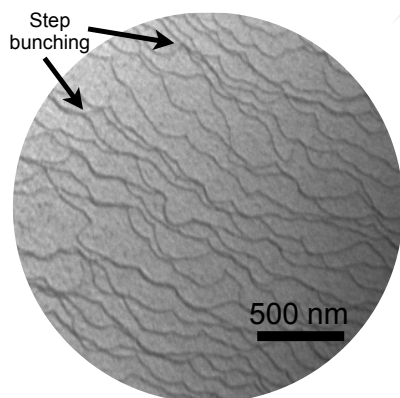


Figure 4.1 – LEEM image from the Cu part of a wedged NiPd/Cu(001) sample. Contrast lines arise from atomic steps. Only a few bunched steps can be seen scattered over the field of view.

A preparation of well-ordered, epitaxially grown films asks for a clean and smooth surface of the substrate crystal and shall be described in the following. The Cu(001) single crystals used for this study were provided by Mateck GmbH [166] with a maximum mis-cut of $< 0.1^\circ$ and a surface roughness of < 30 nm. The substrate crystals were cut in a hat shape, to minimize the formation of stress-induced defects and grain-boundaries in the studied surface area. This is important since the crystal has to undergo many cycles of annealing and sputtering to yield a carbon-free, oxygen-free and smooth surface. Due to the increased mobility of atoms, these cycles promote defects, if the crystal is deformed by force applied by the sample holder.

The hat-shape also allows for shallow angles of incidence during MEED (Sect.3.1.4) growth rate measurements in the geometry of our sample holder system.

Ar⁺-ion bombardment sputtering was applied to remove carbon and oxygen contamina-

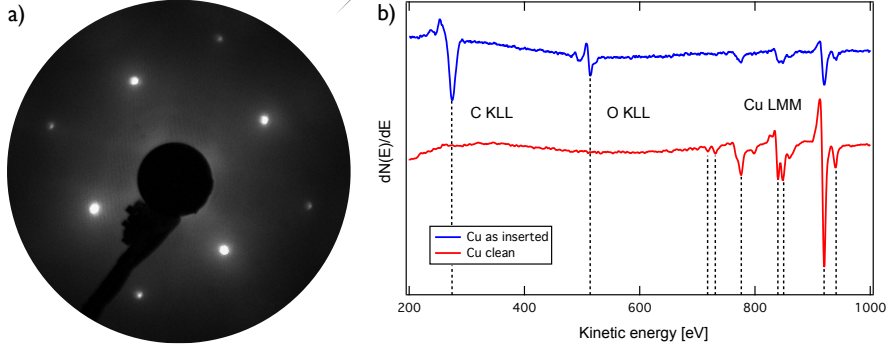


Figure 4.2 – Clean Cu LEED pattern at 150 eV (a). Sharpness of the spots limited by ErLEED optics. Comparison of AUGER spectra (b), demonstrating efficient cleaning by sputtering and heating cycles as described in text.

tions from the crystal surface. Since sputtering leaves the surface in a rough state which is not suitable for epitaxial growth, annealing cycles were applied in an alternating fashion. The elevated temperatures increase the mobility of the surface atoms to promote rearrangement to reduce roughness by minimizing surface free energy. However, annealing also increases the mobility of contaminations, resulting in their segregation to the top. A contamination depletion layer is formed by repeated cycles of sputtering and annealing. Sputtering was done with an acceleration voltage of $U = 1500$ V, at a sputtering current of about $2 \mu\text{A}/\text{cm}^2$, for about 30 mins. The sample was carefully brought to the annealing temperature of about 600°C with about $20^\circ\text{C}/\text{min}$ for an annealing period of about 20 mins at the plateau temperature. The final cycle of sputtering and annealing was carried out at 800 V acceleration voltage and about $1 \mu\text{A}/\text{cm}^2$ for about 10 minutes. The final annealing cycle was carried out for about 30 minutes, with a careful cooldown procedure of about 1.5 hours duration.

AUGER spectra of the clean copper crystal show no signs of contaminations, C and O peaks are below detection limit of the AUGER system (about 1% of a ML). A comparison of the copper crystal as introduced to vacuum and after the cleaning procedure can be found in Fig. 4.2 b). The LEED patterns show sharp spots with a low diffuse background as can be seen in Fig. 4.2 a), which proves a high long-range order quality of the sample, as well as a low sample roughness. AFM measurements for a 2 cycle prepared Cu crystal show a root mean square (RMS) roughness of 0.5 nm for an autocorrelation length of $5 \mu\text{m}$ square. On a shorter length scale, of about $1 \mu\text{m}$ square, the RMS roughness is about 0.1 nm. We assume, this surface quality is achieved for the whole sample upon a

full preparation cycle. Atomic step distance has been shown to be in the range of 10 nm and up to several times $1/10\mu\text{m}$ in previous studies [167], depending on annealing temperature. Lower annealing temperatures suppress step bunching and hence create smaller terrace sizes [168]. A compromise between step bunching and step size has to be found. In the frame of this study, LEEM measurements on the Cu-part of a wedged NiPd/Cu sample show step contrast as seen in Fig. 4.1. Atomic step distance is between 60 nm and 100 nm on average after a typical substrate preparation procedure, without prominent step bunching, which is an excellent result of preparation.

4.2 Ni/Cu(001) thin films

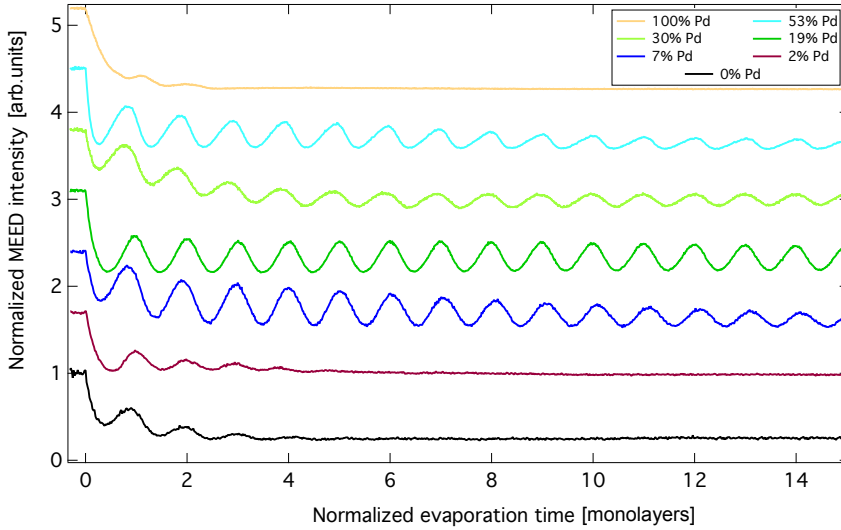


Figure 4.3 – A comparison of MEED intensities recorded from the (0,0) spot during evaporation of NiPd films with different compositions. The evaporation time has been normalized to evaporated monolayers, intensities are normalized to the respective intensity prior to evaporation and the curves have each been offset separately.

All films produced for this thesis have been grown at room temperature to prevent intermixing of the Ni- or NiPd-films with the Cu substrate. During growth, the vacuum did not rise above 5×10^{-10} mbar. General information about molecular beam epitaxy and growth processes is given in Sect. 3.1.1. MEED (see Sect. 3.1.4) was employed to measure the sample thickness during the growth process. LEED images confirm that the

4 Sample preparation & characterization

deposited Ni films grow in an fcc crystal lattice. The lattice mismatch between Ni ($a_{\text{Ni}} = 3.52\text{\AA}$ [169]) and Cu ($a_{\text{Cu}} = 3.61\text{\AA}$ [169]) of 2.6% falls into the category of STRANSKI-KASTRANOV growth, which results in a suppression of MEED oscillations after about 4 ML [see the MEED comparison Fig. 4.3 curve for Ni/Cu(001)]. STM images from Shen et al. [99] confirm layer-by-layer growth for the first 3.4 ML, which marks the start of a transition to island growth, agreeing with the MEED behavior as displayed. At 7.1 ML the film structure can be regarded as three-dimensional platelike islands of rectangular shape [99], with their boundaries aligned to crystallographic $\langle 110 \rangle$ axes. 16.9 ML and 20.3 ML films showed island heights of about 1 nm for both films. LEED images from our study for films between 15 ML and 60 ML suggest that film roughness does not increase beyond a certain equilibrium condition, which we identify as the reported island height of about 1 nm. The deposited Ni/Cu(001) and NiPd/Cu(001) films were not post-annealed to avoid intermixing between substrate and film, which leaves the samples with the described roughness. This is reflected in LEED measurements, featuring a broadened spot size and increased diffuse background intensity, compared to the Cu(001) crystal. MATTHEWS et al. have conducted transmission electron microscopy (TEM) measurements on the lattice strain and its reduction mechanisms depending on film thickness in Ni/Cu(001) [170]. In the framework of the previously described model by CHAPPERT and BRUNO in Sect. 3.1.1, Eqns. 3.4 & 3.5, a critical thickness h_c of $(14.6 \pm 3)\text{\AA} \hat{=} 8.3\text{ ML}$ was found. The TEM images revealed a network of misfit dislocations, oriented along the $\langle 110 \rangle$ -axes as the mechanism to reduce the film stress. BOCHI et al. [91] fitted a power law equation to their own data on lateral stress in Ni/Cu(001) from optical interferometry, confirming the findings from MATTHEWS. A power law conforming to the BRUNO-CHAPPERT model and thereby to the findings described, can be found in Fig. 3.3.

AUGER spectra after evaporation show no signal of C and O contaminations in the deposited Ni films within the detection limit of the Auger system, as can be seen in Fig. 4.4.

4.3 Ni_xPd_{1-x}/Cu(001) thin films

4.3.1 Preparation and characterization

The MBE process for alloy deposition is the same as for Ni/Cu(001) films regarding substrate preparation procedure, evaporation conditions and handling. Again, the resulting AUGER spectra show no hints of C and O contaminations, which can be seen

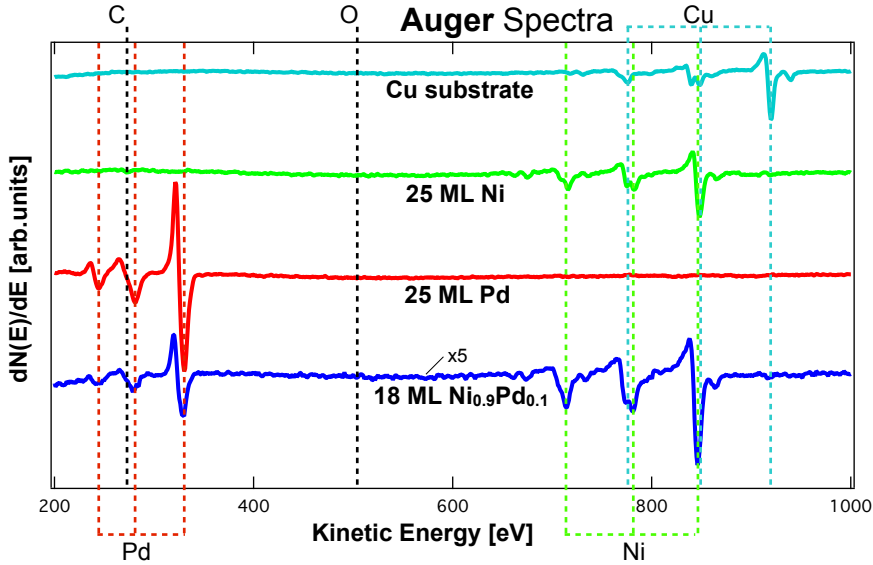


Figure 4.4 – A comparison of representative AUGER spectra. Cu(001) after cleaning procedure (cyan), 25 ML Ni/Cu(001) (green), 25 ML Pd/Cu(001) (red), 18 ML $\text{Ni}_{0.9}\text{Pd}_{0.1}$ /Cu(001) (blue). Superposition of the AUGER reference spectra in the alloy spectrum is clearly visible, enabling a composition analysis according to Eqn. 3.9.

exemplarily in Fig. 4.4 for a $\text{Ni}_{90}\text{Pd}_{10}$. The detection of both Pd and Ni AUGER signals can be seen, which, with the help of the displayed reference spectra, can be translated to film composition data by Eqn. 3.9.

An important difference lies in the growth mode of the evaporated films depending on the composition, which will be discussed in the following paragraph.

4.3.2 Effects on lattice strain

The binary alloy of $\text{Ni}_x\text{Pd}_{1-x}$ condenses in the same fcc crystal structure as Ni and is miscible throughout the whole composition range. For thin films no pronounced segregational behavior has been reported, however, for bulk $\text{Ni}_{50}\text{Pd}_{50}$ segregation could be found [171]. SEIDER has found that two separated layers of Pd (2 ML) and Ni (3 ML) interdiffuse without further improvement upon postannealing up to 450 K [66]. On the one hand, this underlines the ambition of Pd to alloy with Ni as stated by the author of the reference, on the other hand this could also mean that Pd acts as a surfactant layer

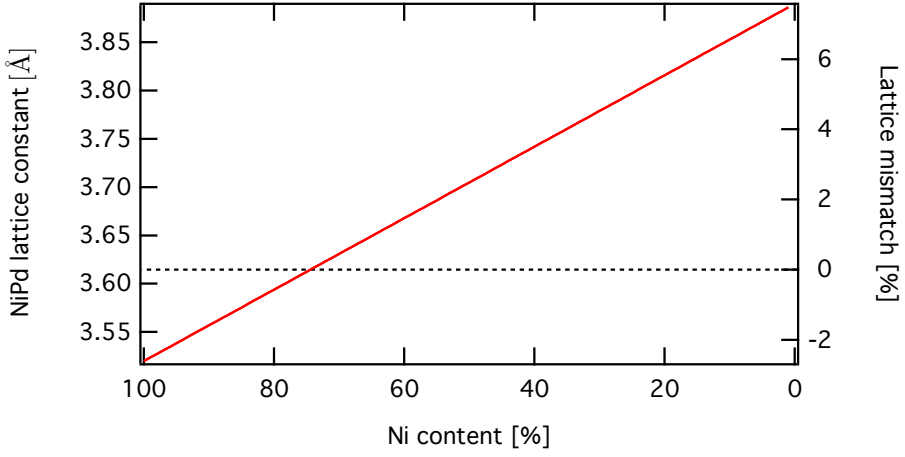


Figure 4.5 – Lattice constant for $\text{Ni}_x\text{Pd}_{1-x}$ depending on the alloy composition. The dashed line denotes the lattice constant of Cu(001). The lattice mismatch with the Cu(001) substrate is given on the right axis. The intersection between the alloy curve (red) and the dashed line denotes the composition of vanishing lattice mismatch.

during growth of the Ni film.

With the fcc lattice sites being occupied randomly by Ni or Pd atoms for alloyed films, the lattice constant of the resulting film is assumed to be a linear combination between the two bulk constants of the mixed elements as given by VEGARD's law [172] and the composition x :

$$a_{\text{Ni}_x\text{Pd}_{1-x}} = x \cdot a_{\text{Ni}} + (1 - x) \cdot a_{\text{Pd}}; \quad (4.1)$$

$a_{\text{Ni}} = 3.52 \text{ Å}$ [169] and $a_{\text{Pd}} = 3.88 \text{ Å}$ [169] being the bulk lattice constants for Ni and Pd, respectively. If put into relation to the Cu(001) substrate lattice constant as given in relation 3.1, the lattice mismatch can be plotted as a function of the NiPd composition (see Fig. 4.5).

As a result of the lattice constant change of the film and therefore varying mismatch, deposited NiPd turns from an expanded to a compressed film upon Pd ratio increase, with a vanishing lattice mismatch at 25 % Pd content. In this 'perfect' configuration the film doesn't need to reduce film stress by incorporating misfit dislocations, which constitutes a FRANK-VAN DER MERVE film growth. The process from STRANSKI-KASTRANOV-growth towards layer-by-layer growth for indefinite sample thicknesses is a continuous

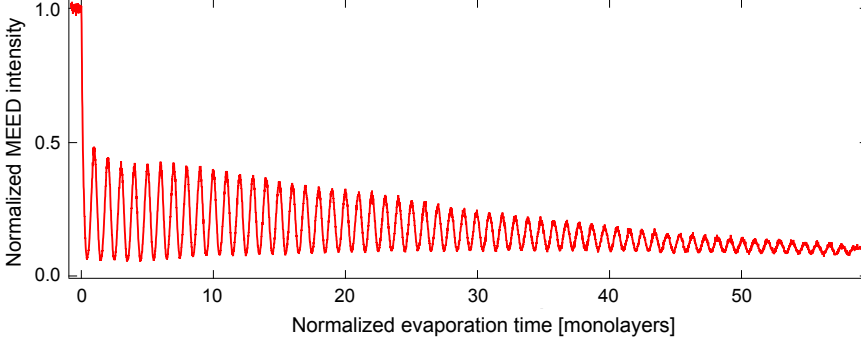


Figure 4.6 – MEED oscillations from a $\text{Ni}_{70}\text{Pd}_{30}$ film. Due to the small lattice mismatch, layer-by-layer-growth is preserved for higher film thicknesses. The evaporation process was stopped at 60 ML.

one, also reflected by the persistence of MEED oscillations when the composition gets closer to 25 % Pd content. Close to the composition of vanishing lattice mismatch we observed MEED oscillations up to 60 MLs, which were the thickest films grown in this stoichiometry regime. The MEED oscillations for such a 60 ML $\text{Ni}_{70}\text{Pd}_{30}$ film can be seen in Fig. 4.6. The continuous transition of growth modes is given by the nature of the relaxation mechanism. As stated above, MDs are incorporated at a certain threshold thickness. The CHAPPERT-BRUNO model implies that two films with two different lattice mismatches regarding their substrate, have the same amount of remaining stress at all thicknesses above the larger h_c , if the means of strain relaxation are assumed to be the same in both cases (see Fig. 3.3). The STM measurements of SEIDER show no hint for a significant difference between NiPd alloy growth and pure Ni films [66].

4 Sample preparation & characterization

5 Magnetic properties of Ni/Cu(001) and $\text{Ni}_x\text{Pd}_{1-x}/\text{Cu}(001)$

In this chapter the experimental results on the epitaxially grown Ni/Cu(001) and NiPd/Cu(001) films in wedged and continuous film geometry are presented. XPEEM measurements have been conducted at the synchrotron source BESSY II, Germany, Berlin at the Forschungszentrum Jülich beamline UE56/1-SGM providing soft x-ray photons of variable polarization. The experimental chamber resides at a base pressure of 3×10^{-10} mbar, while the in-situ grown films were freshly prepared typically on a daily basis with a total time of 36 hour examinations on some few films.

The experiments presented in this chapter aim for an understanding of the evolution of magnetic anisotropy in Ni/Cu(001) and $\text{Ni}_x\text{Pd}_{1-x}/\text{Cu}(001)$ films under varied composition with respect to the domain formation.

As a model system with an extensive scientific database, the microscopic magnetic properties of Ni/Cu(001) in a demagnetized state are investigated and compared to existing publications in experiment and simulation.

Ni-like $\text{Ni}_x\text{Pd}_{1-x}/\text{Cu}(001)$ films are discussed in a comparative manner in the following section, including the topographical influence on the domain structure. In particular, a discussion of the domain wall influence on the observed domain pattern can be found in this section.

In the third part of this chapter, the model of anisotropy contributions is put into context of $\text{Ni}_x\text{Pd}_{1-x}/\text{Cu}(001)$ films that exhibit compressive rather than tensile strain.

Finally, the chapter is concluded with an investigation of the SRT with respect to the frequently reported drop of T_c at the SRT.

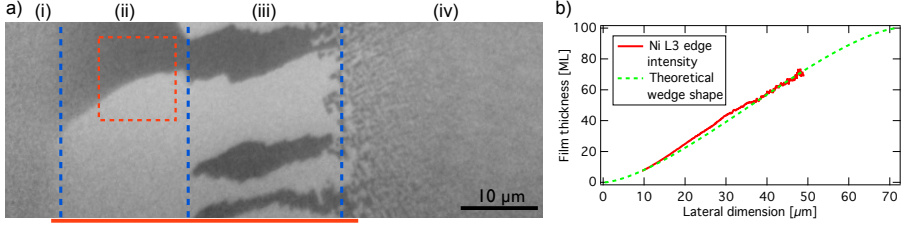


Figure 5.1 – Survey XMCD image of a Ni/Cu(001) wedge at the Ni L_3 edge (852.6 eV) from ~ 5 - ~ 95 ML (a). The red rectangle marks the area used to extract the information used for the histogram shown in Fig. 5.2. The red bar underneath the image denotes the corresponding image area for which the intensity information in (b) has been extracted. Ni wedge thickness from measured Ni L_3 intensity and the theoretical thickness distribution (b).

5.1 Ni/Cu(001) and Ni-like $\text{Ni}_x\text{Pd}_{1-x}/\text{Cu}(001)$

5.1.1 Ni/Cu(001)

In the following section we want to focus on the in-situ grown Ni/Cu(001) and Ni-like $\text{Ni}_x\text{Pd}_{1-x}/\text{Cu}(001)$ films with wedged and continuous-film geometry. A typical domain structure exhibited in a wedged Ni film, representative for the magnetic behavior of all grown Ni/Cu(001) films, is shown in the XMCD image in Fig. 5.1. The contrast is generated by exploitation of the XMCD effect according to the procedure of difference imaging described in Sect. 3.2.2. The film thicknesses throughout the wedge have been calibrated by fitting the Ni white line signal at 852.6 eV to the wedge geometry described in Sect. 3.1.1 and the plateau thickness determined by MEED during sample growth. Also magnetic domain formation comparisons from continuous films have been used to confirm certain reference points. A correction of the white line signal has been studied, considering the decreasing electron yield from buried atomic layers (see eIMFP in Sect. 2.5) [111, 113].

The displayed film's thickness ranges from ~ 5 ML at the left-hand side of the image to ~ 95 ML at the right-hand side of the image. Four areas of different magnetic behavior are marked in the Ni survey image above:

- (i) Starting on the thin side of the Ni film, displayed at the left-hand part of the image, we see a contrast-less, grey area up to a film thickness of about 10 ML. The amount of electrons detected by exciting with circularly left polarized light and circularly right polarized light is the same, resulting in a grey value of zero in the asymmetry image. A lack of contrast and a zero value in asymmetry theoretically may arise from too small

ferromagnetic domains which cannot be resolved and therefore averages to zero contrast. A decrease in domain size, however, would not find a reasonable explanation in this area as no transition area can be seen. Also, the contrast of the domains from the following area fades out with decreasing thickness. This behavior could only be satisfied in a 'decreasing domain size scenario' by disintegrating the 'macro' domains by an increasing number of 'micro' domains including a local imbalance in domains during the process. The 'micro' domains would have to be of a size less than the resolved 50 nm of detail measurements not shown here. Even though this scenario or an influence of the small magnetic field of the objective lens (<1 mT) cannot be completely ruled out, we assume that the loss of contrast in this area results from the paramagnetic state of the film. This effect is accounting for the CURIE temperature T_C , decreasing with film thickness in the thin film regime [58,173]. Previous studies found Ni/Cu(001) films ferromagnetic at room temperature down to a film thickness of about 4 ML [61,174]. The extended range of the non-magnetic phase up to 10 ML can be a) due to higher film roughness or b) an influence of our microscope itself (e.g. external magnetic field), as this effect was also observed on other film systems used in other studies. a) can be excluded by the MEED, LEED and AES characterization, confirming an outstanding film quality (see Sect. 4.2). b) also seems unlikely, which is discussed in a general context in a later paragraph (see Sect. 5.1.3). At this point, the question about the origin of this effect remains to be answered.

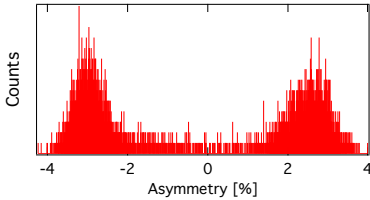


Figure 5.2 – Asymmetry histogram for phase (ii)

- (ii) Magnetic contrast can be observed at a sample thickness above ~ 10 ML in a quasi-monodomain state with an out-of-plane magnetization direction. The magnetization direction has been determined by azimuthal rotation experiments (see Sect. 3.2.2), showing a constant magnetic contrast independent of rotation angle. The contrasts were monitored by a histogram analysis that can be found in

Fig. 5.2, which shows two distinct peaks cor-

responding to the two magnetization directions. Magnetic domains can rarely be found and are of lateral sizes larger than a typical field of view of about $40\ \mu\text{m}$, which we call monodomain-like. Domains are mostly induced by topological influences creating stray fields acting on the dipole term of the anisotropy. The domains are of bubble type with domain walls that follow the segment of a circle with a radius much larger than the latitude of this magnetization state in the slope of the displayed wedge. This conclusion

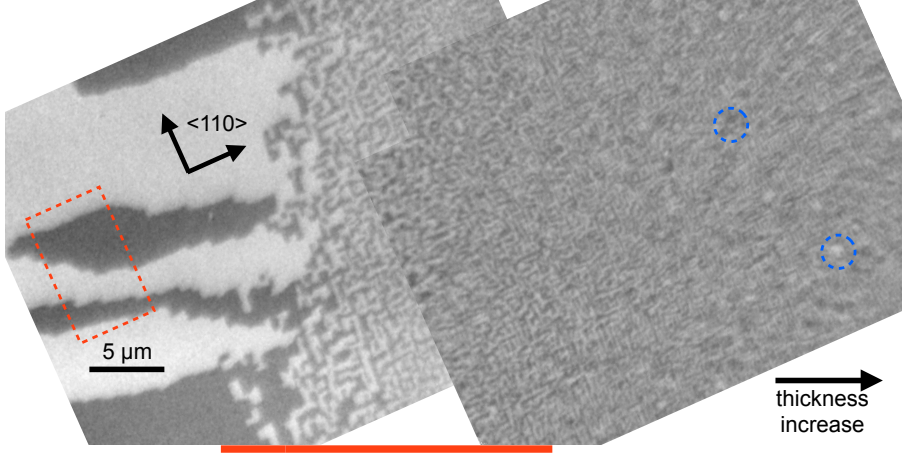


Figure 5.3 – XMCD image of a Ni/Cu(001) wedge at the Ni L_3 edge (852.6 eV), enlarged section from Fig. 5.1. Film thickness ranges from ~ 40 - 100 ML. The red bar underneath the figure denotes the x-axis range of the domain size analysis Figure 5.6. The dashed red rectangle denotes the area used for the histogram analysis shown in Fig. 5.4. Blue circles mark examples of the cloudlike domains superposing the rectangularly aligned domain pattern. Image distortion is creating deformation at the top-right part of the image.

is also based on observations along the wedge and comparable films shown later in this thesis [Fig. 5.10 c) & 5.24 a)]. Phase (ii) extends up to about 40 ML film thickness.

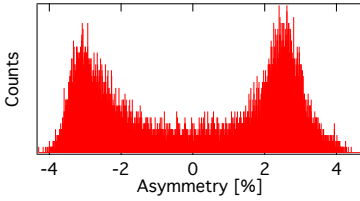


Figure 5.4 – Asymmetry histogram for phase (iii). The area used to extract the histogram is denoted by the red rectangle in Fig. 5.3

- Phase (iii) will be discussed for the example in Fig. 5.3, a stitched XMCD image depicting a magnified area of the survey image from 40 ML to 100 ML. The histogram analysis of phase (iii), depicted in Fig. 5.4, shows no significant variation from the analysis of the previous phase, which suggests no major change in the out-of-plane magnetization direction for this phase. However, a more stable domain formation is introduced in this phase. Domains of 2 to 10 μm width can be found, their length being limited by the length of

phase (iii) (here about $17\mu\text{m}$). Occasionally, the domain structure is interrupted by larger monodomain-like areas again. The domain elongation along the wedge inclination seems to be determined by the direction of thickness increase itself, since the elonga-

tion direction does not coincide with a crystallographic direction. Experimentally, this orientation has been determined by correlation of the first order LEED-spot directions (closest-packed axis) and the real-space imaging mode's rotations (see Sect. 3.2.5). Also, there is a small chance that the domain shape is a remnant of magnetization development during film growth that could not be removed by the demagnetizing procedure. The incorporation of misfit dislocations in a wedged film, however, might be predominantly developing along the wedge inclination direction during growth, serving as a domain wall attraction points after the demagnetizing procedure. Additionally, the domain walls show a strong 90° zig-zag-chain ordering along the crystallographic $\langle 110 \rangle$ -axes. Due to the domain elongation in the slope direction, which is closer to (110) than to (-110), the sides of the 90° zig-zag-chain, ranging from about 1 - 5 μm , are longer in (110) direction.

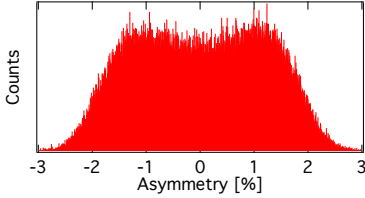
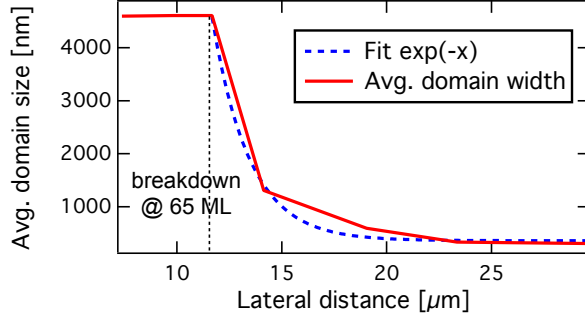


Figure 5.5 – Histogram from the SRT area as denoted in Fig. 5.8. Nearly symmetric distribution of contrast shows equal amount of both magnetization directions. The distribution with two distinct maxima is typical for two contrast levels, indicating a predominantly out-of-plane magnetized state.

- Phase (iv) presents a more complicated behavior, which will be described phenomenologically in this paragraph. However, a more detailed analysis in context of previous studies and the theoretical framework will follow later in this section. At a critical thickness of about 65 ML, a spontaneous breakdown of magnetic domain size can be found (see Fig. 5.3). The breakdown has been confirmed to occur in 70 ML (also see Fig. 5.8) but not in 60 ML plateau thickness wedges. From the critical thickness on, the average domain size decreases conforming to an e^{-x} -function with increasing thickness as displayed in Fig. 5.6.

A first analysis of the histogram values in this area, see Fig. 5.5, suggests an out-of-plane magnetization direction right after the breakdown. The peaks are not as clearly separated as before, as a result of the decreased domain size. The domain shape still follows the rectangular ordering introduced in phase (iii), which now can be described as a rectangularly ordered labyrinth domain pattern. As sample thickness increases, a superposition of the rectangularly aligned pattern with cloud-like domains increases in density and strength of contrast. We define cloud-like domains as contrast arrangements without a preferential shape or pattern like the two areas marked by blue circles in Fig. 5.3. Notably, while the rectangularly ordered domain pattern fades, the cloud-like domain arrangements are gaining in size and density. The following sections will argue

Figure 5.6 – Domain size of the rectangularly ordered labyrinth domain pattern extracted from Fig. 5.3 and the corresponding fit to an e^{-x} function. The x-axis area is marked in Fig. 5.3 by a red bar.



that we attribute the cloud-like domains to an in-plane magnetization and the patch-like increase of their appearance as the domain-state equivalent to the single-domain's canted state.

In the following paragraph, the described domain evolution in all phases will be compared to the theory of anisotropy evolution in Ni/Cu(001) in the single-domain framework described in Sect. 2.2, in order to establish a connection between the anisotropy evolution and the observed domain formations.

Experimental definition of the SRT In the data presented, we attribute the breakdown of domain width at 65 ML film thickness to the zero-crossing of K_2^{eff} and hence, the SRT. The magnetization direction of the domains in phase (iv) beyond the breakdown appears to be out-of-plane, which agrees to the measurements on the similar system of Cu-capped Ni/Cu(001), proceeding via a canted state through the anisotropy space, starting at zero canting angle upon zero-crossing of K_2^{eff} while maintaining a positive K_4^{eff} (see Fig 5.7). The cloud-like patches superposing with the rectangularly ordered pattern in the course of further thickness increase become more dense and larger. A path through the canted state is, in the single-domain picture, connected to an increasing canting angle with increasing film thickness. A slightly canted magnetization angle is of much lower contrast influence compared to the superposed out-of-plane domain pattern. Upon increase of the canting angle its projection on the k-vector of the incident light increases which is reflected by the contrast of the cloud-like patterns: There is no visible contrast directly after the breakdown, but more pronounced cloud-like patches with further increasing thickness. While all studies identifying the SRT in a canted state have been measured under applied magnetic field, creating a single-domain in the sample [31, 76, 175, 176], the data presented here show its remanent domain-state analogon.

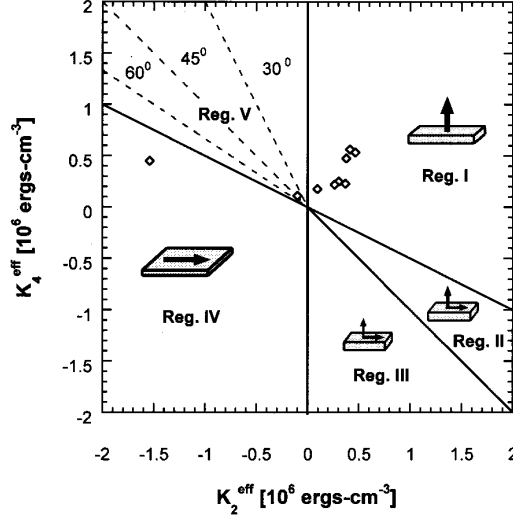


Figure 5.7 – Anisotropy space of K_4^{eff} vs. K_2^{eff} . Diamonds are datapoints of the Cu/Ni/Cu/Si(001) system, thicknesses between 30 Å and 150 Å + 2220 Å measured by HA & O’HANDLEY. The system is performing an SRT via canted transition. From [76]

HA et al. determined the dependence of K_4^{eff} on the film thickness with torque magnetometry for Cu/Ni/Cu/Si [76]. They found the K_4^{eff} to be positive for all film thicknesses up to 200 nm of Ni (see Fig. 5.7), which creates a path through anisotropy space that is consistent with the interpretation of the domain patterns above.

Comparison of phase (iii)- and (iv)-data to the single-domain phenomenological model of anisotropy More insight in the images taken from the Ni wedge can be gained if the evolution of the uniaxial anisotropy (see Sect. 2.2) is taken into account. If we take a closer look at the leading uniaxial anisotropy term K_2^{eff} , we find agreement with the development of the domain structure seen in Figs. 5.3 & 5.8. In between the two zero-crossings, the uniaxial anisotropy of second order should have a maximum at about 3 nm film thickness, as deduced in the publications by BOCHI [91] and HA [76]. This thickness falls into phase (ii), showing domains of bubble type, which are a typical example of higher uniaxial anisotropy materials [34]. Upon thickness increase and decrease of K_2^{eff} , the significance of all other magnetic influences rises. The rectangularly aligned domain structure of phase (iii) reflects this development and is caused by an influence of either topographic or magnetic in-plane anisotropic origin. The influence of topographic

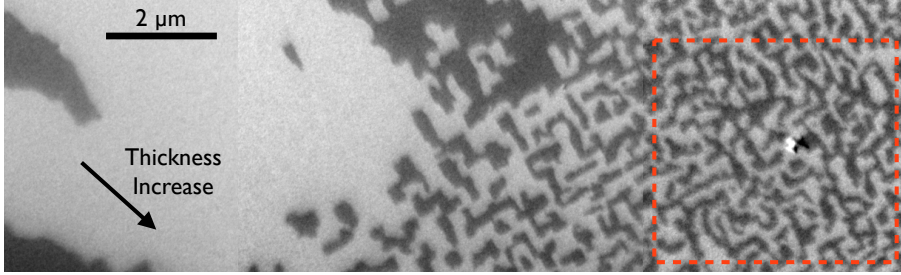


Figure 5.8 – Image of the SRT area in a 70 ML Ni/Cu(001) wedge. Domain wall orientation along $\langle 110 \rangle$. The red rectangle denotes the area used for the histogram analysis in Fig. 5.5

features will be discussed in Sect. 5.1.2 with additional LEEM data. A following paragraph on the comparison of our results with literature concerned with micromagnetic simulations will shed more light on the creation of four-fold symmetric domain patterns by magnetic properties alone. The 4-fold symmetric behavior and orientation along the crystallographic axes show that the strength of the uniaxial anisotropy is decreasing, as proposed in the model. The findings of HA & O'HANDLEY show a transition of the similar Cu/Ni/Cu/Si(001) system through the canted state [76]. As described above, we find an increase of cloud-like patches superposing the rectangularly aligned domain pattern, which we denote as the multi-domain state of the canted SRT in the single-domain picture. In the canted state, the (negative) uniaxial anisotropy is by definition not strong enough to create an entirely in-plane magnetized state, which explains the persistence of the rectangularly aligned pattern in the canted state. It is not clear, however, whether the size of the rectangularly ordered domains decreases in an approach to a size below the resolution limit or the canting of magnetization direction is completed with a finite domain size, as the canting process is not completed at the film thicknesses of 100 ML we grew (see the remaining rectangularly ordered pattern in Fig. 5.3).

The phenomenological ansatz of the anisotropy constant's evolution is in good agreement with the behavior seen in the presented data, not only does it reproduce both SRT thicknesses, but it also is consistent with the domain evolution. Yet, it cannot make any predictions on the domain pattern exhibited in remanent and demagnetized states. A comparison to literature on imaged SRTs and micromagnetic simulations from literature will help to understand the magnetic system on a microscopic level in the following paragraph.

SRT comparison with literature in the single-domain anisotropy framework The data from BOCHI et al. [91] and FARLE et al. [97] combined with the underlying theory of anisotropy contributions to the uniaxial anisotropy shown in Fig. 2.7 reproduces the two thicknesses of SRTs in Ni/Cu(001) first combined in a single study by SCHULZ et al. [32]. While the inverse SRT is supposed to occur at film thicknesses of about 7 ML [32, 97], where no magnetic contrast could be observed in our study (see Fig. 5.1), the SRT at moderate thicknesses is found in literature to be between ~ 35 and 60 ML [31, 32, 76, 90, 91, 174]. However, all studies on the SRT at moderate thickness have been conducted on the similar Cu(2nm)/Ni/Cu(001) system. Studies comparing the SRT thickness of the capped with the uncapped system found a shift of both reorientation transitions to higher thicknesses for the Cu-capped system [91]. While ZHAO et al. confirmed the shift for the iSRT of ultrathin Ni on Cu(001) single crystals [177], O'BRIEN et al. found a shift to the opposite direction [174]. This shift has to be taken into account when comparing the SRT thicknesses in the domain imaging experiment.

The extended range reported for the SRT in the above studies originates from two main effects: Firstly, the temperature dependence of the anisotropy constants will shift the SRT and secondly, the nature of the SRT, not being a first order transition, makes it hard to define an exact thickness for the transition. The previous studies on the SRT at moderate thicknesses have been conducted on the Cu/Si(001) substrate, which introduces a significant amount of interface roughness of $\pm 2 \text{ nm} \hat{=} 11 \text{ ML}$ [91] to the system. Main driving parameters for the SRT are the surface and interface anisotropy contributions of the system as discussed in Sect. 2.2. Hence, the interface roughness and resulting Ni-film surface roughness are of great influence on the SRT thickness. Our shift of the SRT thickness to higher film thicknesses is in agreement with SCHALLER et al., who found smooth surfaces to enhance the PMA compared to rough surfaces [178]. In summary, the extended range of SRT thicknesses reported in literature has been either deduced from samples with a Cu capping, samples with a considerable amount of interface and surface roughness, or both. Surprisingly, there is a good match for the critical SRT thickness between Cu/Ni/Cu/Si(001) samples and our study on uncapped Ni/Cu(001). We suspect that the Cu capping introduced interface anisotropy at least partly compensates the anisotropy arising from the interface roughnesses.

The domain evolution from a micromagnetic point of view Data on SRTs and imaging of domain formation are scarce so far. Comparable data can only be found in the microscopic experiments on SRTs in ultrathin ferromagnetic films of few ML thickness as Co/Au(111) [81, 179], Co/Au(001) [25], Fe/Cu(001) [88, 180–182]. Even though the

SRTs have been imaged depending on either thickness or temperature, the domain size variation in the vicinity of the SRT is a common feature of all studies cited. However, the manifestation of the SRT is subject to a considerable variation regarding order and transition length for second order transitions, as are the domain structures themselves. This chapter aims to find coinciding features between ultrathin-film SRTs and the SRT in Ni/Cu(001) at moderate thicknesses of about 65 ML.

SPECKMANN et al. [179] and OEPEN et al. [27] showed images from Co/Au(111) obtained by scanning electron microscopy with polarization analysis (SEMPA), which document the decrease of domain size in the vicinity of the SRT. SPECKMANN et al. found the reduction of domain size to be more pronounced for post-annealed samples opposed to the as-grown Co/Au(111). The study documents a smoothing effect on the Co film with a more homogeneous distribution of film thickness, resulting in a domain size increase of far-from-SRT-domains. These findings document the important influence of surface properties on the domain formation in general, but also the stability of SRT domains regardless of the surface smoothness variations, since their size has not been influenced by the annealing procedure. Eventually, they were able to fit the domain size decrease to the theoretical predictions made by KAPLAN and GEHRING [183], who proposed a dependency of the domain width on the film thickness, wall energy and uniaxial anisotropy.

CHOI et al. showed an SRT in Fe/Ni/Cu(001) depending on the Fe and Ni thicknesses [184]. They could modify the domain appearance from bubble type to labyrinth-domains by applying magnetic fields. The domain-width dependence of thickness, which was already reported on by WON et al. [185, 186], did not change at all, which constitutes a crucial and consistent role of the domain size in the SRT.

In the case of fcc Fe/Cu(001) reported by PORTMANN et al. [182], a domain transformation has been observed depending on the sample temperature. As already pointed out by the authors, changing the so called effective temperature affects the anisotropy in a similar way the thickness of the film does. Upon increasing the temperature on a miscut ($\sim 3^\circ$) and therefore stepped substrate, the orientational melting of the labyrinth phase resulted in 90° corners in the domain pattern. While shear stress (due to the miscut) might be the most reasonable explanation to the resulting domain structure in their case, the crystal used for our Ni/Cu(001) films is specified to be $<0.3^\circ$ miscut, also proven by the LEEM analysis shown in Sect. 4.1, leaving shear stress as a result of miscut most unlikely.

PIERCE et al. showed for Fe/Cu(001) that the transformation called 'melting of stripe domains', as introduced by VATERLAUS et al. [180], is a feature of the onset of an SRT,

rather than the ferromagnetic/paramagnetic transition [181]. Again, in the vicinity of a temperature driven SRT, domain size reduction could be found. It has to be taken into account, that the Fe/Cu(001) films used in this study are subject to a complicated set of structural and morphological phase transitions in the same thickness region.

As shortly mentioned before, KAPLAN & GEHRING [183] calculated the domain width of perpendicularly magnetized thin films depending on film thickness, domain wall energy and hence uniaxial anisotropy. The calculated energies of stripe and checker domain patterns were found to be extremely close and to have the same functional dependence on the film thickness [183]. They predicted a linear dependency for the domain width of the film thickness h if the film is thinner than the exchange length λ_{ex} . Films thicker than the exchange length were found to be proportional to $he^{\sigma_w/(M_s L)}$, where σ_w is the domain wall energy per unit area.

The measured SRT at 65 ML ≈ 11.5 nm is in a thickness range slightly above the exchange length of $\lambda_{ex} = \sqrt{\frac{A}{\frac{1}{2}\mu_0 M_s^2}}$. For BLOCH walls, the domain wall energy per unit area can be expressed as $\sigma_w = 4\sqrt{AK_u}$, with the uniaxial anisotropy as derived in Sect. 2.1.3. Considering the moderate increase of thickness in the SRT area at 65 ML, we assume it to be constant. The uniaxial anisotropy close to its zero-crossing is subject to severe variation due to the thickness and therefore also strain dependent terms. At the point of the zero-crossing, the theoretical wall energy approaches zero, and thereby the domain width approaches zero. While this model does not take additional effects into account such as in-plane/higher order anisotropies, we find the model qualitatively in good agreement with the observed behavior in phase (iv) of the Ni/Cu(001) film.

In conclusion, the domain size reduction can be found in virtually any microscopic SRT study. The domain shape and patterns, however, find a wild variation in an inter-material comparison. The same can be stated with respect to the study in this thesis, even though the SRT film thickness is about one order of magnitude thicker than typical SRTs. While the domain pattern evolution with the rectangular arrangement of domain walls is the first of its kind to be reported on, we find the common characteristic of domain size reduction as another indication that the SRT in Ni/Cu(001) is described correctly in the micromagnetic approach. Finally, the model of KAPLAN & GEHRING (by balancing the wall energy and the dipolar energy in stripe and checker domain patterns) can describe this domain size reduction found in our films upon entering the canted SRT area.

SRT comparison with literature on micromagnetic simulations Micromagnetic simulations based on magnetic lattice systems, typically of cell size of the order of the magnetic coupling length, tackle the evolution of phase transiting systems from a microscopic

point of view. These simulations yield a self-assembled magnetic state, including magnetic domain formation for energy minimization purpose. A couple of studies have been published since ALLENSPACH et al. first reported on domain formation in Cu/Au(111) during the SRT [25]. In this paragraph the presented results on Ni/Cu(001) are reviewed with a focus on the domain formation with respect to simulations.

The first theoretical work on the domain formation throughout magnetic phase transitions was published by ABANOV et al. [33], strongly building upon earlier work by KASHUBA et al. [187, 188]. Their method involved a combination of microscopic calculations and phenomenological assumptions calculated on a square lattice HEISENBERG spin system. The following Hamiltonian is utilized for the simulations:

$$\begin{aligned}
\mathcal{H} &= \mathcal{H}_{\text{an}} + \mathcal{H}_{\text{ex}} + \mathcal{H}_{\text{dip}} + \mathcal{H}_{\text{dw}} \\
&= -K \sum_i S_{iz}^2 && \text{perpendicular magnetic anisotropy} \\
&\quad -J \sum_{ij} \mathbf{S}_i \cdot \mathbf{S}_j && \text{exchange energy} \\
&\quad + \frac{(g\mu_B)^2}{2} \sum_{ij} \frac{(\mathbf{S}_i \cdot \mathbf{S}_j) - 3(\mathbf{S}_i \cdot \boldsymbol{\nu})(\mathbf{S}_j \cdot \boldsymbol{\nu})}{x_{ij}^3} && \text{dipole energy} \\
&\quad + 4\sqrt{JS^2\lambda_{\text{eff}}} && \text{domain wall energy}
\end{aligned}$$

with K being the uniaxial anisotropy coupling constant, S_z the out-of-plane component of the spin \mathbf{S}_i . J is the exchange coupling, and g the dipolar coupling constant. μ_B denotes the Bohr magneton, $\boldsymbol{\nu}$ a unit vector pointing from one lattice site \mathbf{x}_i to another \mathbf{x}_j , and λ_{eff} denotes the total effective spin anisotropy. Energy minimization of this Hamiltonian yields a phase diagram depending on temperature with six phases: monodomain-, smectic crystal-, ISING-nematic-, tetragonal liquid-, planar- and paramagnetic phase, from lowest to highest temperature. In the smectic crystal phase stripe domains that favor two, mutually perpendicular, directions are found for the calculated thin film sample. The stripe domain follows a long-range orientational order, while the positional order falls off algebraically. The following ISING nematic phase changes to an exponential decay of the positional order. The sample is supposed to show regions of striped domains along one of the two mutually perpendicular directions, which are given by the substrate's crystallographic structure. In a final stripe-domain phase, the tetragonal liquid phase, the tetragonal symmetry is restored. This is reasoned by proliferation of the stripe-area separating 'stripe rotation domain walls', resulting in an exponentially rapid spatial decorrelation between the two stripe orientations. This phase is supposed to be close to a possible SRT, which introduces the planar phase. The paramagnetic state

is reached upon further increase of the temperature. The evolution of a system along the proposed path through the phase diagram is not affected whether or not the system eventually exhibits a spin reorientation. In contrast to the experiments conducted in this thesis, the calculations have been made depending on the system's temperature, not film thickness. However, due to the intertwined relations between temperature and the anisotropy constants, the evolution of a system with increasing thickness can be similar to the evolution with t/T_c .

We find a striking resemblance between the phase transition diagram which was calculated by ABANOV et al. and the data presented on $\text{Ni}/\text{Cu}(001)$ in the previous sections. The monodomain- and tetragonal liquid phases can be identified easily in Fig. 5.1, while the canted state of the SRT leads to the planar phase. Arguably, the smectic crystal and ISING nematic phases find a counterpart in phase (iii) described for the $\text{Ni}/\text{Cu}(001)$ system, as we found a strong ordering of domains along the wedge inclination. Strong deviations from the actual stripe domain pattern are predicted by the authors for real samples, which can be introduced by various material parameters which are not taken into account by their model. Phase (ii) falls out of the comparison completely, since the variation of the uniaxial anisotropy in this thickness regime does not coincide with the anisotropy variation with temperature.

In comparison to our experimental results, the calculations from ABANOV et al. do not give any domain formations, but are solely based on general energy contributions. Models based on a simplified version of the described Hamiltonian in a 2-dimensional framework did lead to simulations which are more closely related to the domain structure. In the following, some of this work will be compared to our experimental results.

BOOTH et al. [189] performed Monte Carlo (MC) simulations with a simplified Hamiltonian consisting of dipolar and exchange terms. The system shows three phases [(a)-(c)] depending on temperature, - (a) a stripe phase, (b) a phase without long range order (consisting of irregular but well-defined domains) and (c) a fully disordered phase. At the breakup of the stripe domain phase, the calculations found domain formations that orient mainly along the closest-packed axis of their MC-grid. With increase of relative temperature the characterizing order parameter decreases further, giving rise to domain orientation along arbitrary directions, but with domain wall orientations preferential along the two closest-packed direction. Eventually, the order is completely lost as the temperature approaches the paramagnetic limit. As the authors conclude, the qualitative features of systems undergoing phase transitions can be explained by micromagnetic calculations, which we find in agreement with the experimental investigations displayed in the previous sections. The rectangular order of domains does not seem to be a fea-

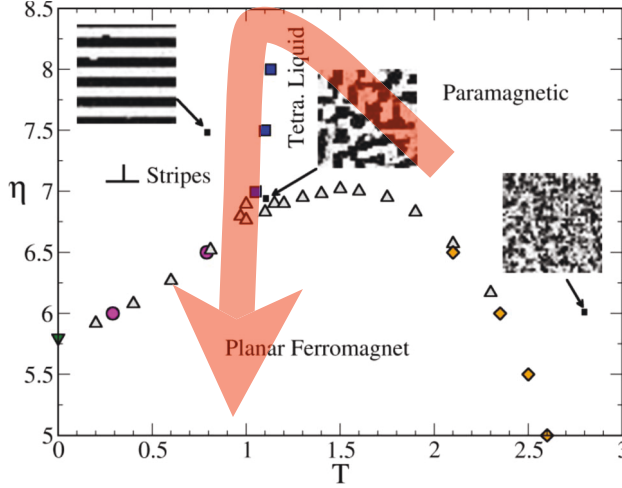


Figure 5.9 – Phase diagram from Monte Carlo simulations on a two-dimensional HEISENBERG model for ultrathin films, depending on a normalized T , with perpendicular anisotropy coupling $\eta = K/g$ and an $J/g = 3$. Taken from [190]. The overlay of the red arrow is a tentatively proposed pathway for the investigated Ni/Cu(001) system.

ture of the domain walls only, but might be promoted by exchange and dipolar energy contributions alone. However, we believe that in a real-life system, fluctuations and energies by domain-walls, domain-wall pinning, and lattice distortion are able to prevent or promote the calculated domain formations.

MACISAAC et al. performed similar MC simulations under the inclusion of an out-of-plane anisotropy term [191]. Comparable simulations have been carried out more recently by CARUBELLI et al. in a varied parameter range [190], agreeing with the previously presented studies. Depending on the ratio $\eta = K/g$ and temperature T (normalized to a critical temperature), a phase diagram with three magnetic phases [(a) - (c)] is found, - (a) planar ferromagnetic, (b) orientationally ordered striped phase at low T , and (c) a tetragonal phase at high T . The slope of the phase transition between planar and stripe phase depends sensitively on the relative strength of the exchange constant J (see Fig. 5.9), which does not affect the qualitative discussion in this section. The phase diagram is consistent with the one found by ABANOV et al. [33]: The T -axis of ABANOV can be depicted as one trajectory through the η and T space, and connects this trajectory to domain structures similar to the ones found by BOOTH et al. [189]. From these results, we can interpret the observations on the Ni/Cu(001) sample system

presented in the previous sections in a theoretically understood framework. The path of our real system through the phase diagram of CARUBELLI is determined by the change of $\eta = K/g$, which can be identified with a proportionality to the uniaxial anisotropy of the Ni/Cu(001) films. The relative temperature of the system Ni/Cu(001) is decreasing with increasing thickness due to the reduced T_c at low film thicknesses according to Fig. 2.2. As shown in the evolution of the uniaxial anisotropy K_2^{eff} (Fig. 2.7) and in the data from our wedged Ni film, the uniaxial anisotropy increases in phases (i) and (ii) and decreases with film thickness in phases (iii) and (iv), determining the general path along the $\eta = K/g$ axis. In order to exhibit a rectangular domain order in line with the phase diagram, the transition has to proceed through the tetragonal liquid phase close to the triple point on the right-hand side of the tetragonal liquid border. A general idea about the performed path through the phase diagram for the Ni/Cu(001) system is sketched into the phase diagram by CARUBELLI et al. shown in Fig. 5.9. However, without a calculation utilizing the specific parameters of our system the discussion must remain on a qualitative level.

SARJALA et al. [192] and FONSECA et al. [193] performed Monte Carlo simulations of a two-dimensional ISING model with dipole interaction with and without the influence of oscillating magnetic fields. The domain structures yielded by their method are of striking resemblance to the domain structures in our rectangularly aligned phase. The magnetic fields show an enforcing effect on the size of rectangularly aligned domains, which however, could also be found without magnetic fields. Hence, it might be possible that the demagnetizing procedure (Sect. 3.2.4) enhances the rectangularly ordered domain structure seen in our images. However, the rectangular order is reported not to appear if the sample is not receptive for this structure, i.e. the order can be considered an energetic ground state.

First experimental confirmation for the theoretical work by ABANOV et al. [33] has been reported by HOFFMANN et al. [194] on Ag/Fe/Ag films. In a very small thickness regime between 3.34 ML and 3.77 ML they found domain formation changes in the perpendicularly magnetized iron from striped domains to isotropic domains. While being consistent with theory, the phase diagram could only partly be represented by the study. The difference in exhibited domain formation with respect to this study also shows that conformation to the phase diagram can be achieved with various actual domain geometries that find local energy minima.

As we can find in the studies presented in this section, the rectangularly aligned phase imaged in the vicinity of the SRT in our study is in strong agreement with the presented theoretical predictions, which were already supported by simulations.

The simulation parameters gravely influence the overall domain evolution in their final appearance, which results in varying and non-distinct manifestations of the domain patterns. Introduction of the material parameters would be needed for micromagnetic simulations to yield quantitative results for the films of interest in this study. Also, implementing the development of uniaxial anisotropy with film thickness could simulate the wedged film behavior. Simulations of such kind would be a powerful tool to gain further knowledge about the mechanisms driving the SRT via the rectangularly aligned state observed in our XMCD-PEEM images.

5.1.2 Ni-like Ni_xPd_{1-x} films on Cu(001)

In order to gain further knowledge on the system and explore the influence of lattice strain, we grew NiPd alloy films of various composition in wedged and continuous film (CF) geometry on Cu(001) single crystals (see Sect. 4.3). Ni-like Ni_xPd_{1-x}/Cu(001) films show a similar behavior of anisotropy development, including PMA, in comparable thickness ranges as the Ni samples discussed in the previous sections. Due to extensive evaporation durations, they were not grown up to thicknesses exhibiting an SRT. Nevertheless we will investigate whether the observed domain patterns agree with our interpretation introduced for pure Ni/Cu(001). Moreover, because the thickest samples of 60 ML seem to be close to the SRT area, deduced from domain formation comparison. Fig. 5.10 a) shows a Ni₈₈Pd₁₂-wedge with a plateau thickness of 60 ML. The described phases (i) to (iii) can be identified in this wedge with slight differences in their detailed structure. Phase (ii) shows domains on a regular basis, which can be understood by the K_2^{eff} behavior: Alloying Pd into the Ni decreases the lattice mismatch as described in Sect. 4.3.2, hence decreasing the magnetoelastic and strain-dependent terms in Eqn. 2.2. As a result, the maximum of K_2^{eff} will be less pronounced, leading to different behavior in domain formation. The domains clearly show curved domain walls without a preferential orientation, emphasizing the bubble-domain type. With increasing thickness, the in-plane anisotropy gains more influence, aligning the domain walls along the $\langle 110 \rangle$ -axis. The effect can be seen in a single domain in the middle of the image, which has curved domain walls on the thinner film side, while the domains on the thicker film side start to align to the crystallographic directions. The sample keeps this state of domain wall alignment along the $\langle 110 \rangle$ -axes throughout the grown wedge up to the 60 ML plateau thickness. Up to the plateau, the domain size is continuously decreasing, with a plateau domain width of about 1-10 nm.

A very similar domain structure is found for a 60 ML continuous film sample of Ni₉₃Pd₇,

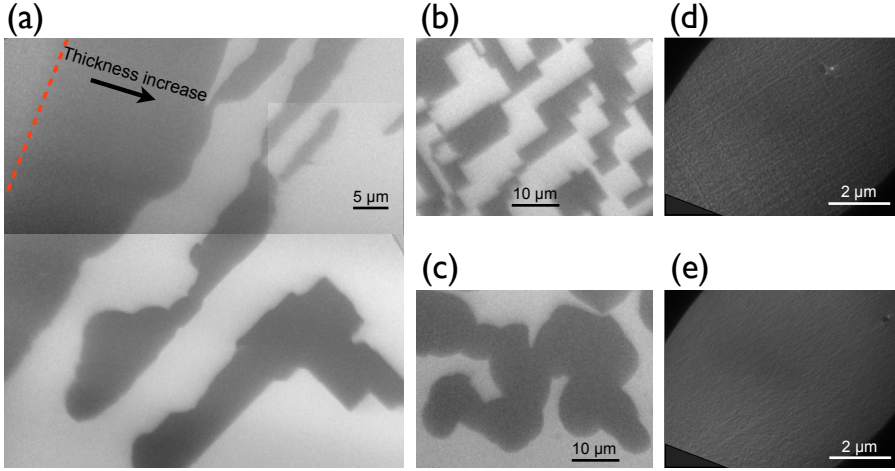


Figure 5.10 – XMCD images from Ni-like films on Cu(001). Survey image of a $\text{Ni}_{88}\text{Pd}_{12}$ wedge area, thickness ranging from ~ 5 ML to ~ 45 ML (a), $\text{Ni}_{93}\text{Pd}_{07}$ continuous film samples at 60 ML (b) and 30 ML (c), the respective LEEM images (d) and (e).

shown in Fig 5.10 b). Both, the plateau area from the wedged sample shown in a) and the continuous film sample from b) show a homogeneous distribution of domain width in both directions. On this basis we conclude that the preferential ordering of domains along one of the rotationally equivalent $\langle 110 \rangle$ axes is a feature induced by the wedge geometry or its magnetic growth history. Fig. 5.10 c) shows the same sample on a second continuous film step of 30 ML thickness. The films have been grown as a two step film of 30 ML & 60 ML thickness on a circularly shaped Cu(001) substrate with a diameter of 6.5 mm, leaving at least 3 mm step width for each continuous film. Falling in phase (ii), the domains found on the 30 ML CF sample are of the bubble type. In a similar way as found in wedged samples of $\text{Ni}_{88}\text{Pd}_{12}/\text{Cu}(001)$ and $\text{Ni}/\text{Cu}(001)$, no domain wall ordering is visible, the walls form along connected segments of circles. As found for the 60 ML film, the domains' shape is of isotropic width as there is no bias from a wedge geometry. However, the film tends to form large monodomain areas. Domain formations can be found regularly on the sample, without significant influence by local variations such as topological features.

LEEM studies at the MEM-LEEM transition (see Sect. 3.2.2) have been conducted to observe the surface structure of the $\text{Ni}_x\text{Pd}_{1-x}$ film. Images from the CF NiPd samples are shown in Figs. 5.10 d) & e). The areas correspond to the central part of the XMCD

images displayed in b) & c). In order to compare the features from LEEM and XMCD images it is notable that the magnification of the images are different. The 60 ML film exhibits lines of strong contrast along the $\langle 110 \rangle$ axes, produced by topographical modification of the electrical field above the sample. Axes between fields of view and the diffractive plane have been taken into account as a result to the determination of image mode rotation discussed in Sect. 3.2.5. The 30 ML film only shows hints of this ordered structure, while generally being dominated by a slight roughness typical for grown films without post-annealing procedure. Since both films were grown next to each other on the same substrate in the same evaporation process, a difference on the basis of sample growth or initial substrate morphology can be excluded. The occurrence of the contrast lines on the 60 ML film hence is a feature of the growth process of Ni on Cu(001) itself. We denote them to an accumulation of few monolayers' height in the surface of the film, caused by the introduction of misfit dislocations (MD) to balance the lattice mismatch between the Cu substrate and the Ni or Ni_xPd_{1-x} film. A similar network of MD formation has been found in transmission x-ray microscopy studies on thinner Ni/Cu(001) films [91, 170]. In line with their studies, the density of MDs will increase with film thickness, explaining, why they cannot be seen in our 30 ML films. However, we did not see this kind of contrast for all Ni-like films of similar thickness, meaning that the strength of the MD accumulation is subject to variation upon sample growth. This variation seems to affect the MD accumulation much stronger than it does affect the magnetic domain formation. Taking the length scales of the occurring effects into account emphasizes their disconnection. While the magnetic domains are of μm size, the contrast lines in LEEM occur in a regularity of $\leq 150\text{ nm}$. Also, larger topographical features as seen in the top right of Fig. 5.10 d) do not influence the magnetic pattern in the XMCD image c). Agreeing with the theoretical predictions and simulations presented in Sect. 5.1.1, we therefore believe that these MD formation is not giving rise to the magnetic domain formation in the first place. Both effects are driven by the same physical means, the relaxation of film strain, resulting in MD formation and magnetic anisotropy, respectively.

Domain wall behavior in the rectangularly aligned phase Domain walls play a crucial part in the domain formation process since their energy contribution is strongly related to the shape of the domain [34]. In higher magnified images from a 60 ML plateau of a Ni₈₈Pd₁₂ wedged sample a considerable contribution of domain walls to the XMCD contrast can be found as displayed in Fig. 5.11 a). The domain wall length not oriented along $\langle 110 \rangle$ direction accounts for only 2 % of the domain wall length in this image. This

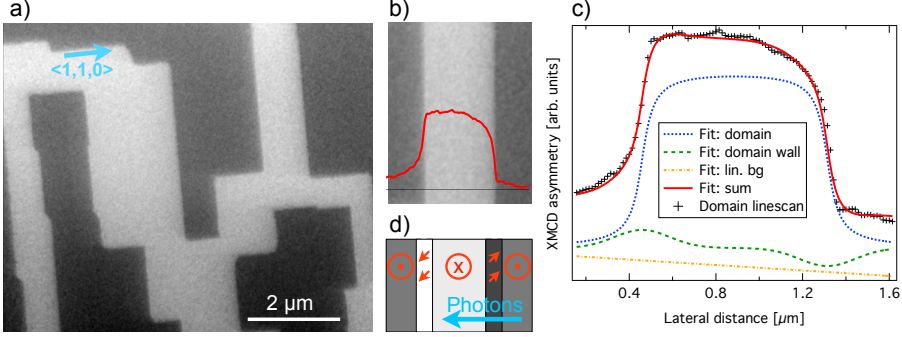


Figure 5.11 – Plateau area of a 60 ML $Ni_{88}Pd_{12}$ wedged sample (a). Enlarged section from a), with overlaid linescan of 30px width (b), mathematical fit to the lineprofile (c), magnetization scheme (d). Fit contributions have been offset separately for clearer display. Further explanations in text.

deviation emphasizes the conclusions about the topographical features: A significant amount of deviations follows one of the $\langle 100 \rangle$ directions, whereas no counterpart could be found in the LEEM images as shown in Fig. 5.10. A closer look at the domains reveals an edge contrast as seen in the enlarged section in Fig. 5.11 b). A linescan perpendicular to the stripe reveals an asymmetric XMCD brightness distribution of the out-of-plane domains, suggesting an in-plane domain wall contribution. In order to understand the produced XMCD signal, the linescan has been modelled by a least squares fitting under the assumption of a function with three terms, representing the domain contrast, the domain wall contrast and a linear background contrast due to beam asymmetries.

$$\begin{aligned}
 f(x) = & \quad m * x + a && \text{linear background} \\
 & + b * \{ \arctan[c * (x - x_{wl})] - \arctan[c * (x - x_{wr})] \} && \text{domain} \\
 & + d * \left\{ \frac{1}{e} * \exp[-(x - x_{wl})^2 / (e^2)] \right\} && \text{domain wall} \\
 & + d * \left\{ -\frac{1}{e} * \exp[-(x - x_{wr})^2 / (e^2)] \right\} && \text{domain wall}
 \end{aligned}$$

where $x_{wl,rl}$ denote the positions of the domain walls. a, b, c, d, and e are fitting parameters. This function is not taking offsets from the 25° inclination angle of the incident photons into account, since there is no sign of characteristic positive or negative excursion of magnetic contrast. The results from the fit can be seen in Fig. 5.11 c). Rotation experiments revealed a contrast connected to a magnetization rotation in the domain wall via $\langle 100 \rangle$ -directions, which can be seen in Fig. 5.12. This domain rotation path is reflected in the sketch of the magnetization contributions in Fig. 5.11 d). The fit

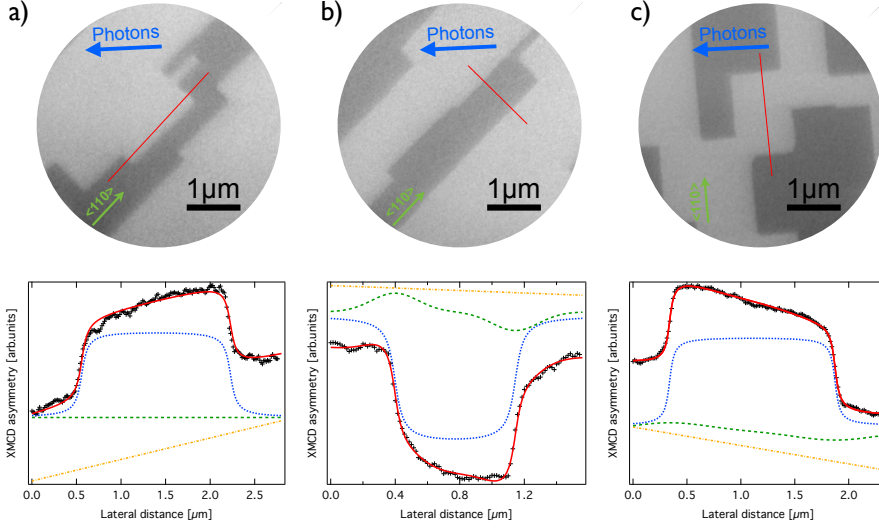


Figure 5.12 – 30px linescans perpendicular to the two domain wall directions, and the corresponding linescans including fits as described in text. Legends for fits can be found in Fig.5.11 d). 50° sample rotation in (a) and (b), with respect to (c) and Fig.5.11 d). The results shown in a) are fitted without domain wall contribution, b) and c) did not find reliable fits without planar contribution along photon **k**.

also indicates a domain wall width of about 300 nm, which is reasonable for NéEL-type walls given the film thickness of about 10 nm [34].

The rotation experiment, images and fits shown in Fig.5.12, aligns the **k** of incoming photons approximately with the <110>-directions and the <100>-directions. The observed contrasts feature the planar contrast contribution in the fits. Fig.5.12 a), as an exception, could also be fitted without the planar contribution. Combining these contrast findings under the assumption that the 4-fold symmetry also applies to the domain walls, the magnetic transition follows a path symbolized in Fig.5.11 c).

Additional information from the linescans can be found in the transition lengths of the perpendicular and the planar part of the magnetic moment's rotation: The planar contrast contribution to the rotation develops over about 300 nm (FWHM of the gaussian fit), the perpendicular contrast changes between its two easy axes within about 100 nm (16%-84% of contrast increase). Also, the magnitude of the planar contribution is smaller by a factor of five.

These findings lead us to the following conclusion: The differences in rotation length

suggest a screw-like rotation of the magnetization vector, starting with the rotation along the domain wall direction earlier than with the rotation perpendicular to the wall. Taking the film thickness into account, we therefore suggest that the rotation documented in this paragraph occurs upon approaching the transition between NÉEL- and BLOCH type of domain walls due to thickness related efficiency of the wall types [34, 195, 196]. The studies suggest film thickness of about 20-30 nm, while the films under investigation are of ~ 10 nm thickness. Higher spin-orbit coupling from the Pd intermixture and varying material parameters for out-of-plane magnetized Ni films grown on Cu(001) might add to the deviation from these predictions.

Deviations from our model may arise since the background XMCD signal caused by the beam asymmetry is not of linear nature and since the azimuthal rotation of the proposed planar contribution to the domain walls is not perfectly perpendicular to the \mathbf{k} of incoming photons.

The domain wall profile is also deformed by higher anisotropy contributions as K_4 (as discussed for 180° walls in 3.6.2(A) in Ref. [34], which is not taken into account in the applied model. According to the previous sections and the experimental confirmation from HA & O'HANDLEY et al. [76], the ratio K_4/K_2 diverges upon reaching the SRT due to the zero-crossing of K_2 , which would be a prominent case for a major influence of K_4 . However, with a value of $K_4/K_2 \geq 1$ (K_2 deduced from Fig. 2.7 and K_4 deduced from Fig. 5.7), this effect is of minor influence in the area of the imaged domain patterns (see Fig. 3.60 in Ref. [34]).

5.1.3 Summary Ni and Ni-like $\text{Ni}_x\text{Pd}_{1-x}$ films on Cu(001)

The presented data of Ni/Cu(001) show a breakdown of domain size at about 65 ML, which is identified as the onset of the SRT with out-of-plane and in-plane contributions found in a superposition of two characteristic domain patterns, the rectangularly aligned out-of-plane and the cloud-like in-plane pattern. This is interpreted as the remanent domain-state manifestation of the canted state found in single-domain theory and measurements on sample systems similar to the Ni/Cu(001) films presented in this study. The evolution of the domain pattern is in agreement with the development of the uniaxial anisotropy given in the same framework. While the domain formations of SRTs in ultrathin films find no resemblance to the findings in this study, the typical domain size decrease seems to be a common feature, which does not relate to the film thickness of SRTs. A closer look from the micromagnetic point of view finds the domain structure to be in agreement with phase diagrams obtained from micromagnetic Monte

Carlo simulations, forming a proof of the legitimacy and connection of both approaches. Ni-like Ni_xPd_{1-x} films have been grown on Cu(001) to check for a similar behavior in domain formation, confirming the findings on Ni/Cu(001) films up to the SRT. The domain patterns found in the PMA region of the investigated films could be interpreted in the framework of the single-domain development of the uniaxial anisotropy. A more distinct and ordered domain pattern in the rectangularly aligned phase before entering the SRT regime may be enhanced by an increased spin-orbit coupling of the intermixed Pd atoms, increasing the bi-axial in-plane part of widely neglected magnetocrystalline anisotropy [91]. LEEM measurements show surface features connected to the formation of misfit dislocations for film thicknesses that exhibit the rectangularly aligned domain structure. However, size comparisons and the micromagnetic calculations from previous studies suggest that the ordering of domain walls is an effect driven by magnetic anisotropy, which at the most might be enhanced by the surface features as seen in Fig. 5.10. Profiling and fitting of the domain walls gave insight to the transition path of the magnetic moments while opening up new questions about the transition between NÉEL and BLOCH walls, which need to be addressed by further studies.

Critical annotations to the results A few effects in connection to the presented measurements, which have not been pointed out before, will be discussed in this section.

The objective lens creates a magnetic field of less than 1 mT at the location of the sample [197]. We refrained from treating the influence of the field in the extensive anisotropy flow concept under the influence of a magnetic field [29, 30], since the field is (i) not varied throughout the measurements and (ii) very small. The anisotropy flow concept under applied field is a useful framework if the magnetization direction is monitored depending on varying applied magnetic fields, while in the case of the present study a minor constant anisotropy offset could be taken into consideration. As the magnetic field from the objective lens is always oriented in the same direction along the optical axis, an imbalance in domains should be clearly visible at areas where K_2^{eff} has a zero-crossing. Histogram analysis from the SRT presented in Fig. 5.5 shows an almost balanced ratio of the two out-of-plane domains, not hinting to a sizable influence of the magnetic field.

CHOI et al. showed a strong dependence of the domain shape on the magnetic field direction with regard to the sample surface in the vicinity of the SRT [184]. While their study is built on the application of magnetic fields, all samples in the presented results have been demagnetized with a planar magnetic field conforming to Sect. 3.2.4. The decreasing field strength of the demagnetizing cycle should effectively reduce all effects

which are mentioned in the study by CHOI et al.

A puzzling issue could be found in films of thicknesses <10 ML. While previous publications report magnetic signals down to 4 ML $\text{Ni}/\text{Cu}(001)$, our films show a paramagnetic behavior. Surface roughness can be excluded as a reason, due to excellent preparation results shown by the characterization of the samples. Since studies on other magnetic films in our facility show similar behavior, we denote the effect to be instrument-related. However, no reasonable explanation could be found so far and leaves this matter as an open question.

5.2 $\text{Ni}_x\text{Pd}_{1-x}/\text{Cu}(001)$ in higher Pd concentration

In this second part, the influence of Pd on the driving mechanisms of the PMA and SRT will be investigated for higher Pd concentrations. At the beginning, a thickness wedged film in the area of compressive film strain, a regime where no effective anisotropy is expected to promote PMA, is presented. Secondly, a concentration-wedged film spanning the areas from tensile to compressive strain is subject to examination.

5.2.1 Thickness wedged $\text{Ni}_x\text{Pd}_{1-x}$



Figure 5.13 – Survey XMCD image of a 60 ML $\text{Ni}_{38}\text{Pd}_{62}$ wedge. The image shows film thicknesses from ~ 5 ML - 60 ML. Magnetic contrast in domains is in-plane, while on the left-hand image side the non-magnetic phase can be seen. An in-plane monodomain can be seen at the onset of the magnetic contrast.

$\text{Ni}_x\text{Pd}_{1-x}$ films exhibit a lattice mismatch with the substrate of $\text{Cu}(001)$ which is variable depending on the composition x . The adoption of the lattice constant of the substrate for the first ~ 15 Å of $\text{Ni}/\text{Cu}(001)$ has been described in Sect. 3.1.1, and gives rise to tensile film strain which decreases as misfit dislocations are included in the film. The results found in the previous sections are in good agreement with previous studies showing that the film stress and its relief are the driving parameters of the iSRT and the SRT in $\text{Ni}/\text{Cu}(001)$. The strain relief can also be achieved by expanding the lattice of film

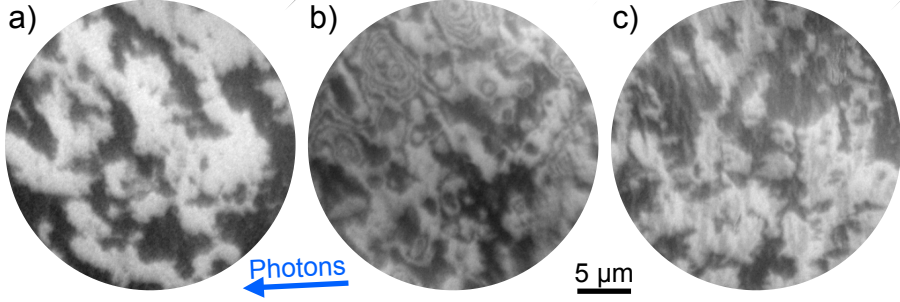


Figure 5.14 – Enlarged section of the domain pattern from the Ni₃₈Pd₆₂ sample presented in Fig. 5.13 (a), showing three different brightness levels for the in-plane magnetization. Domain patterns from Ni₄₂Pd₅₈ continuous film samples (b) & (c), 30 ML and 60 ML, respectively.

during growth: if alloyed with Pd, the lattice mismatch decreases, due to the increase of the Ni_xPd_{1-x} lattice constant according to relation 4.1 and a graphical representation in Fig. 4.5. With decreasing tensile strain, the strain-dependent terms in the anisotropy decrease, to a point where the anisotropy sum does not exhibit zero-crossings, hence no occurrence of the (i)SRT is expected.

Ni_xPd_{1-x} films were grown on Cu(001) with a Pd content above 25 %, to produce films exhibiting compressive strain. A survey image of a thickness wedged Ni₃₈Pd₆₂/Cu(001), which relates to a lattice constant of 3.74 Å and 3.7 % compressive strain, can be seen in Fig. 5.13. The paramagnetic phase on the left-hand image is followed by a short monodomain phase, as marked in the image. The domain structure evolving in succession does not reflect drastic variations in the film anisotropy since the variations in the domain pattern throughout the presented wedge film thickness between ~5 ML and 60 ML are only marginal. This is in good agreement with the assumptions made above - the strong changes in magnetic anisotropy found for Ni and Ni_xPd_{1-x}-films with tensile strain do not show up in Ni_xPd_{1-x} films with compressive strain.

While not very accentuated in the survey image, Fig. 5.14 a), an enlarged part of the wedge image shows three grey levels in the domain formation, connected the projection of a four-fold symmetric in-plane magnetization to the **k** of the incident photons. Fig. 5.14 b) & c), showing a 30 ML and 60 ML continuous film of Ni₄₂Pd₅₈, respectively, emphasize this behavior in an equilibrium geometry without wedge influence. When compared to the images from the wedged film, the continuous films show more detail in their domain structure, mostly owed to microscope alignment differences between the images: The setup used for a) was suited for survey imaging, while b) and c) were

5.2 $\text{Ni}_x\text{Pd}_{1-x}/\text{Cu}(001)$ in higher Pd concentration

dedicated to the respective images. Also image statistics, and azimuthal rotation of the sample with respect to the beam cannot be kept the same between two different samples. However, in terms of domain formation, the two compositions show similar behavior. No long range order or clear preference of domain geometry can be found. Domain sizes and pattern are of similar nature. This means that the stray field, saturation magnetization and anisotropy constants do not vary significantly in this composition region to change the general shape, but probably the details of the domain formation.

The clarification of magnetization direction shows that the films exhibit, in contrast to pure Ni films, in-plane anisotropy throughout the whole presented thickness range of $\sim 10\text{-}60$ ML. The strain-dependent terms in the compressive strain scenario are obviously not creating an effective positive magnetic anisotropy.

With the study presented in this section, the predictions made about the evolution of magnetic anisotropy when alloying Pd into Ni/Cu(001) are verified on $\text{Ni}_x\text{Pd}_{1-x}/\text{Cu}(001)$ films with a composition that exhibits compressive strain: Previously we have seen that in tensile strain Ni/Cu(001), the magnetic anisotropy gives rise to a perpendicularly magnetized area, which is relieved and eventually transitions to compressive strain by changing the lattice mismatch between NiPd and the substrate. The driving mechanisms of the PMA, strain dependent contributions to the anisotropy are also inverted in this process, resulting in the lack of the PMA. Even though this simple picture disregards additional influences, as the change in saturation magnetization and spin-orbit coupling strength, the grown $\text{Ni}_x\text{Pd}_{1-x}/\text{Cu}(001)$ films agree with this behavior and do not show a perpendicular magnetization in the thickness region of question, but only in-plane magnetization.

5.2.2 Composition wedged $\text{Ni}_x\text{Pd}_{1-x}$

In a geometry where the film stress or the amount of relaxation of film stress changes along the lateral dimension of a film, another transition through the magnetic phase diagram can be traced in a composition wedged experiment. In the previously presented case, stress related (surface) terms to the effective uniaxial anisotropy in Ni/Cu(001) pulled the magnetization out-of-plane. With further increasing thickness the effective anisotropy could be found to align parallel to the plane due to the relief of lattice strain. In the following section, the uniaxial anisotropy found in Ni films of 10-60 ML is reduced by relief of lateral stress resulting from Pd alloying into the film, effectively diminishing the stress-related terms by expansion of the lattice constant.

$\text{Ni}_x\text{Pd}_{1-x}/\text{Cu}(001)$ samples were grown in a wedged geometry with a lateral offset of the

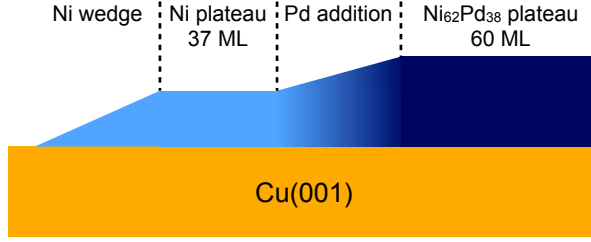


Figure 5.15 – A sketch of the composition/thickness wedged $\text{Ni}_{62}\text{Pd}_{38}/\text{Cu}(001)$ sample. The shadowing aperture is utilized to offset the two thickness wedges by about $200\text{ }\mu\text{m}$ from each other, resulting in a 37 ML Ni thickness wedge and an additional NiPd composition (0-38 % Pd)/thickness (37-60 ML) wedge. Both wedge profiles conform to Fig. 3.4. Since Ni/Cu(001) does not exhibit an SRT in the thickness range of 37-60 ML (see Sect. 5.1.1) the driving parameter a supposed SRT has to be composition-related. Hence, for the sake of simplicity, the wedge is titled 'composition-wedge' in the context of this thesis.

Ni- and Pd-wedges. A sketch of the film can be seen in Fig. 5.15. This design leads to an Ni thickness wedge and an additional $\text{Ni}_x\text{Pd}_{1-x}$ -wedge of constant Ni-amount with increasing Pd-content. It has to be taken into account, that the film thickness increases throughout this process by the amount of additional Pd. In the case of $\text{Ni}_{62}\text{Pd}_{38}$, presented in this section, the wedge relates to a starting thickness of about 37 ML Ni ranging up to 60 ML $\text{Ni}_{62}\text{Pd}_{38}$. Corresponding images of the domain formation can be seen in Fig. 5.16, along with Ni L_3 absorption images of the same region. The Ni L_3 photoemission yield can be used as a measure of Pd addition to the film due to the decrease of Ni content and hence signal. The Ni L_3 intensity images have each been taken as a sum from XAS σ^+ and σ^- absorption spectra peak images to eliminate magnetic contrast. Prior, the spectra are normalized to I_0 -current, measured from a gold grid between the refocussing optics of the beamline and the sample (see Sect. 3.2.3), yielding spectra which are free of beamline or electron storage-ring dependent flux variations. The average of pre-edge images from the spectrum is used to normalize the spectrum's images. This method takes account for beam asymmetries on the sample and background-effects., which results in a signal that is only given by the Ni absorption secondary emission partial yield. A linescan along the composition wedge's Ni L_3 signal displayed in the bottom panel of Fig. 5.16 shows the decrease of Ni L_3 signal.

On the left-hand side of the XMCD image, dark out-of-plane domains with widths between 500 nm and $3\text{ }\mu\text{m}$ can be seen enclosed by a bright domain.³ No significant change

³During survey scanning of the sample the wedge has been observed perpendicularly to the composition/thickness increase. The presented data were chosen as a representative of the general behavior of the sample.

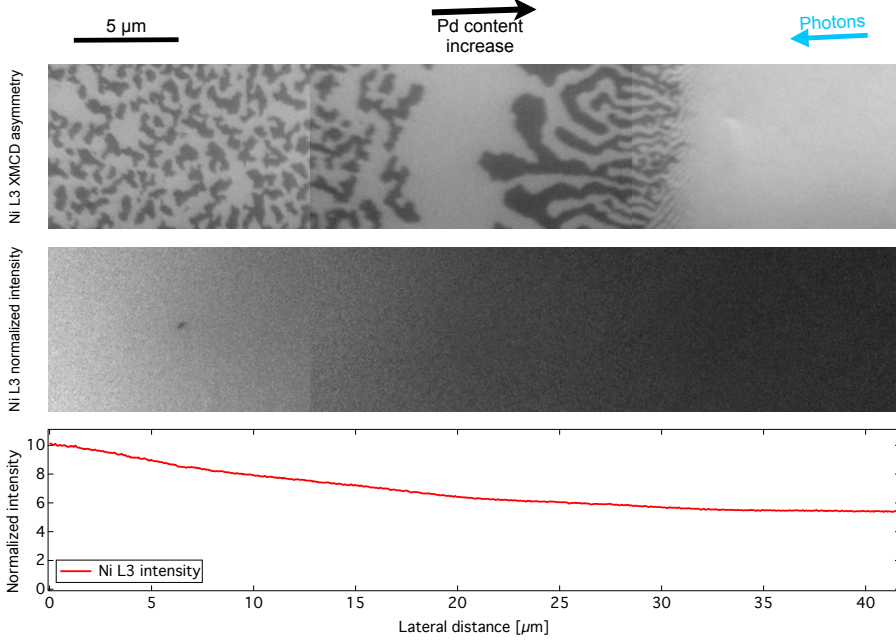


Figure 5.16 – Data from a composition wedged $\text{Ni}_{62}\text{Pd}_{38}/\text{Cu}(001)$ film. All images/plots show the same part of the sample, see marked regions. XMCD survey image displaying different magnetic phases and corresponding domain patterns (top). Corresponding Ni L₃ x-ray absorption intensity (middle). Linescan of 200px width along the horizontal of the absorption intensity data displayed in the middle, the decrease is a result of Pd addition to the film (bottom).

in domain size can be found, the Pd addition does not find any influence on the surface anisotropy. At a certain composition/thickness combination, almost no domains form and only the bright out-of-plane domain, i.e. the domain in which the magnetization vector points into the sample, can be found creating a monodomain-like state. With increasing Pd content, dark out-of-plane domains, i.e. domains in which the magnetization vector points out of the sample, develop again. They are larger in size and form a more equal balance in domain area between bright and dark domains than in the first phase (also see enlarged image detail in Fig. 5.17). The domain width decreases rapidly, starting at $3\text{ }\mu\text{m}$, introducing domain branching (the splitting of a domain into smaller parts along a certain direction) to satisfy the size reduction for both magnetization directions along the easy out-of-plane axis. The domain pattern is strongly influenced

by the wedge's slope elongation direction and would most probably be a labyrinth domain pattern in an equilibrium geometry. The branched domains eventually merge into a monodomain state. The enlarged image detail (Fig. 5.17) also reveals weak-contrast stripes at the boundary to the monodomain area, which proceed along a different angle not coinciding with the wedge geometry.

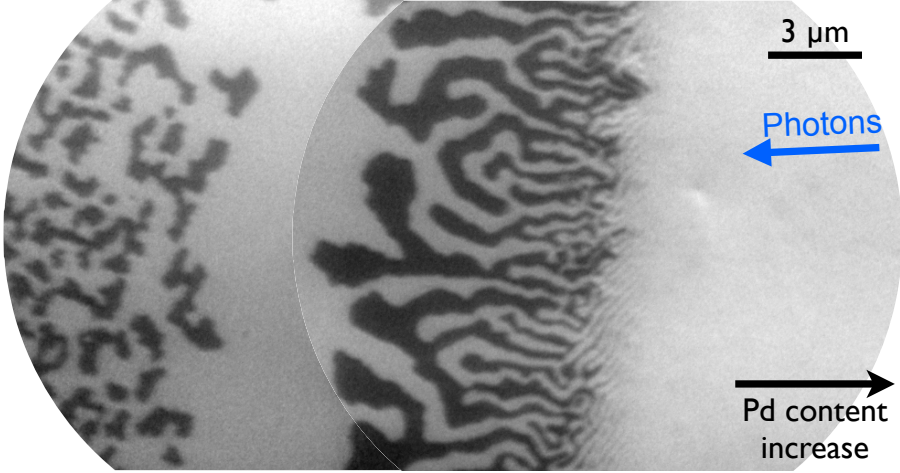


Figure 5.17 – SRT area of a $\text{Ni}_x\text{Pd}_{1-x}/\text{Cu}(001)$ composition wedge. The plateau area is 60 ML $\text{Ni}_{62}\text{Pd}_{38}$.

A rotation experiment reveals the nature of the magnetic contrasts: A sample rotation of about 30° has been employed for the XMCD image displayed in Fig. 5.18, creating a rotated geometry for in-plane magnetized areas due to the varied projection of the magnetization vector on the \mathbf{k} of the photons. A comparison of the contrast levels on the right-hand side of the image reveals an in-plane magnetized character of the monodomain. The contrast levels of the left-hand side of the image stay the same as in the previous sample rotation, conforming to out-of-plane rotation behavior.

An analysis from σ^+/σ^- x-ray absorption spectra underlines the proposed magnetization directions as shown in Fig. 5.20. The spectra are recorded as an image stack, enabling the possibility of microspectroscopy by choosing different regions of interest (ROIs) during spectra image stack evaluation (as shown schematically in Fig. 5.19). For that purpose, the spectra are normalized (i) to the photon flux determined by gold grid current I_0 and (ii) to the pre-edge image average, as previously described for the Ni L_3 intensity shown in Fig. 5.16. In order to calculate the XMCD spectrum from the images, domains

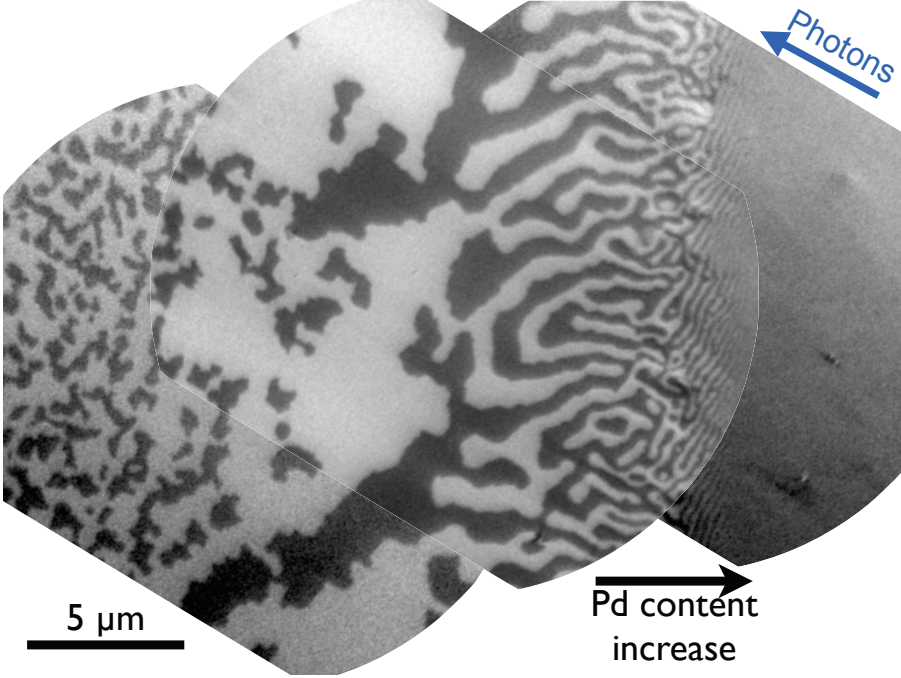


Figure 5.18 – SRT area of a $\text{Ni}_x\text{Pd}_{1-x}/\text{Cu}(001)$ composition wedge with photon incidence angle different from Fig. 5.17 by about 35° . The plateau area is 60 ML $\text{Ni}_{62}\text{Pd}_{38}$. Comparison to Fig. 5.17 shows an increase in XMCD contrast from 0 % to 15 % in the left-hand side of the image. The right-hand side of the image does not show a difference in contrast. Further information see text. XMCD contrast determined by XMCD spectra depicted in Fig. 5.20

of opposite magnetization are needed or the same domains in opposite light helicity (see Sect. 2.4). Hence, ROI A corresponds to data collected from ROIs on *bright* domains (on the XMCD image) from σ^+ *polarized* spectra and/or data collected from ROIs on *dark* domain (on the XMCD image) from σ^- *polarized* spectra. ROI B corresponds to the opposite domains at the same polarization. If oppositely magnetized domains are present, addition of the signals from ROIs of the same type helps to avoid errors from instrumental asymmetries in the setup, e.g. polarization rate and beam intensity decrease in synchrotron decay mode. This technique also helps to enhance statistics of the measurement. A background function can be fitted to pre- and postedge once the ROIs have been analyzed. Due to the preedge normalization, the spectra's preedge level is 1. From these spectra, the XMCD signal is calculated as the difference.

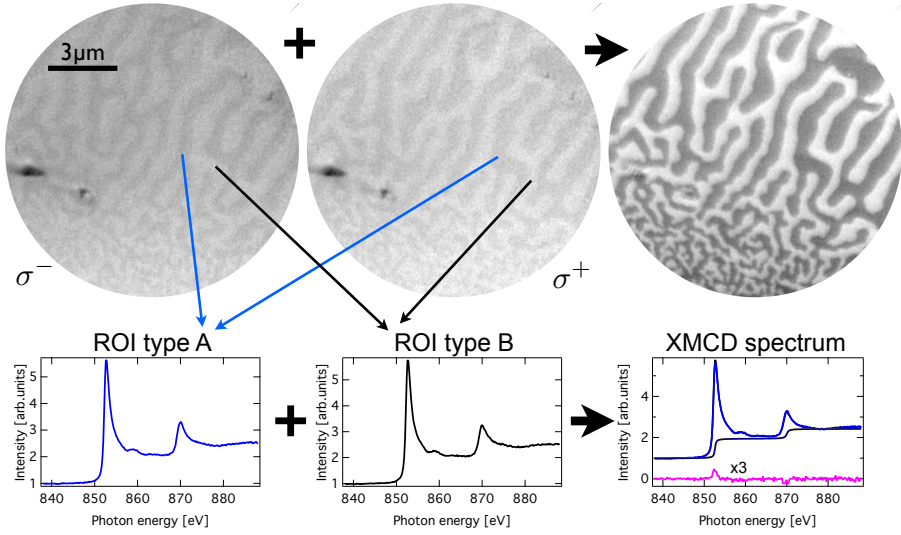


Figure 5.19 – Sketch on the procedure of XMCD micro-spectroscopy data evaluation in a uniaxial magnetization geometry. In the top left and middle two absorption average images are presented, already showing different electron yield from oppositely magnetized areas, due to the XMCD effect. These images are used to define regions of interest (ROIs) to extract the intensity spectra from a photon energy dependent image stack. The 'dark' ('bright') domains in each polarization (σ^+ , σ^-) spectrum are of the same geometrical relation regarding magnetization direction and photon propagation vector \mathbf{k} . Hence, the data from these regions are added as spectra from 'ROI type A' ('ROI type B'), to be seen in the bottom left and middle. The difference of these spectra yields the XMCD difference spectrum (bottom right). Additionally, top right shows the XMCD asymmetry image of the two average images from the absorption edge.

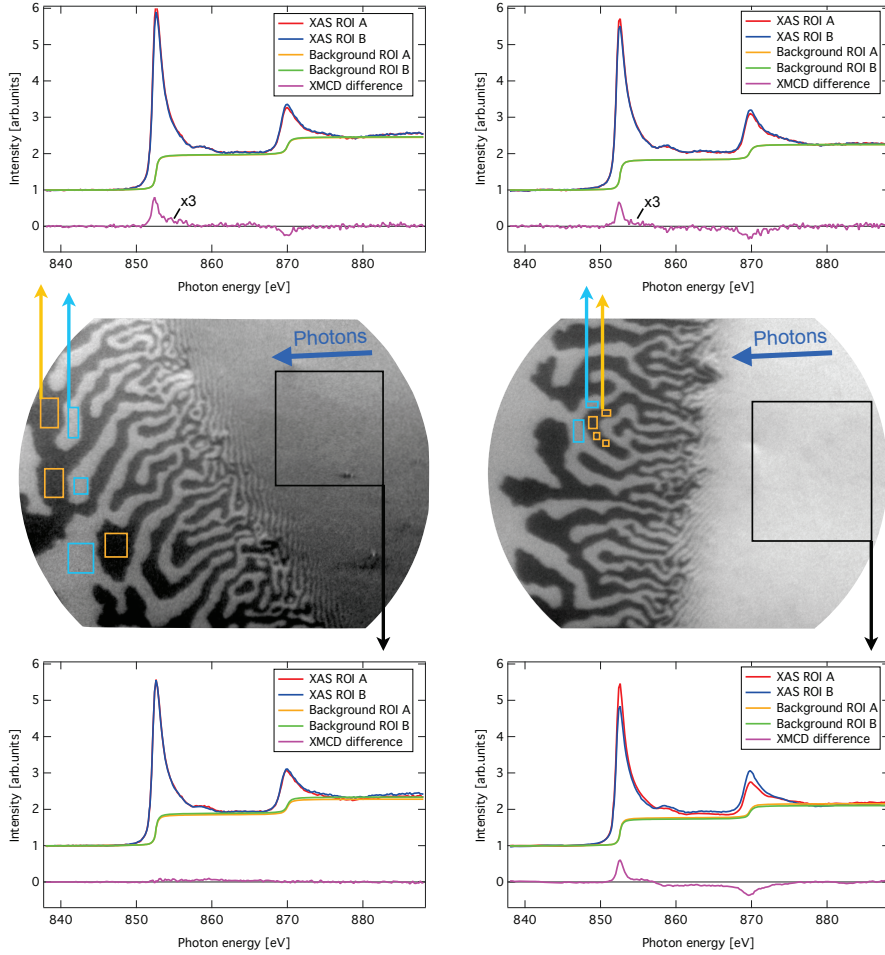


Figure 5.20 – XMCD absorption micro-spectroscopy in the vicinity of the SRT area. Rotation experiments (about 35°) from two measurement geometries are shown. XMCD images for the corresponding geometry shown in the middle row. XMCD spectra from the left-hand side of the images shown in top row, XMCD spectra from the right-hand side of the images shown in the bottom row. The selected areas are marked in the XMCD images. Evaluation process shown in text.

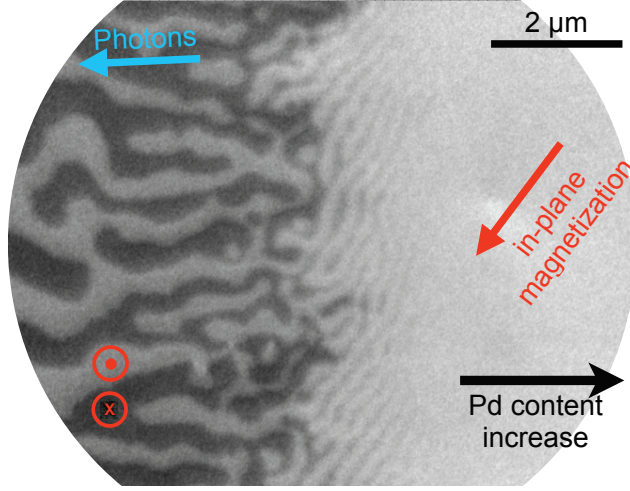


Figure 5.21 – Zoom into the SRT area of Fig. 5.17. Domain alignment and contrast loss instead of further domain branching throughout the SRT can be seen.

The spectra in Fig. 5.20 have been calculated using the ROIs marked in the XMCD images. Comparing the spectra, the difference in XMCD signal from the right-hand part of the images, corresponding to the lower plots, changes from negligible dichroism signal to about 15 % dichroism signal, resulting from a better alignment of the planar magnetic moments and the impinging photons due to sample rotation. Due to the vanishing XMCD contrast in the rotated image, the in-plane magnetization direction is suggested to be 90° to the photon direction of incidence in this image. The increase of XMCD contrast (under angular variation of about 35°) to about 15 % of the signal agrees to typical saturated XMCD contrasts of 25 % [113, 198].

The XMCD contrast in the labyrinth-like pattern is almost the same in both rotations of the sample, which is expected for perpendicular magnetization, whose projection onto the \mathbf{k} of incident photons does not change upon azimuthal rotation.

With an established knowledge about the SRT in the system at hand, details of the SRT area will be discussed in the following. A magnified part of the SRT area can be seen in Fig. 5.21. In this magnification the kink in domain orientation is much more pronounced. While the perpendicularly magnetized domains on the left-hand side of the image follow a direction dictated by the slope of the composition/thickness wedge, the delicate domains in the SRT area follow a direction tilted by about 45° . Notably, the contrast levels in these domains is overall brighter than in the perpendicular part, while still being

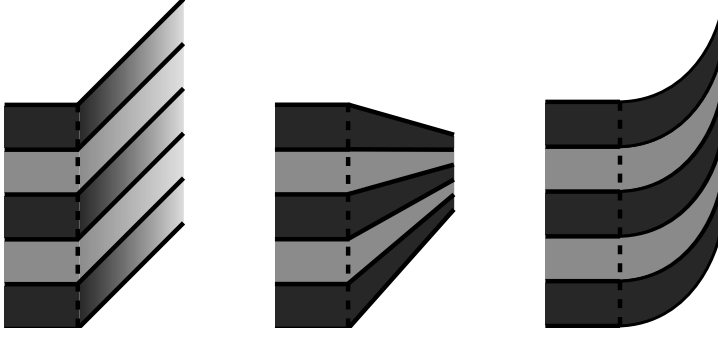
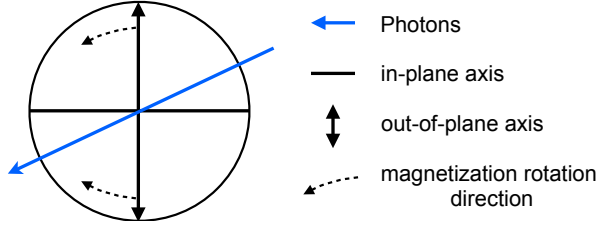


Figure 5.22 – Sketch of the domains in the SRT area. (a) The domain contrast fades in each particular domain. (b) Contrast is lost due to domain size reduction. Without domain branching, no equilibrium can exist, since all domains would need to meet in a single point of the sample. (c) Same as b), but with constantly changing domain wall orientation, creating an equilibrium state without branching. If compared to Fig. 5.21, b) and c) can easily be excluded for the data found in the experiment.

connected to the dark and bright domains given from the perpendicularly magnetized area. The fading of these domains happens via a loss of contrast, not a decrease in domain size beyond resolution, which would require further domain branching (see also Fig. 5.22 for a sketch of SRT contrast change). The loss in contrast is connected to a continuous canting of the magnetization vector, (i) marking a second order SRT and (ii) being a completely different magnetic manifestation of the canted SRT (continuous contrast fading) compared to the manifestation found in the thickness wedged $\text{Ni}/\text{Cu}(001)$ in Sect. 5.1.1 (rectangular domains superposed by cloud-like in-plane contributions).

Since the canting is a continuous process, the amount of perpendicular magnetization in the SRT-domains decreases continuously over the length of $\sim 2\ \mu\text{m}$. The dark domains are almost always connected to the dark domains in the perpendicular part, suggesting that the contrast of the SRT-domains in fact is of perpendicular nature. However, both domains are canting in the same direction towards the monodomain in-plane magnetization preference. This magnetization rotation in relation to the photon incidence is sketched in Fig. 5.23. In this frame, it is reasonable that the bright SRT domains reach the contrast level of the in-plane domain already once on their rotation way, which may be perceived as 'earlier' than the dark SRT domains. This is reasoned by the photon inclination angle of 25° , which makes the bright out-of-plane domains, oriented along the perpendicular axis with the \mathbf{k} of photons, pass the 'perfect alignment' with the \mathbf{k} , while the dark domains will not. This in fact means that the bright domains of the

Figure 5.23 – A sketch of the magnetization rotation paths in relation to the photon incidence direction. The 'down' domain passes the photon incidence direction, while the 'up' domain does not.



perpendicularly magnetized area should initially get brighter than the in-plane-domain, which can be seen in some areas large enough to be free from the influence of neighboring domains.

The reason for the domain alignment deviation from the wedge direction in the SRT area cannot be answered by these measurements. It is most likely that in-plane anisotropies align the domains with easy axes of the in-plane magnetization as could be seen for the rectangularly aligned phase in Ni/Cu(001). Tilting as a result of domain size reduction can be excluded since the domains' alignment is straight throughout the narrow region they exist, while they would be subject of a constant bending process to compensate for a constant domain size reduction (also see Fig. 5.23).

In the framework of micromagnetic calculations The development of the film presented in this section takes a different path through the magnetic phase diagram calculated in the framework of the micromagnetic simulations discussed in Sect. 5.1.1. The composition wedged films path through the phase diagram coincides with the path of the previously discussed wedged Ni film, since there is no Pd content in the film up to 37 ML thickness. The composition wedge alters the uniaxial anisotropy in a way that can be compared to the thickness wedged Ni film. While the strain relaxation might be of close resemblance, increased spin-orbit coupling from the Pd atoms and varied relative values of strain-independent anisotropy terms with respect to the strain-dependent ones have to be taken into account.

Close to the SRT we find a monodomain-like phase and a labyrinth domain pattern, which is a transition including higher disorder. Upon entering the SRT, the disorder is reduced again by forming a stripe geometry. The path of our system through the phase diagram created by simulated by CARUBELLI et al. [190] (see Fig. 5.9) starts in the paramagnetic phase. Since the uniaxial anisotropy is highest in the pure Ni film, the domain phase is entered by reduction of T due to film thickness increase, and increase of the uniaxial anisotropy parameter. This results in the same 'maximum' of the path

as for the pure Ni film. By alloying Pd into the Ni film, the effective temperature will not change much since (i) T_c of $\text{Ni}_x\text{Pd}_{1-x}$ films only decreases moderately with x , because the magnetic moment, which is easily induced in the Pd atoms, since Pd is almost magnetic by itself as can be seen by the STONER criterion (see Sect. 2.1.1). Bulk T_c for $\text{Ni}_{60}\text{Pd}_{40}$ drops from 700K to $\sim 550\text{K}$ [199]. (ii) With an increase of film thickness, T_c effectively raises [56]. While the film thickness in the sample at hand is changing from 37 to 60 ML, we do not anticipate grave effects from this source, since the pure Ni film does not show its SRT in this thickness range (see Sect. 5.1.1). Yet, without experiments on this behalf it is not known which of the two effects dominates the other. The path through the phase diagram will therefore mainly be determined by the decrease in the uniaxial anisotropy, by the relaxation of lattice strain, mediated through the strain-dependent terms in Eqn. 2.22. It is most likely that the film does not cross the SRT border at the same point in the phase diagram as the pure Ni film due to a different balance between uniaxial anisotropy and T_c . Since all phases described in the diagram by CARUBELLI et al. [190] and also by Abanov et al. [33] can be found in the described SRT, the paths cannot be too far apart, though. These findings emphasize that even though the pathways through the phase diagram are technically not that different, the exhibited domain structure is strongly dependent on the point where the SRT border is crossed and most likely subject to other influences, as the exhibition of in-plane anisotropies.

5.2.3 Summary $\text{Ni}_x\text{Pd}_{1-x}$ films with higher Pd concentration

In the previous section $\text{Ni}_x\text{Pd}_{1-x}$ films with higher Pd concentration have been investigated. Thickness wedged $\text{Ni}_x\text{Pd}_{1-x}$ films were found to behave according to theoretical considerations. $\text{Ni}_x\text{Pd}_{1-x}$ films with $x > \sim 25\%$ exhibit compressive stress instead of tensile stress due to the inverted relation of film and substrate lattice constants. While the corresponding magnetoelastic terms in $\text{Ni}/\text{Cu}(001)$ and Ni-like $\text{Ni}_x\text{Pd}_{1-x}/\text{Cu}(001)$ are responsible for the perpendicular magnetic anisotropy over a wide range of film thickness, the inversion of lattice stress removes this driving parameter. Experimental results on wedged $\text{Ni}_{38}\text{Pd}_{62}$ and continuous film $\text{Ni}_{42}\text{Pd}_{58}$ show only in-plane magnetization up to 60 ML film thickness, confirming these theoretical considerations.

In order to find a different geometry for SRTs in $\text{Ni}_x\text{Pd}_{1-x}$ alloys, composition wedged $\text{Ni}_x\text{Pd}_{1-x}$ alloys were grown on $\text{Cu}(001)$. As the lattice stress is relieved with lateral distance, an SRT could be seen depending on the Pd content. The manifestation of domain formation in this film does not resemble the one found for Ni films earlier. No

hints of a rectangularly ordered pattern could be found, but a complex interplay of domain patterns featuring unordered, labyrinth, stripe and monodomain states ranging in domain width between 200 nm and 3 μ m. The observed magnetization phases are in good agreement with the theoretical studies and simulations presented earlier. It is worth noting that the magnetic phases manifest in a completely different way regardless of the films close relation and similarity in phase transition, including domain size reduction and influence of an in-plane anisotropy. Varied properties are the amount of spin-orbit coupling in the film (given by the higher spin-orbit coupling of Pd), the effective uniaxial anisotropy and T/T_c , and the relation between strain-dependent and strain-independent anisotropies.

5.3 Domain patterns close to vanishing lattice mismatch

As discussed in the previous sections, the origin of the (i)SRT in Ni/Cu(001) found strain-dependent anisotropy terms as the driving influence (see Sect. 2.1.3). By alloying Pd into the Ni, the lattice mismatch is reduced, which results in a reduction of the strain-dependent anisotropy terms. At a perfect lattice mismatch, occurring at about 25% Pd content (see Sect. 4.3.2), it is obvious that all the (i)SRT driving mechanisms have completely vanished. The strain-dependent terms of the anisotropy will constantly decrease with increasing Pd content, resulting in a shift of the (i)SRT thickness, as shown for the iSRT in Ni_xPd_{1-x}/Cu₃Au(001) [200, 201]. It has to be noted, that this simple view does not include additional effects from the alloying, such as variations to the average spin-orbit coupling, T_c , and strain-independent anisotropy constants. However, for the sake of clarity, their influence will be neglected in the context of this discussion. In the frame of the calculations presented in Fig. 2.7 and in agreement with the results from the cited studies, the effective uniaxial anisotropy constant will decrease, and at some point, resulting from the interplay of negative strain-dependent surface term and the positive strain-dependent magnetoelastic term, shift the zero-crossings towards each other. Arguably, the effective uniaxial anisotropy, i.e. the sum of all contributions, will not linearly decrease, but find a decrease of the slope inclination. This is reasoned by the strain dependent anisotropy terms, which partially cancel each other out (see Sect. 2.2 and Fig. 2.7). The resulting shift in zero crossings therefore will not proceed linear with Pd content. The first proof of a non-linear zero-crossing shift with composition can be seen in the wedged 60 ML Ni₈₈Pd₁₂/Cu(001) presented in Sect. 5.1.2. Incorporating half the amount of Pd needed to create an all in-plane magnetized film, the film did not show an SRT up to plateau thickness. Hence, an SRT thickness/zero crossing shift of less than

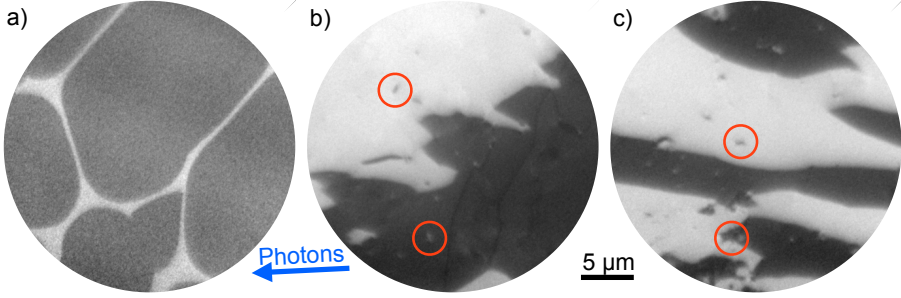


Figure 5.24 – XMCD images of a $\text{Ni}_{80}\text{Pd}_{20}/\text{Cu}(001)$ film with varying thickness: 15 ML (a), 30 ML (b), 60 ML (c). The stoichiometry results in a lattice mismatch of 0.5 %. The strain related anisotropy terms become less influential, hence the 30 and 60 ML films are magnetized in-plane, while the 15 ML film is magnetized out-of-plane. The thickness area of the PMA is reduced in agreement with the anisotropy model introduced in Sect. 2.2.

5 ML for mixing 12% Pd into the Ni film is an additional result from the data obtained in this thesis. In the following section we want to show a simple example for the shift of the SRT to lower film thicknesses due to a Pd content close to the composition of vanishing lattice mismatch.

5.3.1 Continuous films in the vicinity of vanishing lattice mismatch

The wedged $\text{Ni}_x\text{Pd}_{1-x}$ films of Pd concentration up to 12 % presented in Sect 5.1.2 did not show a shift of the SRT thickness under 60 ML. $\text{Ni}_{80}\text{Pd}_{20}/\text{Cu}(001)$ continuous films of 15 ML, 30 ML and 60 ML were grown to approach the vanishing lattice mismatch for magnetic imaging. XMCD images of the domain formation of these films can be found in Fig. 5.24.

In these images an out-of-plane magnetic domain pattern for the 15 ML film can be seen. The pattern is mostly comprised from dark domains, i.e. tending towards a dark monodomain. Bright domains can only sparsely be found. The shape of the domains falls in the bubble domain regime, resembling the domain formation of the 30 ML $\text{Ni}_{93}\text{Pd}_{07}/\text{Cu}(001)$ film presented in Fig. 5.10 c). The extended thickness range of this domain pattern can be understood in connection to the decrease of the strain-dependent anisotropy terms. A varied amount of magnetostatic anisotropy also has to be kept in mind. However, as can be seen from the results on the Ni/Cu(001) wedge, the areas of similar magnetic behavior in terms of domain patterns are extended over a fair thickness range. The imbalance of domains may be attributed to the influence of the weak magnetic field ($<1 \mu\text{m}$) of the objective lens. This in turn means, that the observed state

has a low coercivity to allow for this imbalance.

The 30 ML and 60 ML films show an almost identical domain pattern, with 4 separable brightness values due to a four-fold in-plane magnetic anisotropy and an ideal geometrical alignment to the photon impinging direction.

The phase diagram path of the composition wedged NiPd film discussed in Sect. 5.2.2 has to cross the phase diagram path connecting the 30 ML and 60 ML films presented in this section. While the composition wedge does not create any domain pattern in the in-plane magnetized area, the continuous films presented here show an in-plane domain pattern. Due to the similarity in domain formation of both continuous films, we do not believe a monodomain in-plane phase would exist between the two selected thicknesses. We attribute the single domain formation in the composition wedged film to a spontaneous minimum of the free energy found for in this specific film or a contribution from the non-equilibrium geometry of the wedged film. On the other hand, we could imagine local topography to influence the domain formation in the continuous films by a modulation of the stray field. Such influence can be seen most easily as small dark domains on the bright domains [as marked in Fig. 5.24 c)].

In this section we confirmed a shift of the SRT in Ni₈₀Pd₂₀/Cu(001) to a film thickness between 15 ML and 30 ML. The domain formations in each regime could be connected to the domain formation in 30 ML Ni₉₃Pd₀₇/Cu(001) and the composition wedged 60 ML Ni₁₀₀->Ni₆₃Pd₃₇/Cu(001), respectively, and the phenomenological single-domain anisotropy treatment of thin films.

5.4 T_c drop at the spin-reorientation transition

An often reported feature of SRTs is a drop of T_c at the thickness or temperature connected to the SRT. Most notable studies report on a loss of magnetic contrast or signal for Fe/Ni/Cu(001) [184, 186], Ni/Cu(001) at the iSRT [174], Ni_xPd_{1-x}/Cu₃Au(001) at the iSRT [66, 201], and Co/Au(111) [81]. Contrary to these findings, a continuous transition has been reported for the SRTs in studies on Ni/Cu₃Au(001) at the iSRT without drop of T_c [202].

The images presenting SRTs at room temperature in the previous sections show a transition of continuous nature without loss of contrast (see Figs. 5.3, 5.21). Additional SRTs are presented in this section, documenting further reorientation behavior of magnetic films at room temperature. The XMCD image seen in Fig. 5.25 a) shows the iSRT in a Ni₈₅Pd₁₅/Cu(001) film. No loss of contrast at the iSRT thickness can be found. The domain pattern transits from a cloudlike in-plane pattern with diffuse domain boundaries

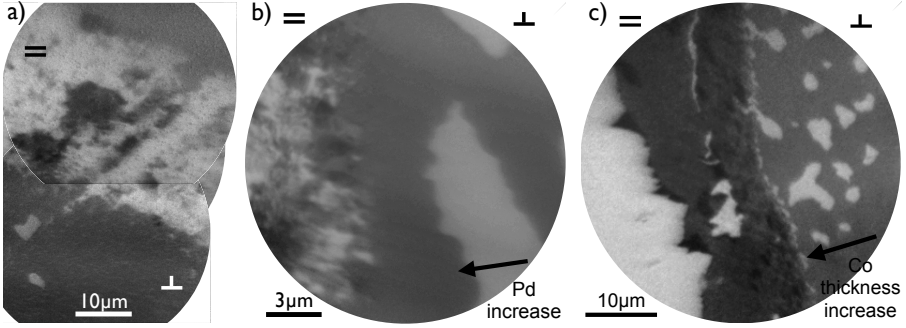


Figure 5.25 – XMCD images at the Ni L_3 edge. (a) $\text{Ni}_{85}\text{Pd}_{15}/\text{Cu}(001)$ at thicknesses between 8 ML and 14 ML. The paramagnetic phase can be seen at the top of the image, followed by an in-plane phase transiting to a nearly domainless out-of-plane phase. (b) A composition/thickness wedged 15 ML $\text{Ni}_{82}\text{Pd}_{18}/\text{Cu}(001)$ (plateau) film exhibiting an SRT from out-of-plane to in-plane due to Pd content increase. (c) An SRT driven by exchange coupling in a $\text{Ni}/\text{Co}/\text{Cu}(001)$ film due to increasing thickness of the buried Co layer. The strong Co in-plane anisotropy forces the magnetic moments of the Ni film to conform at a certain thickness.

to a typical out-of-plane domain pattern without showing a zone of contrast loss.

A composition wedged iSRT in $\text{Ni}_x\text{Pd}_{1-x}/\text{Cu}(001)$ is displayed in Fig. 5.25 b). At the plateau composition, the film is 15 ML $\text{Ni}_{82}\text{Pd}_{18}$. With the increase of Pd content, the system transits from an out-of-plane Ni-like NiPd film of about 12 ML to an in-plane NiPd film of 15 ML and 18% Pd content. While there is not enough information on this transition to see whether it is of first or second order, it clearly does not exhibit a zone without magnetic contrast throughout the iSRT.

A sample of wedged $\text{Ni}(15 \text{ ML})/\text{Co}(15 \text{ ML})/\text{Cu}(001)$, created to image a different type of SRT, is shown in Fig. 5.25 c). The wedges of Ni and Co have been rotated by 45° with respect to each other. The image shows an area of constant Ni thickness, but wedged Co. The image has been obtained at the Ni L_3 edge, showing magnetic contrast from the Ni magnetic moment. While the 15 ML film by its own has a perpendicular magnetic anisotropy (as shown in previous sections), the Co has a strong in-plane anisotropy. The magnetic coupling strength from the underlying Co increases with Co thickness until the Ni magnetic moments conform to the in-plane direction, mediated via exchange coupling. Within the limits of the resolution of the present image (defined by the chosen field of view - $\approx 60 \text{ nm}$) the SRT proceeds without a loss of magnetic contrast.

The three additional SRTs presented in Fig. 5.25 do not show any hint for a loss of magnetic order during the realignment of magnetic moments. These findings underline

the argument deduced from the SRTs presented in the previous sections of this thesis, see Fig. 5.3 and Fig. 5.21. With a loss of magnetic order found for the same system of Ni/Cu(001) and comparable systems Ni/Cu₃Au(001) & Ni_xPd_{1-x}/Cu₃Au(001), all measured under applied field in a single domain method. While unlikely, it is possible that the typically small domains at the SRT are of higher stability, withstanding the single-domain creating magnetic fields from the respective studies. This would also be in agreement with the decreased influence of surface roughness on the size of domains at the SRT, reported by CHOI et al. [184].

This argument would agree with the results from studies that experienced a T_c drop. Lateral averaging of areas bigger than the domain size results in a perceived non-magnetic sample and an apparent T_c drop. The behavior of the magnetic domains in the SRT area under the influence of an external magnetic field in a microscopic setup hence would be an interesting experiment, able to provide further knowledge about the origin of the T_c drop.

6 Summary and outlook

The thesis aimed at giving the first comprehensive PEEM study on the domain formation in a perpendicular magnetic anisotropy (PMA) system exhibiting a spin-reorientation transition (SRT) covering the the thickness range continuously in a wedged geometry. The domain formations were described in connection to the evolution of the uniaxial anisotropy K_2^{eff} . While most sample systems exhibit the PMA only in a narrow thickness range of about 1-5 ML, Ni/Cu(001) offers an extended range of about 7-70 ML and offers a tunable strain influence to the magnetic anisotropy by alloying with Pd.

Samples for analyzation with aberration corrected x-ray photoemission microscopy (XPEEM) have been grown epitaxially in wedged and continuous film geometry up to 100 ML thickness. Synchrotron radiation provided at the Forschungszentrum Jülich beamline UE56/1-SGM at BESSY II, Germany, Berlin has been utilized to employ x-ray circular dichroism (XMCD) as the magnetic contrast mechanism, offering chemical selectivity, as a multi-purpose tool to additionally determine film thickness- and composition-gradients.

Microscopic images along the wedged Ni-like and $\text{Ni}_x\text{Pd}_{1-x}/\text{Cu}(001)$ films showing varying magnetic contrast with thickness were presented in the first part of the experimental results. The magnetic phases, categorized by their distinctive changes in domain pattern, find a good agreement with previous studies on the uniaxial anisotropy properties, which were measured under applied field. The naturally preferred state of the demagnetized films found for Ni/Cu(001) are (i) paramagnetic phase, (ii) out-of-plane monodomain-like phase from 10 ML up to 35 ML, (iii) out-of-plane magnetized phase consisting of elongated domains with rectangular alignment between domain walls up to 65 ML, (iv) canted state SRT phase. A distinctive domain-wall arrangement along the $\langle 110 \rangle$ -axes forming a rectangular pattern is introduced in phase (iii), attributed to the decrease of the uniaxial anisotropy K_2^{eff} , allowing in-plane anisotropies to influence the in-plane part of the domain walls. The SRT phase at moderate thicknesses of 65 ML for our Ni/Cu(001) films marks its first microscopic observation, including the domain-state equivalent to the single-domain canted state. This transition area is characterized by a breakdown of the domain size in the rectangularly aligned pattern, prevailing in a su-

6 Summary and outlook

perposition with what we call a cloud-like domain pattern. We attribute the increasing density and contrast strength of the cloud-like domains to an increased canting of the magnetization angle, in agreement with the creation of XMCD contrast.

A comparison to Monte Carlo simulations from publications of the recent past revealed a formidable consistency with the domain phases found in our experiment. The rectangularly ordered domain formation hence can be explained as a textbook example of the so-called tetragonal liquid phase, showing a unique path of the phase transition of the magnetic system through the phase diagram of uniaxial anisotropy vs. temperature simulated by CARUBELLI et al. closely to the triple point.

Ni-like sample of $\text{Ni}_x\text{Pd}_{1-x}/\text{Cu}(001)$ showed consistent results with the findings from $\text{Ni}/\text{Cu}(001)$ in terms of domain formation. A topographic contrast along the $\langle 110 \rangle$ -axes could be found in some 60 ML films by LEEM experiments, which in agreement to previous study are most likely connected to the formation of misfit dislocations. However, is not considered to be the driving mechanism. Even though a decrease of lattice strain is connected to a decrease of the strain-dependent anisotropy contributions no noticeable shift of the SRT could be found. In combination with $\text{Ni}_x\text{Pd}_{1-x}$ films of concentrations closer to vanishing lattice mismatch, finding an eminent decrease in thickness for the in-plane magnetized phase, we attribute the strain-decrease to influence the strain-dependent terms of K_2^{eff} canceling each other out in the first instance, resulting in an nonlinear change of SRT thickness with increasing Pd content.

The rectangularly aligned domain pattern was analyzed in $\text{Ni}_{88}\text{Pd}_{12}$ by fitting a theoretical description of the magnetization rotation to the magnetic contrast obtained from XMCD image linescans. The screw-like rotation along the $\langle 100 \rangle$ -axes cannot be explained with the data from this study, however, we could understand the behavior if the sample thickness and the influence of in-plane anisotropies was to induce the change from NÉEL-type to BLOCH-type walls.

In agreement to theoretical considerations and the results obtained from the decrease of the SRT thickness in $\text{Ni}_x\text{Pd}_{1-x}$, wedged $\text{Ni}_x\text{Pd}_{1-x}/\text{Cu}(001)$ films of Pd content in the range of compressive strain show only in-plane magnetization throughout the grown thickness range up to 60 ML. This underlines the validity of the stress-related anisotropy contributions, effectively acting as an additional in-plane bias in compressively strained $\text{Ni}_x\text{Pd}_{1-x}$ films.

The thesis shows the first study on a composition-wedged $\text{Ni}_x\text{Pd}_{1-x}/\text{Cu}(001)$ exhibiting an SRT at moderate sample thicknesses. Microscopically, the vicinity of the SRT is again accompanied by a vigorous change in domain formation. Monodomain-like phase and labyrinth phase could be found in the out-of plane regime, while the in-plane area

is governed by a monodomain phase. The SRT itself is determined to be proceeding via a canted state. In this sample geometry the canted state rotation is performed by a completely different domain arrangement, characterized by stripes of fading contrast. In-plane anisotropy contributions could be found at the SRT, tilting this striped domain arrangement away from the typical wedge inclination direction.

In the last part of this thesis, the observed SRTs were analyzed with respect to the frequently reported T_c drop at the reorientation. However, no evidence for the existence was found, including an iSRT in $\text{Ni}_x\text{Pd}_{1-x}$ films and $\text{Ni}/\text{Co}/\text{Cu}(001)$ films. A detailed comparison with measurements in applied field would be necessary to explain the occurrence of the observed T_c -drops.

Future experiments and investigations would highly profit from direct comparison of in-situ and ex-situ produced samples. Complementing the microscopic analysis of domains with the exact determination of anisotropy constants would yield a direct connection between domain formation and the anisotropy constants. Considerable work towards a portable system has been done in the frame of this thesis by development of a $\text{Cu}(001)/\text{Ag}/\text{Fe}/\text{GaAs}(001)$ film system as a high-quality substitute for $\text{Cu}(001)$ single crystals [203]. In comparison to the $\text{Cu}(001)/\text{Si}$ system frequently used for Ni films, an average roughness improvement of about an order of magnitude could be achieved. Film deposition on these artificial $\text{Cu}(001)$ single crystals would enable a direct comparison between the existing results on capped systems and the Cu single crystal results made in this study.

In order to observe the influence of growth to the magnetic formation of domains, evaporation during PEEM/LEEM examination would also broaden the understanding of domain formation in epitaxially grown films. In the frame of domain observations the behavior of the SRT with respect to temperature would be of great interest due to the temperature dependent anisotropy contributions.

With the unique results presented in this thesis, we find $\text{Ni}/\text{Cu}(001)$ and $\text{Ni}_x\text{Pd}_{1-x}/\text{Cu}(001)$ to be a model system for spin reorientations of various manifestations on the microscopic level. While a good agreement with previous studies and theory is found, further investigation of the systems promise a deeper understanding of the microscopic mechanisms governing the SRT. This $\text{Ni}/\text{Cu}(001)$ and $\text{Ni}_x\text{Pd}_{1-x}/\text{Cu}(001)$ study presented magnetic behavior yielding deeper insight to the demagnetized SRT in its magnetic ground state and domain preferences in the SRTs vicinity. In the course of this thesis a variety of intrinsic domain formations and magnetization preferences were found, which underline the diversity of spintronics and the possible properties of materials to be tailored for technological application.

6 *Summary and outlook*

Bibliography

- [1] Top500.org Poster November 2012, http://s.top500.org/static/lists/2012/11/TOP500_201211_Poster.pdf, Accessed: 2014-07-10.
- [2] Apple system on a chip, http://en.wikipedia.org/wiki/Apple_system_on_a_chip, Accessed: 2014-07-10.
- [3] S. A. Wolf et al., *Spintronics: A Spin-Based Electronics Vision for the Future*, Science **294**, 1488 (2001).
- [4] C. M. Schneider, *Spintronics - Introduction*, volume 40 of *Spring School Lecture Notes*, chapter II, Forschungszentrum Jülich GmbH, 2009.
- [5] W. Thomson, *On the electro-dynamic qualities of metals:—effects of magnetization on the electric conductivity of nickel and of iron*, Proceedings of the Royal Society of London **8**, 546 (1856).
- [6] J. C. Maxwell, *A treatise on electricity and magnetism*, volume 1, Clarendon press, 1881.
- [7] P. A. Dirac, *The quantum theory of the electron*, Proceedings of the Royal Society of London. Series A, Containing Papers of a Mathematical and Physical Character , 610 (1928).
- [8] E. C. Stoner, *Collective electron ferromagnetism*, Proceedings of the Royal Society of London. Series A, Mathematical and Physical Sciences , 372 (1938).
- [9] I. Campbell and A. Fert, *Transport properties of ferromagnets*, Ferromagnetic materials **3**, 747 (1982).
- [10] P. Grünberg, R. Schreiber, Y. Pang, M. B. Brodsky, and H. Sowers, *Layered Magnetic Structures: Evidence for Antiferromagnetic Coupling of Fe Layers across Cr Interlayers*, Phys. Rev. Lett. **57**, 2442 (1986).

Bibliography

- [11] M. N. Baibich et al., *Giant Magnetoresistance of (001)Fe/(001)Cr Magnetic Superlattices*, Phys. Rev. Lett. **61**, 2472 (1988).
- [12] G. Binasch, P. Grünberg, F. Saurenbach, and W. Zinn, *Enhanced magnetoresistance in layered magnetic structures with antiferromagnetic interlayer exchange*, Phys. Rev. B **39**, 4828 (1989).
- [13] A. Berger, *Spintronics - Technology of Hard Disk Drives*, volume 40 of *Spring School Lecture Notes*, chapter F1, Forschungszentrum Jülich GmbH, 2009.
- [14] M. Julliere, *Tunneling between ferromagnetic films*, Physics Letters A **54**, 225 (1975).
- [15] E. F. Kneller and F. E. Luborsky, *Particle Size Dependence of Coercivity and Remanence of Single-Domain Particles*, Journal of Applied Physics **34**, 656 (1963).
- [16] C. Chappert, A. Fert, and F. N. Van Dau, *The emergence of spin electronics in data storage*, Nat Mater **6**, 813 (2007).
- [17] M. Kryder et al., *Heat Assisted Magnetic Recording*, Proceedings of the IEEE **96**, 1810 (2008).
- [18] W. Gallagher and S. Parkin, *Development of the magnetic tunnel junction MRAM at IBM: From first junctions to a 16-Mb MRAM demonstrator chip*, IBM Journal of Research and Development **50**, 5 (2006).
- [19] S. S. P. Parkin, M. Hayashi, and L. Thomas, *Magnetic Domain-Wall Racetrack Memory*, Science **320**, 190 (2008).
- [20] R. Jansen, *The spin-valve transistor: a review and outlook*, Journal of Physics D: Applied Physics **36**, R289 (2003).
- [21] D. A. Allwood et al., *Magnetic Domain-Wall Logic*, Science **309**, 1688 (2005).
- [22] U. Gradmann, *Ferromagnetism near surfaces and in thin films*, Applied physics **3**, 161 (1974).
- [23] C. Chappert, D. Renard, P. Beauvillain, J. Renard, and J. Seiden, *Ferromagnetism of very thin films of nickel and cobalt*, Journal of Magnetism and Magnetic Materials **54 - 57, Part 2**, 795 (1986).
- [24] D. Pescia et al., *Magnetism of Epitaxial fcc Iron Films on Cu(001) Investigated by Spin-Polarized Photoelectron Emission*, Phys. Rev. Lett. **58**, 2126 (1987).

- [25] R. Allenspach, M. Stampanoni, and A. Bischof, *Magnetic domains in thin epitaxial Co/Au(111) films*, Phys. Rev. Lett. **65**, 3344 (1990).
- [26] A. Moschel and K. D. Usadel, *Reorientation transitions of first and second order in thin ferromagnetic films*, Phys. Rev. B **51**, 16111 (1995).
- [27] H. P. Oepen, M. Speckmann, Y. Millev, and J. Kirschner, *Unified approach to thickness-driven magnetic reorientation transitions*, Phys. Rev. B **55**, 2752 (1997).
- [28] Y. Millev and J. Kirschner, *Reorientation transitions in ultrathin ferromagnetic films by thickness- and temperature-driven anisotropy flows*, Phys. Rev. B **54**, 4137 (1996).
- [29] Y. T. Millev, H. P. Oepen, and J. Kirschner, *Influence of external field on spin reorientation transitions in uniaxial ferromagnets. I. General analysis for bulk and thin-film systems*, Phys. Rev. B **57**, 5837 (1998).
- [30] Y. T. Millev, H. P. Oepen, and J. Kirschner, *Influence of external fields on spin reorientation transitions in uniaxial ferromagnets. II. Ultrathin ferromagnetic films*, Phys. Rev. B **57**, 5848 (1998).
- [31] R. Naik, C. Kota, J. S. Payson, and G. L. Dunifer, *Ferromagnetic-resonance studies of epitaxial Ni, Co, and Fe films grown on Cu(100)/Si(100)*, Phys. Rev. B **48**, 1008 (1993).
- [32] B. Schulz and K. Baberschke, *Crossover from in-plane to perpendicular magnetization in ultrathin Ni/Cu(001) films*, Phys. Rev. B **50**, 13467 (1994).
- [33] A. Abanov, V. Kalatsky, V. L. Pokrovsky, and W. M. Saslow, *Phase diagram of ultrathin ferromagnetic films with perpendicular anisotropy*, Phys. Rev. B **51**, 1023 (1995).
- [34] A. Hubert and R. Schäfer, *Magnetic Domains*, Springer Berlin Heidelberg, 1998.
- [35] J. Kranz and A. Hubert, *Die Möglichkeiten der Kerr-Technik zur Beobachtung magnetischer Bereiche*, Z. angew. Phys **15**, 220 (1963).
- [36] F. Schmidt, W. Rave, and A. Hubert, *Enhancement of magneto-optical domain observation by digital image processing*, Magnetism, IEEE Transactions on **21**, 1596 (1985).

Bibliography

- [37] G. Schütz et al., *Absorption of circularly polarized x rays in iron*, Phys. Rev. Lett. **58**, 737 (1987).
- [38] G. van der Laan et al., *Experimental proof of magnetic x-ray dichroism*, Phys. Rev. B **34**, 6529 (1986).
- [39] J. Stöhr et al., *Element-specific magnetic microscopy with circularly polarized x-rays*, Science **259**, 658 (1993).
- [40] C. M. Schneider, U. Pracht, W. Kuch, A. Chassé, and J. Kirschner, *Magnetic dichroism in photoemission as a spin-resolving probe for electronic correlations*, Phys. Rev. B **54**, R15618 (1996).
- [41] W. Kuch et al., *Element-Selective Magnetic Imaging in Exchange-Coupled Systems by Magnetic Photoemission Microscopy*, Surface Review and Letters **05**, 1241 (1998).
- [42] J. Stöhr et al., *Images of the Antiferromagnetic Structure of a NiO(100) Surface by Means of X-Ray Magnetic Linear Dichroism Spectromicroscopy*, Phys. Rev. Lett. **83**, 1862 (1999).
- [43] F. Nolting et al., *Direct observation of the alignment of ferromagnetic spins by antiferromagnetic spins*, Nature **405**, 767 (2000).
- [44] T. Schmidt et al., *Double aberration correction in a low-energy electron microscope*, Ultramicroscopy **110**, 1358 (2010).
- [45] S. Blundell, *Magnetism in Condensed Matter*, Oxford University Press USA, 2001.
- [46] A. Auerbach, *Interacting electrons and quantum magnetism*, Springer, 1994.
- [47] D. M. Gottlob, Fe/GaAs(001) and MgO/Fe/GaAs(001) epitaxial systems: A spin- and angle-resolved photoemission study, diploma thesis, Technische Universität Dortmund, 2010.
- [48] R. Zeller, *Band Magnetism II*, volume 36 of *Spring School Lecture Notes*, chapter A5, Forschungszentrum Jülich GmbH, 2005.
- [49] P. Mohn, *Magnetism in the solid state: an introduction*, volume 134, Springer Science & Business, 2006.
- [50] O. Gunnarsson, *Band model for magnetism of transition metals in the spin-density-functional formalism*, Journal of Physics F: Metal Physics **6**, 587 (1976).

- [51] C. Schneider and J. Kirschner, Chapter 9 magnetism at surfaces and in ultrathin films, in *Electronic Structure*, edited by K. Horn and M. Scheffler, volume 2 of *Handbook of Surface Science*, pages 511 – 668, North-Holland, 2000.
- [52] S. Blügel, *Spintronics - Magnetism in Reduced Dimensions*, volume 40 of *Spring School Lecture Notes*, chapter A3, Forschungszentrum Jülich GmbH, 2009.
- [53] A. Dekker, *Solid State Physics*, Prentice-Hall Technical books, Macmillan, 1958.
- [54] R. Levy, *Principles of Solid State Physics*, Academic Press, 1968.
- [55] H. Fan, *Elements of solid state physics*, Wiley-Interscience publication, John Wiley & Sons Australia, Limited, 1987.
- [56] M. Tischer et al., *Temperature dependent MCXD measurements of thin Ni films on Cu(100)*, Surface Science **307 - 309, Part B**, 1096 (1994), Proceedings of the European Conference on Surface Science.
- [57] L. Tjeng, Y. Idzerda, P. Rudolf, F. Sette, and C. Chen, *Soft-X-ray magnetic circular dichroism: a new technique for probing magnetic properties of magnetic surfaces and ultrathin films*, Journal of Magnetism and Magnetic Materials **109**, 288 (1992).
- [58] R. Zhang and R. F. Willis, *Thickness-Dependent Curie Temperatures of Ultrathin Magnetic Films: Effect of the Range of Spin-Spin Interactions*, Phys. Rev. Lett. **86**, 2665 (2001).
- [59] I. Turek et al., *First-principles study of the electronic structure and exchange interactions in bcc europium*, Phys. Rev. B **68**, 224431 (2003).
- [60] F. Huang, G. J. Mankey, M. T. Kief, and R. F. Willis, *Finite size scaling behavior of ferromagnetic thin films*, Journal of Applied Physics **73**, 6760 (1993).
- [61] F. Huang, M. T. Kief, G. J. Mankey, and R. F. Willis, *Magnetism in the few-monolayers limit: A surface magneto-optic Kerr-effect study of the magnetic behavior of ultrathin films of Co, Ni, and Co-Ni alloys on Cu(100) and Cu(111)*, Phys. Rev. B **49**, 3962 (1994).
- [62] G. Bochi, C. A. Ballentine, H. E. Inglefield, C. V. Thompson, and R. C. O’Handley, *Perpendicular magnetization and surface magnetoelastic anisotropy in epitaxial Cu/Ni/Cu (001)*, Journal of Applied Physics **79**, 5845 (1996).

Bibliography

- [63] P. Dederichs, R. Zeller, H. Akai, and H. Ebert, *Ab-initio calculations of the electronic structure of impurities and alloys of ferromagnetic transition metals*, Journal of Magnetism and Magnetic Materials **100**, 241 (1991).
- [64] R. Zeller, *Electronic Basis of Magnetism*, volume 40 of *Spring School Lecture Notes*, chapter A2, Forschungszentrum Jülich GmbH, 2009.
- [65] G. Nieuwenhuys, *Magnetic behaviour of cobalt, iron and manganese dissolved in palladium*, Advances in Physics **24**, 515 (1975).
- [66] M. Seider, *Der Einfluß der Gitterverzerrung auf Struktur, Morphologie und Magnetismus ultradünner ferromagnetischer Nickel- und Ni_xPd_{1-x} -Legierungsfilme*, Doktorarbeit, Technische Universität Dresden, 2001.
- [67] H. Wijn, *Magnetic Properties of Metals: D-Elements, Alloys and Compounds*, Data in Science and Technology, Springer Berlin Heidelberg, 1991.
- [68] W. A. Ferrando, R. Segnan, and A. I. Schindler, *Matrix and Impurity-Cluster Polarization in Ni-Pt and Ni-Pd Alloys*, Phys. Rev. B **5**, 4657 (1972).
- [69] N. D. Mermin and H. Wagner, *Absence of Ferromagnetism or Antiferromagnetism in One- or Two-Dimensional Isotropic Heisenberg Models*, Phys. Rev. Lett. **17**, 1133 (1966).
- [70] J. Stöhr and H. Siegmann, *Magnetism: From Fundamentals to Nanoscale Dynamics*, Springer Series in Solid-State Sciences, Springer, 2006.
- [71] J. H. van Vleck, *On the Anisotropy of Cubic Ferromagnetic Crystals*, Phys. Rev. **52**, 1178 (1937).
- [72] P. Bruno, *Physical origins and theoretical models of magnetic anisotropy*, volume 24 of *Spring School Lecture Notes*, chapter 24, Forschungszentrum Jülich GmbH, 1993.
- [73] C. Chappert and P. Bruno, *Magnetic anisotropy in metallic ultrathin films and related experiments on cobalt films (invited)*, Journal of Applied Physics **64**, 5736 (1988).
- [74] Neel, Louis, *L'approche á la saturation de la magnétostriction*, J. Phys. Radium **15**, 376 (1954).

- [75] D. S. Chuang, C. A. Ballentine, and R. C. O'Handley, *Surface and step magnetic anisotropy*, Phys. Rev. B **49**, 15084 (1994).
- [76] K. Ha and R. C. O'Handley, *Magnetization canting in epitaxial Cu/Ni/Cu/Si(001) films*, Journal of Applied Physics **87**, 5944 (2000).
- [77] U. Gradmann, *Struktur und Ferromagnetismus sehr dünner, epitaktischer Ni-Flächenschichten*, Annalen der Physik **472**, 91 (1966).
- [78] U. Gradmann, *Magnetic surface anisotropies*, Journal of Magnetism and Magnetic Materials **54 - 57, Part 2**, 733 (1986).
- [79] J. G. Gay and R. Richter, *Spin Anisotropy of Ferromagnetic Films*, Phys. Rev. Lett. **56**, 2728 (1986).
- [80] A. Freeman and R. quian Wu, *Electronic structure theory of surface, interface and thin-film magnetism*, Journal of Magnetism and Magnetic Materials **100**, 497 (1991).
- [81] H. P. Oepen, Y. T. Millev, and J. Kirschner, *The reorientation transition in Co/Au(111)*, Journal of Applied Physics **81**, 5044 (1997).
- [82] N. C. Koon, B. T. Jonker, F. A. Volkening, J. J. Krebs, and G. A. Prinz, *Direct Evidence for Perpendicular Spin Orientations and Enhanced Hyperfine Fields in Ultrathin Fe(100) Films on Ag(100)*, Phys. Rev. Lett. **59**, 2463 (1987).
- [83] B. Heinrich et al., *Ferromagnetic-resonance study of ultrathin bcc Fe(100) films grown epitaxially on fcc Ag(100) substrates*, Phys. Rev. Lett. **59**, 1756 (1987).
- [84] C. Ballentine, R. Fink, J. Araya-Pochet, and J. Erskine, *Exploring magnetic properties of ultrathin epitaxial magnetic structures using magneto-optical techniques*, Applied Physics A **49**, 459 (1989).
- [85] Z. Q. Qiu, J. Pearson, and S. D. Bader, *Asymmetry of the spin reorientation transition in ultrathin Fe films and wedges grown on Ag(100)*, Phys. Rev. Lett. **70**, 1006 (1993).
- [86] C. Liu, E. R. Moog, and S. D. Bader, *Polar Kerr-Effect Observation of Perpendicular Surface Anisotropy for Ultrathin fcc Fe Grown on Cu(100)*, Phys. Rev. Lett. **60**, 2422 (1988).

Bibliography

- [87] D. P. Pappas, K.-P. Kämper, and H. Hopster, *Reversible transition between perpendicular and in-plane magnetization in ultrathin films*, Phys. Rev. Lett. **64**, 3179 (1990).
- [88] R. Allenspach and A. Bischof, *Magnetization direction switching in Fe/Cu(100) epitaxial films: Temperature and thickness dependence*, Phys. Rev. Lett. **69**, 3385 (1992).
- [89] J. Thomassen, F. May, B. Feldmann, M. Wuttig, and H. Ibach, *Magnetic live surface layers in Fe/Cu(100)*, Phys. Rev. Lett. **69**, 3831 (1992).
- [90] R. Jungblut, M. T. Johnson, J. aan de Stegge, A. Reinders, and F. J. A. den Broeder, *Orientational and structural dependence of magnetic anisotropy of Cu/Ni/Cu sandwiches: Misfit interface anisotropy*, Journal of Applied Physics **75**, 6424 (1994).
- [91] G. Bochi et al., *Perpendicular magnetic anisotropy, domains, and misfit strain in epitaxial Ni/Cu_{1-x}Ni_x/Cu/Si (001) thin films*, Phys. Rev. B **52**, 7311 (1995).
- [92] G. Bochi, C. A. Ballentine, H. E. Inglefield, C. V. Thompson, and R. C. O’Handley, *Evidence for strong surface magnetoelastic anisotropy in epitaxial Cu/Ni/Cu(001) sandwiches*, Phys. Rev. B **53**, R1729 (1996).
- [93] B. N. Engel, C. D. England, R. A. Van Leeuwen, M. H. Wiedmann, and C. M. Falco, *Interface magnetic anisotropy in epitaxial superlattices*, Phys. Rev. Lett. **67**, 1910 (1991).
- [94] F. den Broeder, W. Hoving, and P. Bloemen, *Magnetic anisotropy of multilayers*, Journal of Magnetism and Magnetic Materials **93**, 562 (1991).
- [95] C. H. Lee et al., *Magnetic anisotropy in epitaxial Co superlattices*, Phys. Rev. B **42**, 1066 (1990).
- [96] T. Kingetsu and K. Sakai, *Perpendicular magnetic anisotropy and structures of epitaxial Co/Ag and Co/Au metallic superlattices*, Journal of Applied Physics **73**, 7622 (1993).
- [97] M. Farle, B. Mirwald-Schulz, A. N. Anisimov, W. Platow, and K. Baberschke, *Higher-order magnetic anisotropies and the nature of the spin-reorientation transition in face-centered-tetragonal Ni(001)/Cu(001)*, Phys. Rev. B **55**, 3708 (1997).

- [98] K. Baberschke and M. Farle, *Higher-order contribution and temperature dependence of the magnetic anisotropy in ultrathin films (invited)*, Journal of Applied Physics **81**, 5038 (1997).
- [99] J. Shen, J. Giergiel, and J. Kirschner, *Growth and morphology of Ni/Cu(100) ultrathin films: An in situ study using scanning tunneling microscopy*, Phys. Rev. B **52**, 8454 (1995).
- [100] W. Rave and A. Hubert, *Magnetic ground state of a thin-film element*, Magnetics, IEEE Transactions on **36**, 3886 (2000).
- [101] B. Lilley, *LXXI. Energies and widths of domain boundaries in ferromagnetics*, Philosophical Magazine Series 7 **41**, 792 (1950).
- [102] A. Einstein, *Über einen die Erzeugung und Verwandlung des Lichtes betreffenden heuristischen Gesichtspunkt*, Annalen der Physik **322**, 132 (1905).
- [103] C. Nordling, E. Sokolowski, and K. Siegbahn, *Precision Method for Obtaining Absolute Values of Atomic Binding Energies*, Phys. Rev. **105**, 1676 (1957).
- [104] P. A. M. Dirac, *The quantum theory of dispersion*, Proceedings of the Royal Society of London. Series A **114**, 710 (1927).
- [105] E. Fermi, *Nuclear Physics: A Course Given by Enrico Fermi at the University of Chicago*, Midway Reprints, University of Chicago Press, 1950.
- [106] B. T. Thole, P. Carra, F. Sette, and G. van der Laan, *X-ray circular dichroism as a probe of orbital magnetization*, Phys. Rev. Lett. **68**, 1943 (1992).
- [107] P. Carra, B. T. Thole, M. Altarelli, and X. Wang, *X-ray circular dichroism and local magnetic fields*, Phys. Rev. Lett. **70**, 694 (1993).
- [108] F. Nickel, *Aberrationskorrigierte Photoemissionsmikroskopie an magnetischen Systemen: Von statischer Charakterisierung zu zeitaufgelöster Abbildung*, Doktorarbeit, Universität Duisburg-Essen, Germany, 2013.
- [109] S. Tanuma, C. J. Powell, and D. R. Penn, *Calculations of electron inelastic mean free paths. IX. Data for 41 elemental solids over the 50 eV to 30 keV range*, Surface and Interface Analysis **43**, 689 (2011).
- [110] R. F. Egerton, *Electron energy-loss spectroscopy in the electron microscope*, volume 233, Springer, 1996.

Bibliography

- [111] M. P. Seah and W. A. Dench, *Quantitative electron spectroscopy of surfaces: A standard data base for electron inelastic mean free paths in solids*, Surface and Interface Analysis **1**, 2 (1979).
- [112] S. Tanuma et al., *Experimental determination of electron inelastic mean free paths in 13 elemental solids in the 50 to 5000 eV energy range by elastic-peak electron spectroscopy*, Surface and Interface Analysis **37**, 833 (2005).
- [113] R. Nakajima, J. Stöhr, and Y. U. Idzerda, *Electron-yield saturation effects in L-edge x-ray magnetic circular dichroism spectra of Fe, Co, and Ni*, Phys. Rev. B **59**, 6421 (1999).
- [114] R. M. Tromp, M. Mankos, M. C. Reuter, A. W. Ellis, and M. Copel, *A New Low Energy Electron Microscope*, Surface Review and Letters **05**, 1189 (1998).
- [115] R. Tromp et al., *A simple energy filter for low energy electron microscopy/photoelectron emission microscopy instruments*, Journal of Physics: Condensed Matter **21**, 314007 (2009).
- [116] F. Nickel et al., *Time-resolved magnetic imaging in an aberration-corrected, energy-filtered photoemission electron microscope*, Ultramicroscopy **130**, 54 (2013), Eighth International Workshop on LEEM/PEEM.
- [117] S. Schramm, A. Pang, M. Altman, and R. Tromp, *A Contrast Transfer Function approach for image calculations in standard and aberration-corrected LEEM and PEEM*, Ultramicroscopy **115**, 88 (2012).
- [118] Specs GmbH, <http://www.specs.de/>, 2014.
- [119] R. Tromp et al., *A new aberration-corrected, energy-filtered LEEM/PEEM instrument. I. Principles and design*, Ultramicroscopy **110**, 852 (2010).
- [120] H. Lüth, *Surfaces and Interfaces of Solid Materials*, Springer, Berlin Heidelberg, 1996.
- [121] E. Bauer, *Phänomenologische Theorie der Kristallabscheidung an Oberflächen. I*, Z. Kristallogr. **110**, 372 (1958).
- [122] P. Ruggerone, C. Ratsch, and M. Scheffler, Chapter 13 density-functional theory of epitaxial growth of metals, in *Growth and Properties of Ultrathin Epitaxial Layers*, edited by D. King and D. Woodruff, volume 8 of *The Chemical Physics of Solid Surfaces*, pages 490 – 544, Elsevier, 1997.

- [123] F. C. Frank and J. H. Merwe, *One-dimensional dislocations. II. Misfitting monolayers and oriented overgrowth*, Proc. Roy. Soc.(London) **189**, 216 (1949).
- [124] G. Bochi, O. Song, and R. C. O’Handley, *Surface magnetoelastic coupling coefficients of single-crystal fcc Co thin films*, Phys. Rev. B **50**, 2043 (1994).
- [125] M. A. Herman and H. Sitter, *Fundamentals of the MBE Growth Process*, Springer Berlin Heidelberg, 1989.
- [126] C. Kittel and P. McEuen, *Introduction to Solid State Physics, 7th edition*, volume 8, John Wiley & Sons Inc., 1996.
- [127] J. Y. Tsao, *Materials fundamentals of molecular beam epitaxy*, Academic Press, 1993.
- [128] W. Dekeyser, L. Fiermans, G. Vanderkelen, and J. Vennik, Eds., *Electron Emission Spectroscopy*, D. Reidel Publishing Company, 1973.
- [129] D. Briggs and M. P. Seah, *Practical surface analysis: by auger and X-ray photoelectron spectroscopy*, Wiley New York, 1983.
- [130] L. C. Feldman and J. W. Mayer, *Fundamentals of surface and thin film analysis*, volume 119, North-Holland New York, 1986.
- [131] M. Henzler and W. Göpel, *Oberflächenphysik des Festkörpers*, B.G. Teubner Stuttgart, 1994.
- [132] H. Wedler and K. Heinz, *Information on Surface Structure by Low Energy Electron Diffraction*, Vakuum in Forschung und Praxis **7**, 107 (1995).
- [133] J. Choi, C. B. Eom, G. Rijnders, H. Rogalla, and D. H. A. Blank, *Growth mode transition from layer by layer to step flow during the growth of heteroepitaxial SrRuO₃ on (001) SrTiO₃*, Applied Physics Letters **79**, 1447 (2001).
- [134] E. Brüche, *Elektronenmikroskopische Abbildung mit lichtelektrischen Elektronen*, Zeitschrift für Physik **86**, 448 (1933).
- [135] E. Brüche and W. Knecht, *Bemerkung über die Erreichung hoher Auflösungen mit dem elektronenoptischen Immersionsobjektiv*, Zeitschrift für Physik **92**, 462 (1934).
- [136] W. Teliëps and E. Bauer, *An analytical reflection and emission UHV surface electron microscope*, Ultramicroscopy **17**, 57 (1985).

Bibliography

- [137] W. Grogger et al., *Probing the Nanoworld - Advanced Nanoanalysis in Transmission Electron Microscopy: Overview*, volume 38 of *Spring School Lecture Notes*, chapter B3, Forschungszentrum Jülich GmbH, 2007.
- [138] M. Lentzen, *Probing the Nanoworld - Aberration-Corrected HRTEM*, volume 38 of *Spring School Lecture Notes*, chapter C1, Forschungszentrum Jülich GmbH, 2007.
- [139] P. Ebert, *Probing the Nanoworld - Scanning Probe Microscopy: Overview*, volume 38 of *Spring School Lecture Notes*, chapter B4, Forschungszentrum Jülich GmbH, 2007.
- [140] C. M. Schneider and G. Schönhense, *Investigating surface magnetism by means of photoexcitation electron emission microscopy*, Reports on Progress in Physics **65**, 1785 (2002).
- [141] S. Cherifi, *Probing the Nanoworld - LEEM and Spin Polarized LEEM*, volume 38 of *Spring School Lecture Notes*, chapter C7, Forschungszentrum Jülich GmbH, 2007.
- [142] O. Krivanek, N. Dellby, and M. Murfitt, Aberration correction in electron microscopy, in *Handbook of Charged-Particle Optics, Second Edition*, edited by J. Orloff, chapter 6, pages 601–640, CRC Press, Taylor & Francis Group, LLC, 2009.
- [143] O. Scherzer, *Über einige Fehler von Elektronenlinsen*, Zeitschrift für Physik **101**, 593 (1936).
- [144] O. Scherzer, *Sphärische und chromatische Korrektur von Elektronen-Linsen*, Optik **2**, 114 (1947).
- [145] B. Kabius et al., *First application of Cc-corrected imaging for high-resolution and energy-filtered TEM*, Journal of Electron Microscopy **58**, 147 (2009).
- [146] H. Rose, *Inhomogenous Wien Filter as a Corrector Compensating for the Chromatic and Spherical-Aberration of Low-Voltage Electron Microscopes*, Optik **84**, 91 (1990).
- [147] M. Hibino and S. Maruse, *Correction of the Spherical Aberration of a Magnetic Lens with a Foil Lens*, Journal of Electron Microscopy **25**, 229 (1976).

- [148] T. Koshikawa et al., *A new aberration correction method for photoemission electron microscopy by means of moving focus*, Journal of Physics: Condensed Matter **17**, S1371 (2005).
- [149] L. Oldfield, *Microwave cavities as electron lenses.*, Doktorarbeit, University of Cambridge, 1973.
- [150] G. Schönhense and H. Spiecker, *Correction of chromatic and spherical aberration in electron microscopy utilizing the time structure of pulsed excitation sources*, Journal of Vacuum Science & Technology B **20**, 2526 (2002).
- [151] G. F. Rempfer, D. M. Desloge, W. P. Skoczylas, and O. H. Griffith, *Simultaneous Correction of Spherical and Chromatic Aberrations with an Electron Mirror: An Electron Optical Achromat*, Microscopy and Microanalysis **null**, 14 (1997).
- [152] D. Preikszas and H. Rose, *Correction properties of electron mirrors*, Journal of Electron Microscopy **46**, 1 (1997).
- [153] R. Tromp, J. Hannon, W. Wan, A. Berghaus, and O. Schaff, *A new aberration-corrected, energy-filtered LEEM/PEEM instrument II. Operation and results*, Ultramicroscopy **127**, 25 (2013), Frontiers of Electron Microscopy in Materials Science.
- [154] J. Schaab et al., *Imaging and characterization of conducting ferroelectric domain walls by photoemission electron microscopy*, Applied Physics Letters **104**, (2014).
- [155] D. Meier et al., *Electrostatics at improper ferroelectric domain walls*, unpublished.
- [156] C. M. Schneider, *Probing the Nanoworld - Electron Emission and Photoemission Microscopy*, volume 38 of *Spring School Lecture Notes*, chapter C6, Forschungszentrum Jülich GmbH, 2007.
- [157] Z. Ding, H. Li, R. Shimizu, and K. Gotod, *On the energy distribution of secondary electrons emitted from metals*, Journal of Surface Analysis **15**, 186 (2008).
- [158] L. Landau and E. Lifshitz, *On the theory of the dispersion of magnetic permeability in ferromagnetic bodies*, Phys. Z. Sowjetunion **8**, 101 (1935).
- [159] F. R. Elder, A. M. Gurewitsch, R. V. Langmuir, and H. C. Pollock, *Radiation from Electrons in a Synchrotron*, Phys. Rev. **71**, 829 (1947).
- [160] J. D. Jackson, *Classical Electrodynamics*, Wiley-VCH, third Edition, 1998.

Bibliography

- [161] D. Attwood, *Soft X-Rays and Extreme Ultraviolet Radiation: Principles and Applications*, Cambridge University Press, 2007.
- [162] Halbach, K., *Permanent Magnet Undulators*, J. Phys. Colloques **44**, C1 (1983).
- [163] S. Sasaki et al., *Design of a new type of planar undulator for generating variably polarized radiation*, Nuclear Instruments and Methods in Physics Research Section A: Accelerators, Spectrometers, Detectors and Associated Equipment **331**, 763 (1993).
- [164] J. M. Cowley, *Diffraction physics*, North-Holland Pub. Co. ; American Elsevier Amsterdam : New York, 1975.
- [165] V. Kolarik, M. Mankos, and L. H. Veneklasen, *Close packed prism arrays for electron microscopy*, Optik (Stuttgart) **87**, 1 (1991).
- [166] MaTecK GmbH, <http://www.mateck.de>, 2014.
- [167] A. Schmid and J. Kirschner, *In situ observation of epitaxial growth of Co thin films on Cu(100)*, Ultramicroscopy **42-44**, Part 1, 483 (1992).
- [168] C. Klein, R. Ramchal, A. K. Schmid, and M. Farle, *Controlling the kinetic order of spin-reorientation transitions in Ni/Cu(100) films by tuning the substrate step structure*, Phys. Rev. B **75**, 193405 (2007).
- [169] O. Madelung, U. Rössler, and M. Schulz, Springer materials—the landolt-börnstein database, 2010.
- [170] J. W. Matthews, S. Mader, and T. B. Light, *Accommodation of Misfit Across the Interface Between Crystals of Semiconducting Elements or Compounds*, Journal of Applied Physics **41**, 3800 (1970).
- [171] G. Derry, C. McVey, and P. Rous, *The surface structure and segregation profile of Ni₅₀Pd₅₀(100): a dynamical LEED study*, Surface Science **326**, 59 (1995).
- [172] L. Vegard, *Die Konstitution der Mischkristalle und die Raumfüllung der Atome*, Zeitschrift für Physik **5**, 17 (1921).
- [173] C. M. Schneider et al., *Curie temperature of ultrathin films of fcc-cobalt epitaxially grown on atomically flat Cu(100) surfaces*, Phys. Rev. Lett. **64**, 1059 (1990).

- [174] W. L. O'Brien, T. Droubay, and B. P. Tonner, *Transitions in the direction of magnetism in Ni/Cu(001) ultrathin films and the effects of capping layers*, Phys. Rev. B **54**, 9297 (1996).
- [175] G. Bochi et al., *Magnetic Domain Structure in Ultrathin Films*, Phys. Rev. Lett. **75**, 1839 (1995).
- [176] S. Hameed et al., *Analysis of disordered stripe magnetic domains in strained epitaxial Ni(001) films*, Phys. Rev. B **64**, 184406 (2001).
- [177] H. W. Zhao, Y. Z. Wu, C. Won, F. Toyoma, and Z. Q. Qiu, *Effect of the Cu capping layer on the magnetic anisotropy of Ni/Cu(100)*, Phys. Rev. B **66**, 104402 (2002).
- [178] D. M. Schaller, D. E. Bürgler, C. M. Schmidt, F. Meisinger, and H.-J. Güntherodt, *Spin reorientations induced by morphology changes in Fe/Ag(001)*, Phys. Rev. B **59**, 14516 (1999).
- [179] M. Speckmann, H. P. Oepen, and H. Ibach, *Magnetic Domain Structures in Ultrathin Co/Au(111): On the Influence of Film Morphology*, Phys. Rev. Lett. **75**, 2035 (1995).
- [180] A. Vaterlaus et al., *Two-Step Disordering of Perpendicularly Magnetized Ultrathin Films*, Phys. Rev. Lett. **84**, 2247 (2000).
- [181] J. P. Pierce, M. A. Torija, J. Shen, and E. W. Plummer, *Mapping the magnetic phase diagram of metastable fct Fe/Cu(100) using Co atoms*, Phys. Rev. B **64**, 224409 (2001).
- [182] O. Portmann, A. Vaterlaus, and D. Pescia, *An inverse transition of magnetic domain patterns in ultrathin films*, Nature **422**, 701 (2003).
- [183] B. Kaplan and G. Gehring, *The domain structure in ultrathin magnetic films*, Journal of Magnetism and Magnetic Materials **128**, 111 (1993).
- [184] J. Choi et al., *Magnetic Bubble Domain Phase at the Spin Reorientation Transition of Ultrathin Fe/Ni/Cu(001) Film*, Phys. Rev. Lett. **98**, 207205 (2007).
- [185] C. Won et al., *Magnetic Phase Transition in Co/Cu/Ni/Cu(100) and Co/Fe/Ni/Cu(100)*, Phys. Rev. Lett. **91**, 147202 (2003).

Bibliography

- [186] C. Won et al., *Magnetic stripe melting at the spin reorientation transition in Fe/Ni/Cu(001)*, Phys. Rev. B **71**, 224429 (2005).
- [187] A. Kashuba and V. L. Pokrovsky, *Stripe domain structures in a thin ferromagnetic film*, Phys. Rev. Lett. **70**, 3155 (1993).
- [188] A. B. Kashuba and V. L. Pokrovsky, *Stripe domain structures in a thin ferromagnetic film*, Phys. Rev. B **48**, 10335 (1993).
- [189] I. Booth, A. B. MacIsaac, J. P. Whitehead, and K. De'Bell, *Domain Structures in Ultrathin Magnetic Films*, Phys. Rev. Lett. **75**, 950 (1995).
- [190] M. Carubelli et al., *Spin reorientation transition and phase diagram of ultrathin ferromagnetic films*, Phys. Rev. B **77**, 134417 (2008).
- [191] A. B. MacIsaac, K. De'Bell, and J. P. Whitehead, *Simulation of the Reorientation Transition in Ultrathin Magnetic Films with Striped and Tetragonal Phases*, Phys. Rev. Lett. **80**, 616 (1998).
- [192] M. Sarjala, E. Seppälä, and M. Alava, *Minor magnetization loops in two-dimensional dipolar Ising model*, Physica B: Condensed Matter **406**, 2126 (2011).
- [193] J. S. M. Fonseca, L. G. Rizzi, and N. A. Alves, *Stripe-tetragonal phase transition in the two-dimensional Ising model with dipole interactions: Partition function zeros approach*, Phys. Rev. E **86**, 011103 (2012).
- [194] R. Hoffmann et al., *Perpendicular magnetic domains of a thin Ag/Fe/Ag film observed by magnetic force microscopy at room temperature*, Journal of Magnetism and Magnetic Materials **250**, 32 (2002).
- [195] S. Middelhoek, *Domain Walls in Thin Ni-Fe Films*, Journal of Applied Physics **34**, 1054 (1963).
- [196] T. Trunk, M. Redjda, A. Kákay, M. F. Ruane, and F. B. Humphrey, *Domain wall structure in Permalloy films with decreasing thickness at the Bloch to Néel transition*, Journal of Applied Physics **89**, 7606 (2001).
- [197] Private discussion with A. Kaiser, SPECS GmbH, 2012.
- [198] J. Lee et al., *Evidence for a strain-induced variation of the magnetic moment in epitaxial Cu/Ni/Cu/Si(100) structures*, Phys. Rev. B **55**, 15103 (1997).

- [199] J. Kudrnovský, V. Drchal, and P. Bruno, *Magnetic properties of fcc Ni-based transition metal alloys*, Phys. Rev. B **77**, 224422 (2008).
- [200] M. Seider, R. Kaltofen, U. Muschiol, M.-T. Lin, and C. M. Schneider, *Growth and magnetic properties of thin epitaxial Ni_xPd_{1-x} alloy films on $Cu_3Au(100)$* , Journal of Applied Physics **87**, 5762 (2000).
- [201] F. Matthes, M. Seider, and C. M. Schneider, *Strain-induced magnetic anisotropies in ultrathin epitaxial Ni_xPd_{1-x} alloy films*, Journal of Applied Physics **91**, 8144 (2002).
- [202] A. Braun, B. Feldmann, and M. Wuttig, *Strain-induced perpendicular magnetic anisotropy in ultrathin Ni films on $Cu_3Au(0\ 0\ 1)$* , Journal of Magnetism and Magnetic Materials **171**, 16 (1997).
- [203] D. M. Gottlob, T. Jansen, M. Hoppe, D. E. Bürgler, and C. M. Schneider, *Epitaxial $Cu(001)$ films grown on a $Cr/Ag/Fe/GaAs(001)$ buffer system*, Thin Solid Films **562**, 250 (2014).

Bibliography

Acknowledgements

With the last words written in this thesis I would like to thank all the countless people involved in helping me to get where I am standing now. The PhD time was filled with ups and downs, which I wouldn't want to miss in my life.

First of all, I would like to express my gratitude towards **Prof. Dr. Claus M. Schneider** for making this thesis possible. The opportunity to work in an excellent, international group of scientists and permanently working at a large-scale scientific facility has been exciting and educative. Your knowledgeable and kind appearance will always be an inspiration for me.

I would like to thank **Prof. Dr. Gerd Schönhense** for the disposition to co-referee this thesis.

Dr. Stefan Cramm. Apart from physical discussions, support & guidance for the beamline and help at drafting the thesis, you have become a friend. I enjoy that I can't get away with less than an hour of time whenever we talk, be it in person or over the phone.

A special thanks goes to my fellow PhD students **Hatice Doğanay** and **Dr. Florian Nickel** for countless nightshifts and a comfortable working atmosphere in our group.

I have to thank **Dr. Ingo Krug** for taking me in to the Forschungszentrum Jülich LEEMPEEM team at BESSY II.

I am thankful for the guidance of **Dr. Daniel Bürgler**, who helped a great deal in making the Cu(001) films on buffer systems possible. Discussions, corrections and communication in a most kind way made it a pleasure to work with you.

Thomas Jansen produced the Cu(001) films on the buffer system. Thank you for the invested time and your accurate and detailed work.

The help of **Prof. Dr. Harald Ibach** with LEED pattern analysis in the course of the Cu(001) film system is greatly acknowledged.

I would like to thank **Dr. Slavomír Nemšák** for the nice group atmosphere you created throughout the time we've been working together and all the chit-chats in between.

Dr. Alexander Kaiser was always available if extended help with the LEEM/PEEM

Acknowledgements

was needed. Replacement parts finding their way into my hands during the weekend in a personal meeting at the S-Bahn is just one example that's coming to mind.

I want to thank the **HZB** and **BESSY II staff**, not only for constant work providing my work with synchrotron radiation, electronic-, administrative-, UHV-, and computer support, but also for the nice chats between measurements and office.

The Forschungszentrum Jülich support with computers, by **Jürgen Lauer**, and with electronics, by **Heinz Pfeiffer**, was carried out swiftly and with great precision to my needs. It was always a pleasure stopping by in your office/workshop, or having you here at BESSY II.

The technical support by **Konrad Bickmann** and **Bernd Küpper** for constructional work and help with vacuum parts is greatly acknowledged.

All the fellow **colleagues** and **PhD students at the Peter-Grünberg-Institut 6**, Forschungszentrum Jülich. It was a pleasure working with you, I always enjoyed meeting you.

There are people I met through scientific collaborations and work at BESSY II, some of which have become friends I like to thank for all the good time I've had with them. **Christian Heine**, companion in thesis-writing. We had a lot of stories to share about exhausting and unfortunate times, and I enjoyed that we could always laugh at least about the irony of things. **Jakob Schaab**, measuring with you always was a pleasure, there is still a vast number of triple K's to do. **Dr. Dennis Meier**, I will meet you surfing Santa Cruz sometime in the future. **Gina Peschel**, having lunch or stopping by at your experiment brought a laugh and nice chats into any dull working day. **Francesca Genuzio**, somewhere, there's still a beer or two waiting for us.

Hagen Klemm. Meeting you at work was so fortunate. Thank you for being the guy you are, cheering me up and supporting me when it was needed. I admire your fortitude and positivity.

Lastly I want to thank my family:

My brothers in life, **Alexander Rogosch**, **Andreas Klein**, **Philip Böttger**, **Philipp Uebach**. Meeting you changed my life. I carry you in my heart, through every mile I go.

Rahsan Sarah Schenk. You made me the person I am today. I know I could put my life in your hands without a thought of worry.

Hatice and **Dr. Uwe Schenk**. I learned a lot about life from you, which is incorporated in my everyday relation with people. The unconditional way you treat me is an unbelievable gift to me.

My grandfather **Willhelm Musberg** for being the everyday hero only he could be, my grandmother **Gertrud Musberg** for all these years of love and support, my aunt **Monika Musberg** for a heart of gold, and my uncle **Konstantin Gottlob** for a different, inspiring point of view.

I owe everything to my parents **Ursula Gottlob** and **Christian Gottlob**. Your unconditional love and support made it possible to pursue whatever I wanted in my life. I could not have asked for more.

Acknowledgements

Curriculum Vitae

Personal data

Name: Daniel Marius Gottlob
Date of birth: 17. Mai 1984
Place of birth: Recklinghausen, Germany
Nationality: German
e-mail: daniel.gottlob@uni-dortmund.de

Work experience

Jan. 2011 - ongoing Scientist
Peter-Grünberg-Institut 6, Forschungszentrum Jülich
Nov. 2010 - Dec. 2010 Guest scientist
Institut für Festkörperforschung 9, Forschungszentrum Jülich
Apr. 2007 - Apr. 2009 Undergraduate teaching assistant
Technische Universität Dortmund

Education

Oct. 2014 Submission of Ph.D. Thesis (Dr. rer. nat.)
Title: *Spin-reorientation-transition in epitaxial Ni_xPd_{1-x} films on Cu(001): a microscopic analysis*
Universität Duisburg-Essen
Aug. 2010 Diploma Thesis in Physics
Title: *Fe/GaAs(001) and MgO/Fe/GaAs(001) epitaxial systems: A spin- and angle-resolved photoemission study*
Technische Universität Dortmund
Okt. 2004 - Aug. 2010 Diploma student physics
Technische Universität Dortmund
Sep. 2003 - Jun. 2004 Civilian Service at Seniorenzentrum Grullbad Recklinghausen
1994 - 2003 Abitur (High School degree)
Gymnasium Petrinum, Recklinghausen
1990-1994 Elementary School
Grundschule Hohenzollernstraße, Recklinghausen

Curriculum Vitae

List of own Publications

(in chronological order)

Papers

F. Nickel, **D.M. Gottlob**, I.P. Krug, H. Doganay, S. Cramm, A.M. Kaiser, G. Lin, D. Makarov, O.G. Schmidt, and C.M. Schneider,

Time-resolved magnetic imaging in an aberration corrected, energy-filtered photoemission electron microscope, Ultramicroscopy **130**, 54-62 (2013)

DOI: 10.1016/j.ultramic.2013.03.005

H. J. Elmers, A. Chernenkaya, K. Medjanik, M. Emmel, G. Jakob, G. Schönhense, **D. Gottlob**, I. Krug, F. M. F. de Groot, and A. Gloskovskii,

Exchange coupling in the correlated electronic states of amorphous GdFe films, Physical Review B **88**, 174407 (2013)

DOI: 10.1103/PhysRevB.88.174407

Daniel M. Gottlob, Thomas Jansen, Michael Hoppe, Daniel E. Bürgler, and Claus M. Schneider,

Epitaxial Cu(001) films grown on a Cr/Ag/Fe/GaAs(001) buffer system, Thin Solid Films **562**, 250 - 253 (2014)

DOI: 10.1016/j.tsf.2014.04.078

J. Schaab, I. P. Krug, F. Nickel, **D. M. Gottlob**, H. Doğanay, A. Cano, M. Hentschel, Z. Yan, E. Bourret, C. M. Schneider, R. Ramesh, and D. Meier,

Imaging and characterization of conducting ferroelectric domain walls by photoemission electron microscopy, Applied Physics Letters **104**, 232904 (2014)

DOI: 10.1063/1.4879260

M. Emmel, A. Alfonsov, D. Legut, A. Kehlberger, E. Vilanova, I.P. Krug, **D.M. Got-**

tlob, M. Belesi, B. Büchner, M. Kläui, P.M. Oppeneer, S. Wurmehl, H.J. Elmers, and G. Jakob,

Electronic properties of Co₂FeSi investigated by x-ray magnetic linear dichroism, Journal of Magnetism and Magnetic Materials **368**, 364-373 (2014)

DOI: 10.1016/j.jmmm.2014.06.001

Conference contributions

I.P. Krug, F. Nickel, O. Schaff, A. Berghaus, A.K. Schmid, **D.M. Gottlob**, A. Quesada, S. Cramm, and C.M. Schneider, *A new endstation for time-resolved nanospectroscopy - the aberration-corrected LEEM/PEEM at UE65-1 SGM*, BESSY User Meeting, Berlin, Germany, 9.-10. December 2010

F. Nickel, I.P. Krug, O. Schaff, A.M. Kaiser, **D. Gottlob**, S. Cramm, R.M. Tromp, and C.M. Schneider, *The Jülich TRAX-PEEM @ BESSY II - A state-of-the-art user-facility for time-resolved magnetism research.*, Frühjahrstagung der DPG, Dresden, Germany, 13.-18. March 2011

D.M. Gottlob, L. Plucinski, C. Westphal, C.M. Schneider, *Fe/GaAs(001) and MgO/Fe/GaAs(001) epitaxial systems: A spin- and angle-resolved photoemission study*, Frühjahrstagung der DPG, Dresden, Germany, 13.-18. March 2011

C.M. Schneider, M. Patt, V. Feyer, C. Wiemann, I.P. Krug, F. Nickel, **D. Gottlob**, and S. Cramm, *Photoelectron Spectroscopy - Opportunities and Challenges*, Internat. Symposium of Synchrotron Radiation in Natural Science, Krakau, Polen, 20.-25. May 2012

I.P. Krug, I. Vrejoiu, A. Morelli, F. Nickel, **D. Gottlob**, H. Doganay, N. Barrett, J. Wang, and C.M. Schneider, *Ferroelectrically induced valency change in multiferroic PbTiO₃/La_{0.7}Sr_{0.3}MnO₃/BaTiO₃ nanostructure arrays*, LEEM-PEEM 8, Hong-Kong, 11.-15. November 2012

F. Nickel, I.P. Krug, **D.M. Gottlob**, A.M. Kaiser, D. Makarov, G. Lin, S. Cramm, H. Doganay, O.G. Schmidt, and C.M. Schneider, *Time-resolved Magnetic Imaging in an Energy-Filtered, Aberration-corrected Photoemission Electron Microscope*, BESSY User

Meeting, Berlin, Germany, 12.-14. December 2012

D.M. Gottlob, I.P. Krug, F. Nickel, H. Doganay, S. Cramm, and C.M. Schneider, *On the micromagnetic origin of the spin-reorientation transition in Ni_xPd_{1-x} alloys*, BESSY User Meeting, Berlin, Germany, 12.-14. December 2012

H. Doğanay, I.P. Krug, J. Schubert, **D.M. Gottlob**, F. Nickel S. Cramm, and C.M. Schneider *XAS Studies on All-Oxide Ferromagnetic/Ferroelectric Heterosystems: $SrTiO_3/La_{0.7}Sr_{0.3}MnO_3/BaTiO_3$* , BESSY User Meeting, Berlin, Germany, 12.-14. December 2012

F. Nickel, I.P. Krug, **D.M. Gottlob**, A.M. Kaiser, D. Makarov, G. Lin, S. Cramm, H. Doganay, O.G. Schmidt, and C.M. Schneider, *Time-resolved Magnetic Imaging in an Energy-Filtered, Aberration-corrected Photoemission Electron Microscope*, Frühjahrstagung der DPG, Regensburg, Germany, 10.-15. March 2013

H. Doganay, I.P. Krug, J. Schubert, **D.M. Gottlob**, F. Nickel, S. Cramm, and C.M. Schneider, *XAS Studies on All-Oxide Ferromagnetic/Ferroelectric Heterosystems: $SrTiO_3(001)/La_{0.7}Sr_{0.3}MnO_3/BaTiO_3$* , Frühjahrstagung der DPG, Regensburg, Germany, 10.-15. March 2013

I.P. Krug, I. Vrejoiu, A. Morelli, F. Nickel, **D.M. Gottlob**, H. Doganay, R. Laskowski, N. Barrett, J. Wang, and C.M. Schneider, *Tunable ferroelectric imprint and Mn valency in $PbTiO_3/La_{0.7}Sr_{0.3}MnO_3$ nanostructures*, Frühjahrstagung der DPG, Regensburg, Germany, 10.-15. March 2013

D.M. Gottlob, I.P. Krug, F. Nickel, H. Doganay, S. Cramm, and C.M. Schneider, *On the micromagnetic origin of the spin-reorientation transition in Ni_xPd_{1-x} alloys*, Frühjahrstagung der DPG, Regensburg, Germany, 10.-15. March 2013

M. Emmel, I. Krug, **D.M. Gottlob**, A. Alfonsov, S. Wurmehl, H.J. Elmers, and G. Jakob, *Electronic properties of Heusler alloys investigated by X-ray magnetic linear dichroism*, Frühjahrstagung der DPG, Regensburg, Germany, 10.-15. March 2013

D.M. Gottlob, I.P. Krug, H. Doğanay, F. Nickel, S. Cramm, and C.M. Schneider, *Spin-reorientation transition and domain structure in Ni_xPd_{1-x} alloys*, Frühjahrstagung der

List of own Publications

DPG, Dresden, Germany, 30. March - 04. April 2014

H. Doğanay, I.P. Krug, **D.M. Gottlob**, S. Cramm, and C.M. Schneider, *A combined LEEM/PEEM study on ferroelectric domains in perovskite crystals*, Frühjahrstagung der DPG, Dresden, Germany, 10.-15. March 2014

D.M. Gottlob, H. Doğanay, F. Nickel, S. Cramm, I.P. Krug and C.M. Schneider, *Domain orientation in the vicinity of the spin-reorientation transition in $Ni_xPd_{1-x}/Cu(001)$* , LEEMPEEM 9, Berlin, Germany, 14. September - 18. September 2014

I.P. Krug, J. Schaab, F. Nickel, **D.M. Gottlob**, H. Doğanay, A. Cano, M. Hentschel, Z. Yan, E. Bourret, C.M. Schneider, R. Ramesh, D. Meier, *Imaging and characterization of conducting ferroelectric domain walls by photoemission microscopy*, LEEMPEEM 9, Berlin, Germany, 14. September - 18. September 2014

A. Quesada, M. Monti, I.P. Krug, N. Rougemaille, F. Nickel, **D.M. Gottlob**, H. Doğanay, A.T. N'Diaye, G. Chen, A. Serrano, K.F. McCarty, J.F. Fernández, C.M. Schneider, A.K. Schmid, and J. de la Figuera, *Temperature dependence of the single-domain threshold in Fe nanostrips: a reversible magnetic transition*, LEEMPEEM 9, Berlin, Germany, 14. September - 18. September 2014

H. Doğanay, I.P. Krug, **D.M. Gottlob**, S. Cramm, and C.M. Schneider, *Interplay between ferroelectricity and magnetosstrictive behavior in artificial $BaTiO_3(001)/Fe$ multiferroics*, LEEMPEEM 9, Berlin, Germany, 14. September - 18. September 2014

D.M. Gottlob, H. Doğanay, F. Nickel, I.P. Krug, S. Cramm, and C.M. Schneider, *Microscopy studies on magnetization (dynamics) and ferroelectricity at the FZ Jülich LEEM/PEEM endstation at BESSY-II*, Deutsche Tagung für Forschung mit Synchrotronstrahlung, Neutronen und Ionenstrahlen an Großgeräten 2014, Bonn, Germany, 21. September - 23. September 2014

Band / Volume 91

6th Georgian-German School and Workshop in Basic Science

A. Kacharava (Ed.) (2014), CD

ISBN: 978-3-89336-991-1

Band / Volume 92

**Ab initio investigations of π -conjugated-molecule-metal interfaces
for molecular electronics and spintronics**

M. Callsen (2014), viii, 155 pp

ISBN: 978-3-89336-992-8

Band / Volume 93

**Ladungstransportmessungen an Si(111) Oberflächen
mit einem Multispitzen-Rastertunnelmikroskop**

M. Blab (2014), iv, 132, X pp

ISBN: 978-3-89336-997-3

Band / Volume 94

Functional Soft Matter

Lecture Notes of the 46th IFF Spring School 2015

23 February – 06 March, 2015 Jülich, Germany

ed. by J. Dhont, G. Gompper, G. Meier, D. Richter, G. Vliegenthart, R. Zorn

(2015), ca. 600 pp

ISBN: 978-3-89336-999-7

Band / Volume 95

**2-Steps in 1-pot: enzyme cascades for the synthesis
of chiral vicinal amino alcohols**

T. Sehl (2014), XIV, 167 pp

ISBN: 978-3-95806-001-2

Band / Volume 96

**Immunohistochemical and electrophysiological characterization of the
mouse model for Retinitis Pigmentosa, *rd10***

S. Biswas (2014), XII, 119 pp

ISBN: 978-3-95806-011-1

Band / Volume 97

**Single molecule localization microscopy: Imaging of cellular structures
and a new three-dimensional localization technique**

X. Fan (2014), XII, 92 pp

ISBN: 978-3-95806-014-2

Band / Volume 98

Cryogenic Break-Junction Characterization of Single Organic Molecules

T. Grellmann (2014), VI, 86 pp

ISBN: 978-3-95806-015-9

Band / Volume 99

Interacting Interactions: A Study on the Interplay of Molecule-Molecule and Molecule-Substrate Interactions at Metal-Organic Interfaces

M. Willenbockel (2014), IX, 245 pp

ISBN: 978-3-95806-018-0

Band / Volume 100

Microwire crossbar arrays for chemical, mechanical, and thermal stimulation of cells

P. Rinklin (2015), xii, 184 pp

ISBN: 978-3-95806-022-7

Band / Volume 101

Modification and characterization of potential bioelectronic interfaces

K. Greben (2015), 76 pp

ISBN: 978-3-95806-028-9

Band / Volume 102

Extending the precision and efficiency of the all-electron full-potential linearized augmented plane-wave density-functional theory method

G. Michalíček (2015), 195 pp

ISBN: 978-3-95806-031-9

Band / Volume 103

Metabolic engineering of *Escherichia coli* for the production of plant phenylpropanoid derived compounds

P. V. van Summeren-Wesenhagen (2015), V, 92 pp

ISBN: 978-3-95806-039-5

Band / Volume 104

Spin-reorientation transition in epitaxial $\text{Ni}_x\text{Pd}_{1-x}$ films on Cu(001): a microscopic analysis

D. Gottlob (2015), x, 134 pp

ISBN: 978-3-95806-049-4

Weitere **Schriften des Verlags im Forschungszentrum Jülich** unter
<http://www.wzb1.fz-juelich.de/verlagextern1/index.asp>

Schlüsseltechnologien /
Key Technologies
Band / Volume 104
ISBN 978-3-95806-049-4

